LBNL-44440

ERNEST ORLANDO LAWRENCE
BERKELEY NATIONAL LABORATORY

Flow Dynamics and Solute Transport in Unsaturated Rock Fractures

Grace W. Su

Earth Sciences Division

October 1999

Ph.D. Thesis

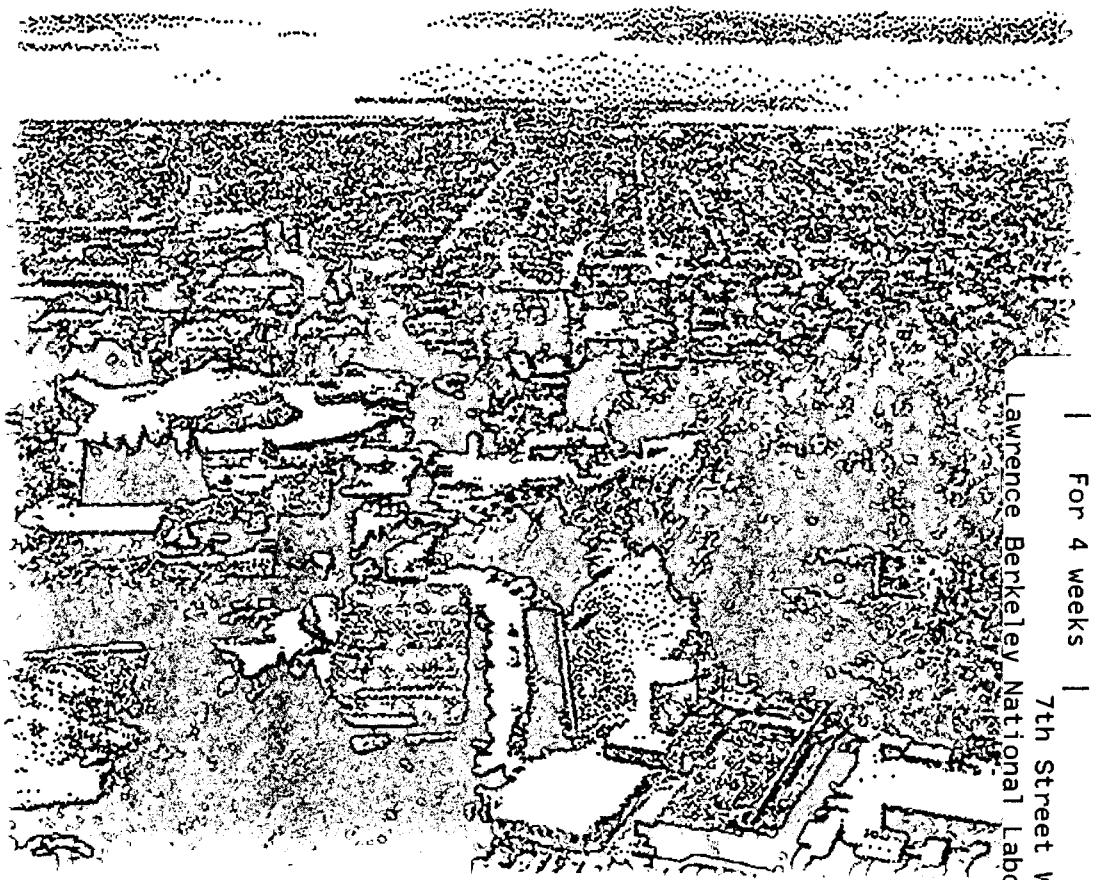

DISCLAIMER

LBNL-44440

Flow Dynamics and Solute Transport in Unsaturated Rock Fractures

by

Grace Woan-chee Su

Ph.D. Thesis

Department of Civil and Environmental Engineering
University of California, Berkeley

and

Earth Sciences Division
Lawrence Berkeley National Laboratory
University of California
Berkeley, CA 94720

October 1999

This work was supported by the Director, Office of Science, Office of Biological and Environmental Research under the U.S. Department of Energy under Contract No. DE-AC03-76SF00098.

Flow Dynamics and Solute Transport in Unsaturated Rock Fractures

by

Grace Woan-chee Su

Abstract

Flow Dynamics and Solute Transport in Unsaturated Rock Fractures

by

Grace Woan-chee Su

Doctor of Philosophy
in
Engineering-Civil and Environmental Engineering

University of California, Berkeley

Professor James R. Hunt, Chair

Rock fractures play an important role in flow and contaminant transport in fractured aquifers, production of oil from petroleum reservoirs, and steam generation from geothermal reservoirs. In this dissertation, phenomenological aspects of flow in unsaturated fractures were studied in visualization experiments conducted on a transparent replica of a natural, rough-walled rock fracture for inlet conditions of constant pressure and flow rate over a range of angles of inclination. The experiments demonstrated that infiltrating liquid proceeds through unsaturated rock fractures along non-uniform, localized preferential flow paths. Even in the presence of constant boundary conditions, intermittent flow was a persistent flow feature observed, where portions of the flow channel underwent cycles of snapping and reforming. Two modes of intermittent flow were observed, the pulsating blob mode and the rivulet snapping mode. A conceptual model for the rivulet snapping mode was proposed and examined using idealized, variable-aperture fractures. The frequency of intermittent flow events was measured in several experiments and related to the capillary and Bond numbers to characterize this flow behavior.

Finger drainage, the dynamics of blob migration, and rivulet flow were additional flow features examined theoretically and experimentally. Finger drainage, or the formation a rivulet connected to an advancing blob, occurred over a range of wettabilities and certain scales of surface roughnesses. During blob migration, contact angle hysteresis was an important factor controlling the rate at which the blobs move through the fracture. During rivulet flow, the rivulet width was affected by the wettability of the surface. In sufficiently large apertures, the liquid in the rivulet did not completely span the aperture and was unstable in that region.

Breakthrough curves of a conservative chloride tracer were obtained in laboratory experiments to study solute transport along preferential flow channels in unsaturated fractures. Longer travel times were measured when flow was intermittent compared to flow that was steady. Most of the breakthrough curves were analyzed with three transfer function models and the lognormal transfer function fit the measured data the best, indicating that it may be applicable for modeling solute transport in unsaturated, heterogeneous fractures. A model was also formulated to describe transport when the pulsating blob mode of intermittent flow occurred and was successfully fit to the measured data.

Dedication

To my parents,

Yu Ming and Chu Eng Su

Table of Contents

List of Figures

List of Tables

Acknowledgements

I would like to express my sincere appreciation to my adviser, Professor Jim Hunt, for providing guidance and direction on my research. His careful comments and suggestions on my dissertation have been invaluable and I am fortunate to have been one of his students. Dr. Feng Wen also served as my adviser during a portion of my studies and I am thankful for her support and suggestions on my research and dissertation. I would also like to gratefully acknowledge Professor Tad Patzek for giving his insight and comments in preparing this dissertation.

I am extremely thankful to Dr. Karsten Pruess for his continuous support and technical guidance on my research. His enthusiasm for research has given me inspiration many times throughout my years at U.C. Berkeley. My deepest gratitude to Dr. Jil Geller for getting me started in the laboratory and for always being available to give her input and advice. It has been a great pleasure working with these two researchers. Dr. Chin-Fu Tsang should be acknowledged for initiating the collaboration between LBL and the CEE department at U.C. Berkeley, which strongly influenced my decision to come to Berkeley. I would also like to thank Maria Dragila, Peter Persoff, and Tim Kneafsey for being very generous with their time in discussing my research work.

Many thanks to the people in my lab at LBL for the interesting conversations, the wonderful birthday celebrations, and lunch outings: Patty Seifert, Kurt Nehei, Michael Kowalsky, Sharon Borglin, Roberto Suárez-Rivera, Brad Bessinger, Jianli Fan, Pingan Huang, and Galen Hesler. A special thank you to my officemates, Pascual Benito and Seiji Nakagawa, for making our office a pleasant and fun place to work in. Thanks also to my other friends and colleagues from LBL: Julie Najita, Henk Keers, Rohit Salve, David Mays, Michael Steiger, Paul Cook, Deb Hopkins, Jerry Fairley, Stefan Finsterle, Jiamin Wan, Tetsu Tokunaga, Yvonne Tsang, Tai-Sheng Liou, Kaushik Das, Andrew Cohen, Amitabh Garg, Max Hu, Maria Fink, Glenn Morrison, Wesley Steele, and Melissa Grush.

My Berkeley friends outside of LBL have also made my years here very special and enjoyable. I have many fond memories of the friendships with Emily Zedler, Nina Wu, Hermann Kim, Pierre Korzilius, Frederike Schilter, Katti Millock, Sandy Hoffmann, Connie Anderson,

Jeannie Chiu, Sonia Nosratinia, Romy Choi, Lih-wei Lin, Augie Kuo, Chaincy Kuo, Dahlia Horowitz, Emily Hsu, Amy Wilson, and Debbie Bennett. The support from friends away from Berkeley is also very much appreciated: Laura Paquette, Paul Lindenfeld, Nathan Lim, Jeany Cheng, Denise Edwell, Heidi Emery, and Corrie Bair.

My studies at Berkeley could not have been completed without the encouragement and love from my parents, Yu Ming and Chu Eng, my brother, Stephen, and my sister, Jeanne.

I would also like to extend my gratitude to my relatives in the Bay area for their support: Peggy Huang, Terry Huang, Dick Chang, and Huibi Chang. A special thank you to Sara Kashima and Amy Takaki for being like my extended family throughout my years at Berkeley.

This work was supported by the Director, Office of Energy Research, Office of Health and Environmental Sciences, Biological and Environmental Research Program, of the U.S. Department of Energy under Contract No. DE-AC03-76SF00098.

1. Introduction

1.1. Overview

Fractures in the unsaturated zone play an important role in water infiltration and contaminant transport. The transport of dissolved radionuclides through fractures in the unsaturated zone and into the groundwater is a concern at Yucca Mountain, Nevada, which is a site currently being evaluated as a potential nuclear waste repository. Non-aqueous phase liquids (NAPLs) have frequently been released into the unsaturated zone by leaking underground storage tanks and spills at industrial sites. Rock fractures may provide fast pathways for the migration of NAPLs through the unsaturated zone and to the groundwater table.

The conventional approach to describing seepage of liquids through unsaturated fractures involves using macroscale continuum concepts and volume averaging over a large scale (*Peters and Klavetter*, 1988). The fracture is modeled as parallel plates and the aperture between the plates represents the average aperture of a natural rock fracture with variable apertures. This approach predicts that the liquid will proceed as a spatially uniform infiltration front, subject to strong capillary imbibition effects from the rock matrix that draws the flowing liquid from the fracture (*Nitao and Busheck*, 1991; *Wang and Narasimhan*, 1993).

Field studies have provided strong evidence that water proceeds non-uniformly along fast flow paths through the unsaturated zone. At Rainier Mesa, Nevada, only portions of the fractures carried water, and the chemical composition of the water from the fractures indicated that it was of recent origin and was substantially different from the nearby rock matrix water (*Wang et al.*, 1993). Tracers injected into a thick unsaturated zone of fractured chalk in the Negev Desert in Israel were observed to rapidly migrate across this zone (*Nativ et al.,* 1995). These observations were explained by water migrating rapidly along localized preferential flow paths through rock fractures. The contact area of flowing water on the rock is greatly reduced by preferential flow paths compared to sheet flow, resulting in a decrease in the liquid residence time in the fracture and a reduction of imbibition of the flowing liquid into the rock matrix.

Preferential flow paths can accelerate contaminant transport compared with the conventional models which predict spatially uniform infiltration. The effect of preferential flow during solute transport in saturated fractures has been studied extensively for the past two decades (e.g. *Neretnieks et al.*, 1982; *Abelin et al.*, 1987; *Moreno et al., 1997*). Features of laboratory breakthrough curves (BTC's) attributed to preferential flow are a steep rise at the early times and multiple peaks in the breakthrough curves (*Neretnieks et al.*, 1982; 1985). The channel model proposed by *Tsang and Tsang* (1987) was developed to account for the occurrence of preferential flow in saturated fractures, which successfully reproduced the features in the laboratory BTC's measured by *Neretnieks et al.* (1982). The effect of preferential flow on solute transport under unsaturated conditions has been primarily limited to studies in soils. The breakthrough curves measured in soils with macropores (*Wildenschild et al.*, 1994) and in heterogeneous sands (*Wildenschild and Jensen*, 1999) had a steep rise at early times and multiple peaks, which are the same features observed in the BTC's measured in saturated fractures. *Birkholzer and Tsang* (1997) performed numerical simulations of flow and transport in unsaturated, heterogeneous porous media and obtained tracer breakthrough curves that also exhibited these features.

1.2. Mechanisms for Preferential Flow

Preferential flow is the focusing of flow into narrow channels or fingers. During two-phase flow, preferential flow or fingering can arise due to fluid instabilities created by density or viscosity differences between two immiscible fluids or because of heterogeneities in the geologic media (*Kueper and Frind*, 1988). Unstable preferential flow has been studied extensively over a number of decades. During liquid invasion of dry homogeneous porous media or fractures, microscopic perturbations can form on the macroscopically planar front separating two immiscible fluid phases and develop into fingers when conditions for hydrodynamic instability are present. Viscous and gravitational forces can act as stabilizing or destabilizing forces for fingering. Viscous instability occurs when less viscous fluid displaces a more viscous fluid. Gravitational instability occurs when a denser fluid displaces a lighter one from above. Viscous

instability has been studied primarily in the petroleum industry because of its importance for oil extraction, while gravitational instability has been examined extensively by soil scientists and hydrologists because of its significance in groundwater recharge and contamination.

A first order linear stability analysis was performed by *Chuoke et al.* (1959) to determine the necessary and sufficient conditions for the onset of instability in homogeneous media. The fingering criterion is a function of the surface tension, interfacial velocity in the direction of flow, and the density and viscosity differences between the two fluids. The theoretical formulation agreed well with the experiments *Chuoke et al.* (1959) performed in parallel plates (Hele-Shaw cells) and two-dimensional cells filled with porous material. Linear stability analysis is still currently used to analyze results from laboratory fingering experiments. *Wang et al.* (1998a,b) generalized the analysis performed by *Chuoke et al.* (1959) to include the effects of wettability and successfully predicted the finger size and velocity for a range of conditions that gave rise to gravity fingering, including air entrapment, soil layering, water repellency, and surface desaturation. In nature, application of linear stability theory to predict the onset of fingering and the subsequent finger widths is difficult since the conditions for this theory rarely, if ever, hold (*Glass and Nicholl*, 1996). Even in nominally homogeneous media, fingers can meander and merge due to small-scale heterogeneity, and this is not described by linear stability theory (*Glass et al.*, 1989a,b; 1991).

In heterogeneous soils and fractures, fingering occurs because of the distribution of the heterogeneities rather than an unstable interface between the two fluids. When water moves through soils with discrete lenses of coarse and fine material, the lenses can act as barriers to flow and cause flow focusing (*Kung*, 1990a,b). Flow can bypass the soil matrix and preferentially enter macropores, which are defined as large soil pores that have diameters ranging from 0.075 to 1.0 mm or more (*Luxmoore et al.*, 1990). A similar phenomenon occurs in unsaturated fractured rocks, where the rock matrix is bypassed and flow preferentially occurs through the fractures. In macropores, water fills the entire cross-section of the pore or flows as a film along the pore surface (*McCoy et al*, 1994). In unsaturated fractures, flow is more likely to proceed as localized fingers due to gravitational instabilities or variability in aperture sizes, rather than as a smooth sheet which fills the entire plane of the fracture. Film flow may also occur along the fracture

surface driven by favorable wetting conditions and small-scale surface roughness (*Tokunaga and Wan*, 1997).

Flow of water through fractures while the rock matrix remains unsaturated is contrary to expectations from capillary theory. As water enters an air-filled porous medium, capillary theory predicts that all pores smaller than a critical size will contain water, while larger pores remain air-filled. According to this theory, the rock matrix should fill with water before the fracture does since the matrix pores are small relative to the size of the fracture opening. Earlier conceptual models of flow in unsaturated, fractured rock assumed that most of the infiltrating water flowed through the rock matrix since the matrix has high suction pressures (*Wang and Narasimhan*, 1985; *Peters and Klavetter*, 1988). Such models predict very low seepage rates through unsaturated fractured rock that are inconsistent with the large seepage velocities measured in the field. Preferential flow through the rock fractures was therefore hypothesized to be responsible for the large seepage velocities. Flow through the fractures in the presence of an unsaturated matrix can occur when the water flux becomes larger than the hydraulic conductivity of the matrix, resulting in ponded infiltration, or where local heterogeneity diverts water into the fracture (*Glass and Nicholl*, 1996). The water that flows through the fracture also gets imbibed into the dry or partially saturated matrix, but the rate of imbibition may be relatively low, particularly in hard rocks of low permeability, and when there are coatings on the fracture surface. Matrix imbibition is also reduced when the water flows as localized fingers rather than as a spatially uniform sheet down the fracture plane since the surface area contacted by the water is much smaller (*Pruess*, 1999).

1.3. Approaches for Describing Unsaturated Flow in Porous and Fractured Media

Petroleum engineers, soil scientists, and hydrologists have traditionally used a macroscopic continuum approach to describe multiphase flow in porous media, involving scales much larger than the pore scale. Darcy's Law, which has been applied to single phase flow in porous media, can be generalized for multiphase flow of immiscible phases and is written for phase l as (*Scheidegger*, 1974):

$$u_l = -\frac{kk_{r,l}}{\mu_l}(\nabla P_l - \rho_l g) \tag{1.1}$$

where u_l is the Darcy velocity, k is the inherent permeability of the porous medium, $k_{r,l}$ is the relative permeability of the liquid, μ_l is the viscosity, ρ_l is the density, P_l is the liquid phase pressure, and g is the gravitational acceleration. Relative permeability quantifies the interference of one phase with the other and varies between 0 and 1.

The mass balance equation for phase l is:

$$\frac{\partial(\phi S_l)}{\partial t} = -\nabla \cdot u_l \tag{1.2}$$

where ϕ is the porosity, or volume of voids per volume of porous medium, and S_l is the saturation of phase l, or fraction of void space occupied by phase l.

The migration of liquids through the unsaturated zone proceeds under the combined action of gravity, capillary and pressure forces and is commonly described using Richards' equation. This equation assumes that the effect of displaced air during liquid infiltration can be neglected, flow is laminar, air pressure and temperature are constant, and liquid density and viscosity are also constant. Combining Equations 1.1 and 1.2 to eliminate u_l results in the multiphase extension of Richards' equation, which is expressed as:

$$\frac{\partial(\phi S_l)}{\partial t} = \nabla \cdot \left[\frac{kk_{r,l}}{\mu_l}(\nabla P_l - \rho_l g)\right] \tag{1.3}$$

The pressure in the liquid phase is equal to the (constant) pressure in the air, P_{air}, minus the capillary pressure, P_c:

$$P_l = P_{air} - P_c \tag{1.5}$$

At equilibrium, the capillary pressure derived from the Young-Laplace equation for an interface spanning an opening between parallel plates of width b is given by:

$$P_c = \frac{2\sigma \cos\gamma}{b} \tag{1.6}$$

where σ is the interfacial tension between the fluids and γ is the contact angle measured between the wetting phase and the solid phase.

Richards' equation has been applied to variable aperture fractures, based upon the conceptual model that views a fracture as a two-dimensional heterogeneous porous medium. The heterogeneities are represented by variable apertures in the fracture plane (*Pruess and Tsang*, 1990; *Pruess*, 1998). Local permeability is directly proportional to the square of the aperture width, b, or:

$$k = \frac{b^2}{12} \tag{1.4}$$

derived for laminar flow between parallel plates (*deMarsily*, 1986). *Pruess* (1998) numerically simulated water seepage in heterogeneous, unsaturated fractures using Richards' equation. The variability in aperture sizes and asperity contacts resulted in flow focusing, liquid ponding, and bypassing.

When Richards' equation is used to describe flow in fractures, the capillary pressure is related to the fluid saturation and relative permeability using constitutive relationships originally used for porous media, such as the curves derived by *Corey* (1954), *Brooks and Corey* (1964), and *van Genuchten* (1980). *Reitsma and Kueper* (1994) measured capillary pressure-saturation curves in horizontal rough-walled fractures and found that the measured curves were well represented by the Brooks and Corey curve. Relative permeability curves measured by *Fourar et al.* (1993) and *Persoff and Pruess* (1995) during two-phase flow in fractures were qualitatively

similar to curves obtained in porous media. *Fourar et al.* (1993) obtained a family of relative permeability curves that depended on the liquid velocity rather than the single curve obtained in porous media. *Persoff and Pruess* (1995) measured relative permeabilities in fractures that were generally lower than predicted by the *Corey* (1954) relationships calculated using common values of residual saturations measured in porous media. Such discrepancy indicates that the constitutive relationships derived for porous media are not entirely applicable for fractures. In addition, gravity was not included in these measurements. The constitutive relationships will be a function of the relative strength of gravity since more wetting phase will be trapped at lower angles of inclination compared to higher angles of inclination for a given capillary pressure.

Invasion percolation theory is also frequently used to describe preferential flow and has been successful in reproducing qualitative features of fingering observed in laboratory scale experiments conducted in porous media and fractures (*Lenormand and Zarcone*, 1983; *Nicholl et al.*, 1994). In percolation theory, a lattice is constructed which is made up of sites connected by bonds. The sites are given a probability of filling from a uniform probability distribution. All sites connected to a wetted site are available for filling and the one with the highest assigned probability of filling is found and filled (*Glass*, 1993). Simulations performed using invasion percolation are faster than those using continuum, marcoscale approaches (*Ewing and Berkowitz*, 1998), but it is not clear whether and how invasion percolation can be applied for flow and transport predictions in the field (*Pruess et al.*, 1999).

1.4. Experimental Observations of Preferential Flow Features

Preferential flow in unsaturated fractures has been examined in a number of laboratory studies. *Schwille* (1984) conducted a series of flow visualization experiments in unsaturated and saturated porous media and fractures. In the unsaturated fracture flow experiments, the fractures consisted of two flat glass plates, separated by a uniform aperture (Hele-Shaw cell) and were inclined vertically. Both smooth and rough (sand-blasted) glass plates were used. For the smooth plates, 0.1 mm and 0.2 mm apertures were used, and an aperture of 0.2 mm was used in the rough plates. Kerosene or TCE was introduced as a point source into the initially dry plates at a

constant flow rate. Both liquids formed one thin narrow liquid channel or rivulet in the 0.2 mm smooth plates. The distribution of the two liquids was different in the 0.1 mm smooth plates than in the 0.2 mm plates due to the increase in the capillary force. Instead of forming one thread immediately below the inlet, the liquid spread laterally, forming a diffuse front near the top of the fracture. Below this diffuse front, multiple rivulets formed, where the liquid front became gravitationally unstable. The liquid distribution was even more complex in the rough plates, where a network of fingers formed beneath the source. These fingers split and merged into each other and were much more tortuous than the rivulets which formed in the smooth plates.

Nicholl et al. (1994) used a less idealized fracture than *Schwille* (1984) in their studies of gravitational instability in inclined fractures. Their analog fracture consisted of two obscure glass plates, which had a statistically homogeneous aperture distribution. *Nicholl et al.* (1994) observed several different boundary conditions which produced gravitationally unstable fingers. Fingers immediately formed when a constant flux below the gravitationally driven saturated flux of the plates was applied to the inlet. Fingering also occurred when the plates were inverted so that the denser fluid rested on top of the lighter one. When a finite volume of water was injected uniformly over the width of the fracture, fingers formed after the water was allowed to redistribute. *Nicholl et al.* (1994) conducted a series of experiments where finger widths were measured after injecting a finite volume of water and compared with predictions using linear stability theory. A range of angles of inclination and volumes of injected water were used. They found that linear stability analysis may provide a lower bound on their measured finger widths. The method of liquid application in their experiments caused finite perturbations along the air-water interface, however, and this may have controlled the width of the fingers that subsequently formed. Linear stability theory is based on the assumption that an infinitesimal number of microscopic perturbations are present at the interface; therefore, this theory may not be applicable for *Nicholl et al.'s* conditions since a finite number of perturbations formed in their experiments. These results again illustrate the difficulty of maintaining conditions where linear stability theory is applicable even when the system is nominally homogeneous. *Nicholl et al.* (1993) also examined the influence of initial moisture content on fingering instability in obscure

glass plates and found that the fingers traveled faster and were narrower and longer compared to the initially dry case.

Non-isothermal conditions can also significantly affect flow behavior in unsaturated fractures. *Kneafsey and Pruess* (1998) conducted a series of flow visualization experiments on natural and analog fractures to examine thermally driven liquid flow behavior. Preferential flow paths created by vapor condensation were prevalent in these experiments. They exhibited a number of flow regimes including continuous rivulet flow, intermittent rivulet flow, and drop flow.

Film flow along the fracture surface may also be an important factor contributing to fast flow in fractures, where a film is defined as having one contact and one free surface. *Tokunaga and Wan* (1997) proposed and demonstrated that film flow could provide a mechanism for flow observed in unsaturated fractured rock. They measured average film thicknesses and velocities as a function of matric potential on a rough fracture surface. The film velocities measured were on the order of 1000 times faster than pore water velocity under unit gradient saturated flow through the rock matrix. For cases where film flow in fractures is significant, conceptual models based on the aperture distribution may not correctly predict unsaturated flow in fractures.

In the experiments summarized in this section, the effects of the rock matrix were incorporated in only one of the experiments conducted by *Kneafsey and Pruess* (1998) and the experiments conducted by *Tokunaga and Wan* (1997). In a homogeneous rock matrix, the total volume of water imbibed per cross-sectional area of the medium is proportional to the square root of time. Imbibition was also found to follow a linear relationship with the square root of time even in a heterogeneous rock matrix (*Tidwell et al.*, 1995). *Pruess* (1999) theoretically examined the significance of matrix imbibition in fractures for flow that occurred locally and episodically and found that the rate of matrix imbibition is small compared to rates that would occur if flow occurred as a spatially uniform sheet over long periods of time.

1.5. Research Objectives

The understanding of flow and transport in unsaturated fractures has undergone much development in recent years, but more work is still needed to better characterize the mechanisms controlling flow and transport. Flow mechanisms have been observed and measured in laboratory experiments that cannot be described by the conventional, macroscale continuum models for flow in unsaturated rock fractures. Laboratory experiments can provide fundamental insight into the important small-scale processes impacting flow and transport in unsaturated fractures.

The research in this dissertation is conducted with the following objectives:

- Identify physical characteristics of liquid seepage in an unsaturated rock fracture with a realistic geometry through flow visualization
- Propose a conceptual model for intermittent flow and characterize this flow behavior
- Study the effect of wettability and/or surface roughness on finger drainage, blob migration, and rivulet flow in unsaturated fractures
- Examine solute transport along preferential flow paths in an unsaturated fracture

1.6. Approach

A transparent replica of a natural fracture is constructed to allow direct visualization of the liquid distribution and flow dynamics in a single fracture with a realistic geometry. During these flow visualization experiments, capillary control is maintained at the inlet of the fracture using a specially designed ceramic endcap. Idealized fractures with controlled apertures are also used in this dissertation to quantitatively examine the important flow mechanisms and features identified in the visualization experiments conducted on the fracture replica. Solute transport along preferential flow paths in variable aperture fractures is also studied by measuring breakthrough curves of a chloride tracer. The fracture is inclined to different angles of inclination in all the experiments to vary the relative strength of gravity and capillary forces.

1.7. Organization of Dissertation

The purpose of this research is to obtain a qualitative and quantitative understanding of physical mechanisms controlling flow and transport in heterogeneous, unsaturated rock fractures at the laboratory-scale. In Chapter 2, a series of flow visualization experiments are conducted on a transparent replica of a natural granite rock fracture. Different boundary conditions, flow rates, angles of inclination and liquids are used to identify the important flow features during unsaturated fracture flow. In Chapter 3, a conceptual model is proposed to explain flow intermittence observed in the visualization experiments where the flow channel would undergo cycles of snapping and reforming. Experiments are conducted to test the conceptual model for intermittent flow and quantitative parameters are obtained from these experiments to characterize this flow behavior. Chapter 4 discusses some theoretical aspects of finger drainage, blob migration, and rivulet flow in unsaturated fractures and the theory is compared with experiments conducted on idealized fractures with different wettabilities and surface roughnesses. Laboratory tracer tests are conducted in Chapter 5 to investigate solute transport in unsaturated fractures. Breakthrough curves from different fractures are measured and analyzed at varying angles of inclination. Finally, conclusions drawn from the results of the previous chapter are summarized in Chapter 6, and suggestions for future work are given.

2. Flow Visualization Experiments on Liquid Seepage in Unsaturated, Rough-walled Fractures

2.1. Introduction

Field studies have provided considerable evidence that water proceeds along fast flow paths through partially saturated fractures (*Liu et al.*, 1995, *Wang et al.*, 1993, *Nativ et al.*, 1995). These observations were explained by water migrating rapidly along localized preferential flow paths through unsaturated rock fractures. Preferential flow channels reduce rock matrix-fracture interaction compared to models which predict spatially uniform flow, thereby accelerating water travel in unsaturated fractured-porous media (*Glass et al.*, 1995). Understanding the mechanisms controlling fast flow is important for developing conceptual models describing seepage of liquids through unsaturated, fractured porous media.

Liquids in unsaturated porous media migrate under the combined action of gravity, pressure, capillary, and viscous forces. At the macroscopic scale, Richards' equation (*Richards*, 1931) has been used to describe flow in unsaturated fractures, based upon the conceptual model that views a fracture as a two-dimensional porous medium. In the conventional approach to describing flow through unsaturated fractures, the fracture is volume averaged over a large scale and modeled as smooth parallel plates (*Peters and Klavetter*, 1988). This approach predicts that the liquid will proceed with a spatially uniform infiltration front, subject to strong capillary imbibition effects from the rock matrix that draws the flowing liquid from the fracture (*Nitao and Busheck*, 1991; *Wang and Narasimhan*, 1993). Actual rock fractures have rough walls and variable apertures with numerous asperity contacts. The aperture variability controls capillary effects and thereby multi-phase distribution in fractures (*Pruess and Tsang*, 1990). Flow behavior dependent upon small-scale aperture distribution, such as preferential flow, is not predicted by these conventional models.

Preferential flow is the focusing of flow into narrow channels or fingers. Laboratory, field, and theoretical studies have demonstrated the occurrence of preferential flow in both

saturated fractures (e.g. *Neretnieks et al.*, 1982; *Abelin et al.*, 1987; *Tsang and Tsang*, 1987; *Brown et al.*, 1998) and partially saturated fractures (e.g. *Scanlon*, 1992; *Nicholl et al.*, 1994; *Pruess*, 1998). Flow channeling through saturated fractures is fairly well-understood, but the theory for flow through fractures under multiphase conditions is still undergoing much development.

Models based on macroscale continuum concepts of flow through unsaturated fractures average flow processes and constitutive properties over a control volume. The ability of these models to describe liquid seepage in fractures must be tested against experimental observations, to see whether or not averaging overlooks phenomena that may be controlling factors in transport predictions. In this chapter, flow visualization experiments are conducted in a transparent replica of a natural rock fracture to identify the phenomenological aspects of water seepage in a rough-walled fracture. A natural fracture obtained from the field is used in this research to bring out the influences of realistic geologic heterogeneity on the flow behavior and liquid distribution. These aspects may be overlooked in more idealized systems, such as the analog fractures used by *Schwille* (1988) and *Nicholl et al.* (1994).

2.2. Experimental Approach

Four flow visualization experiments were conducted in a 21.5 cm x 33 cm sized transparent replica of a natural granite fracture obtained from the Stripa Mine, Sweden to study the liquid distribution and behavior of seeps under the following conditions:

1) Experiment 2.1: different angles of inclination
2) Experiment 2.2: varying the inlet pressure head
2) Experiment 2.3: varying the liquid properties
4) Experiment 2.4: one half of the fracture replica mated with actual rock fracture

The experimental conditions are summarized in Table 2.1 and in Figures 2.1 – 2.3. The transparent replica was an epoxy cast (Eccobond 27, W. R. Grace Co., Canton, MA) made from a silicone mold (Rhodorsil RTV 1556, Rhone-Poulenc, Inc., Monmouth Junction, NJ) of both fracture surfaces. Both the silicone mold and epoxy cast were cured at room temperature.

Details of the casting procedure, originally developed by *Gentier* (1986), are described in *Persoff and Pruess* (1995).

The advantages of using epoxy casts are that they allow direct observation of liquid flow behavior and they provide an accurate reproduction of the fracture surface topography, as was demonstrated in a comparison of profilometry measurements with a 10 μm resolution of a rock and its epoxy cast (*Persoff and Pruess*, 1993). The epoxy replicas differ from natural rock fractures in several respects. Small-scale surface roughness below the resolution of the profilometer is not reproduced on the replica. The stress-state and mating of the fracture replica halves is different from the in-situ rock conditions, which may affect the aperture and asperity contact distributions. This problem also exists for laboratory testing of actual rock fractures where the stress state has changed from in-situ conditions. The casts provide the general geometric features of the fracture surface, and results must be interpreted based upon the laboratory-measured aperture distributions.

The difference in surface chemistry of the epoxy compared to the natural rock and the impermeability of the epoxy cast affect the wettability of the surfaces to water. The contact angle of water on cast epoxy is approximately 63° (*Geller et al.*, 1996), which falls in the range of intermediate wettability as defined by *Dullien* (1988). For conditions of intermediate wettability, spreading of films may be prevented. *Tokunaga and Wan* (1997) demonstrated that water film flow along natural fracture surfaces may also be an important mechanism controlling fast flow through unsaturated fractures. Water wetted a smooth granite surface relative to air with a contact angle closer to that of water on the smooth epoxy surface, than water on glass (*Geller et al.*, 1996), which is commonly used as an analog for natural rock surfaces (e.g. *Nicholl et al.*, 1994). *Geller et al.* (1996) observed that a drop of water spreads spontaneously on the fracture surface of the same granite rock, indicating that near-surface porosity in natural rocks may significantly affect wetting behavior.

The fracture replica was compressed between two transparent lucite plates that were held together by aluminum flanges during Experiments 2.1 and 2.3 (see Figure 2.1). In Experiment 2.2, a gasket was placed between the replica and lucite plate to load the fracture with 35 kPa gas pressure, modified from the design used by *Nicholl et al.* (1994).

Table 2.1. Experimental Conditions

Exp.	Flow cell	Liquid	Inlet flow rate[(a)], Q (ml/hr)	Angle of inclination, β	Comments
2.1	fracture replica	Water	2.0	19°, 46°, 81.5°	Compressed between ½" lucite plates. Ceramic endcap across middle third of inlet and liquid supplied by syringe pump.
2.2	fracture replica	Water	1.3 to 6.1	70°	35 kPa nitrogen confining pressure. Ceramic endcap across middle third of inlet and liquid supplied by Mariotte bottle.
2.3	fracture replica	PCE	2.0	19°	Compressed between ½" lucite plates.
		n-dodecane	2.0	23°	Ceramic endcap across middle third of inlet and liquid supplied by syringe pump.
2.4	Fracture replica with rock	Water	2.0	31°	Replica mounted to rock by four adjustable screws. Filter paper was placed across top third of inlet and liquid supplied by syringe pump

[(a)]Flow rate that the fracture equilibrated to after approximately 24 hours

Gas confining pressure was used in Experiment 2.2 to examine the sensitivity of the flow distribution to the fracture loading. In Experiment 2.4, a special holder was constructed to clamp the rock in place because of the large size of the rock. The fracture was loaded quite differently for this experiment. A ¼ inch thick glass plate and the aluminum flange were placed over the replica and held in placed by mounting screws which pressed down onto the flange as shown in Figure 2.2. Part of the fracture replica was obscured by the flanges, resulting in a total visible area of 19 x 30.5 cm.

The fracture replica was washed in hot water with Liquinox, rinsed with distilled water, rinsed with methanol, and allowed to dry at least an hour before assembling it for each experiment. Filter paper or felt was placed at the outlet of the fracture to promote drainage of the water in the experiments. This assembly was mounted over a light table with an adjustable angle and observations were photographed with a 35 mm SLR camera (Nikon, model N8008) or video camera (JVC KY-F55BU with lens JVC TY-10x6 MDPU) to obtain better resolution of time-dependent behavior. The video recorder (Sony SVHS no. SVO-5800) had time coding, which provided a temporal resolution of 1/30 s. Digital images were acquired from the videotape after the experiment with a frame grabber (Truevision, Targa 16/32 +F with Diaquest software controller) and measurements on the images were made with Adobe Photoshop® 3.0 for Windows. In all the experiments, the liquids were dyed to improve visualization and the dyed liquid properties are summarized in Table 2.2. In Experiments 2.1and 2.2, de-aired distilled water was dyed with 0.2% by volume Liquitint Patent Blue (Milliken Chemical, Inman, SC). The presence of the dye lowered the surface tension and contact angle on the epoxy relative to pure water. The liquids used in Experiment 2.3, n-dodecane and PCE, were dyed with 0.5 g/L Spectra-red (Spectra Colors Corp., Kearny, NJ). Water was dyed with 1 g/L fluorescein (MCB Manufacturing Chemists, Inc.) and imaged under near-UV light during Experiment 2.4.

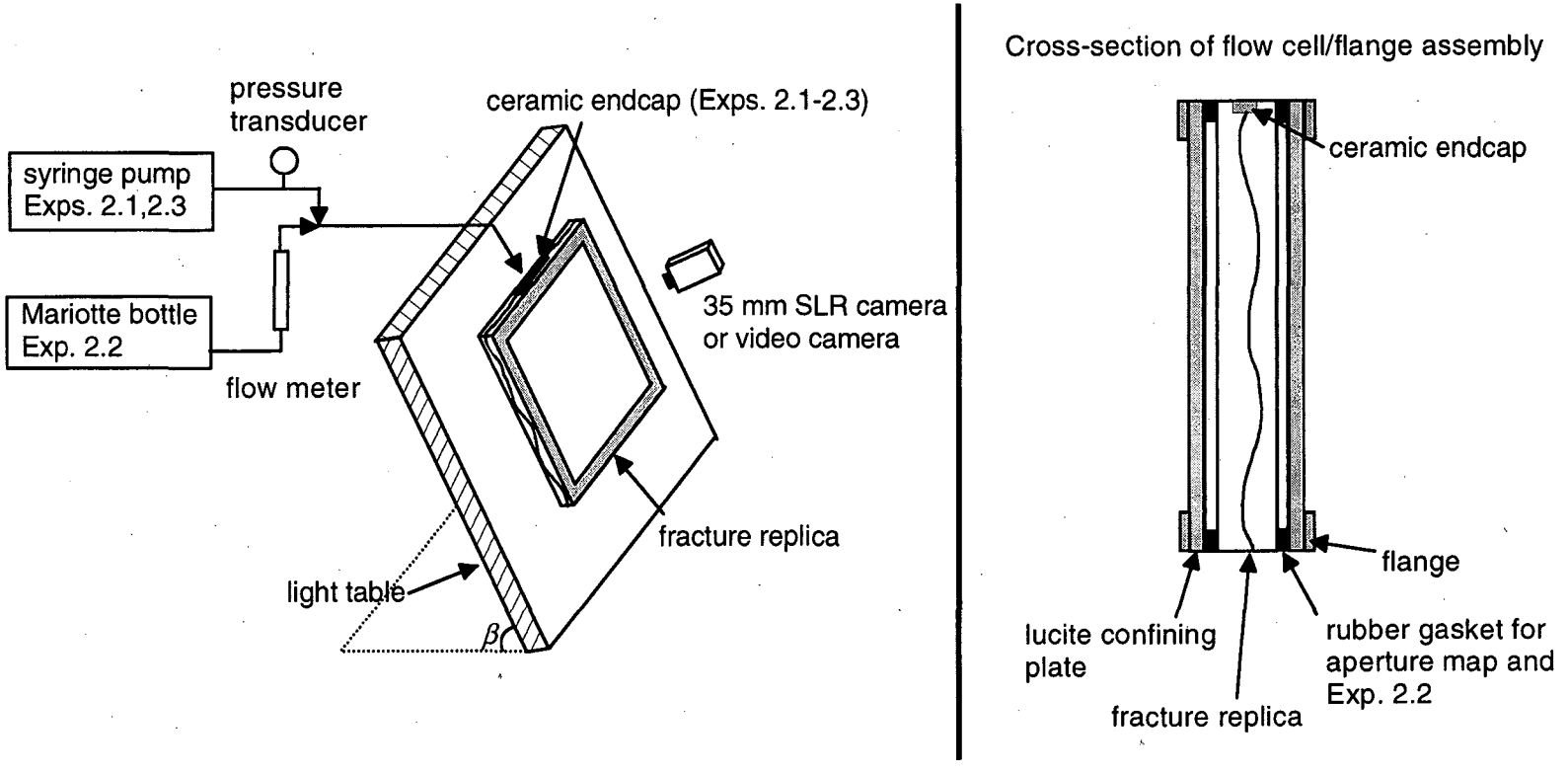

Figure 2.1. Schematic of apparatus for Experiments 2.1 – 2.3 and the cross-section of the flow cell/flange assembly.

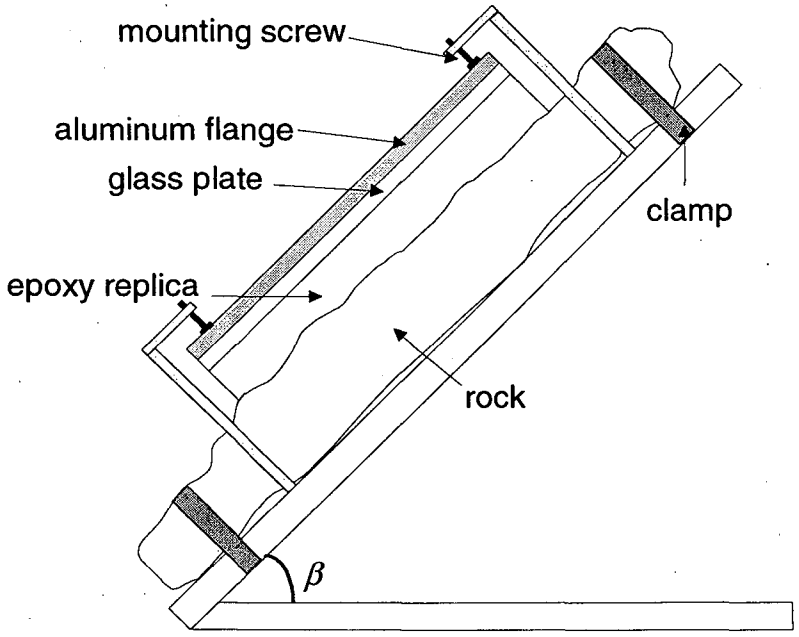

Figure 2.2. Schematic of the apparatus for Experiment 2.4 (rock-replica combination).

Table 2.2. Properties of Dyed Liquids at 20°C

Liquid	Density (kg/m^3)	Viscosity (kg/(m-s))	Surface Tension[(a)] (mN/m)	Contact angle on cast epoxy (deg)[(b)]
Water with 0.2% Liquitint	998	1.002×10^{-3}	66.4	63
Water with fluoroscein dye	998	1.002×10^{-3}	70.7	*NA*
n-Dodecane[(c)]	745	1.378×10^{-3}	25.2	0
PCE[(c)]	1560	0.711×10^{-3}	31.2	0

[(a)] measured with a CSC Du Nouy Tensiometer (CSC Scientific Company, Inc., Fairfax, VA)
[(b)] measured with a goniometer (Ramé-Hart, Inc., Mountain Lakes, NJ)
[(c)] dyed with 0.5 g/L Spectra-red
NA: Not available

In order to maintain capillary control at the inlet, a ceramic endcap designed for two-phase flow experiments (*Persoff and Pruess*, 1995) was placed in the center third of the fracture inlet to deliver water to the fracture edge (Figure 2.3). The ceramic (Soil Moisture Corporation, Santa Barbara, CA) had a 50 kPa air entry pressure and consequently remained water saturated for capillary pressures below that value. Ambient air flowed freely in and out of the fracture edge through grooves milled into the sides and bottom of the endcap, thereby maintaining atmospheric air pressure at the fracture inlet. A tunnel was drilled lengthwise across the endcap so that the water could be distributed uniformly to the ceramic material across the length of the endcap. The water was delivered to the edge of the fracture through the teeth of the endcap. A second opening to the channel was used to withdraw the air initially present. The ceramic endcap was saturated with water prior to placing it into the opening in the fracture edge. In Experiment 2.4, filter paper (Whatman glass microfibre filters GF/D, Clifton, NJ) instead of the ceramic endcap was placed

at the inlet since the inlet opening was too small to hold the endcap. In Experiments 2.1, 2.3, and 2.4 a syringe pump (Model 33, Harvard Apparatus, South Natick, MA) delivered the dyed water into the inlet. In Experiment 2.2, dyed water was supplied with a constant head Mariotte bottle, which allowed the inlet pressure to be varied by adjusting the height of the Mariotte bottle. Flow rates to the inlet endcap were measured using a variable area flowmeter in Experiment 2.2 (Gilmont shielded flowmeter, micro, Cole Parmer, IL). In Experiment 2.1, the pressure at the inlet was measured relative to atmospheric pressure with a differential pressure transducer (DP15-22, Validyne Engineering Corp., Northridge, CA) connected to a pressure tap glued into the center of the ceramic plate.

2.3. Aperture Distribution Measurement

The aperture distribution of the fracture replica used in the flow visualization experiments was measured from the light intensity map of the image of the fracture saturated with water dyed with Liquitint, normalized by the image of the fracture saturated with clear water. The dye concentration was set to 0.2% to establish the best resolution of the estimated aperture range. The attenuation of light varies with the distance the light travels according to Beer's law, and was correlated to the width of open space of the fracture by calibration to the intensity of light transmitted through known apertures filled with the same liquids. The same technique was used by *Nicholl and Glass* (1994) and *Persoff and Pruess* (1995).

The calibration apertures were constructed with glass plates separated by shims of known thickness. Images were acquired with a 1024 x 1024 pixel by 12 bit gray-scale digital camera (SpectraSource Instruments, MCD1200, Westlake Village, CA), with a 35 mm f2 AF Nikon lens and an ND2 filter. The fracture was mounted over a halogen light table (VP 400 Floor Illuma, Bencher, Wood Dale, IL). The height of the camera was adjusted so the length of the fracture fills the field of view. A spatial resolution of 0.31 mm was obtained for this fracture. Eight images were averaged for each measurement. The images of the fracture saturated with dyed water were normalized

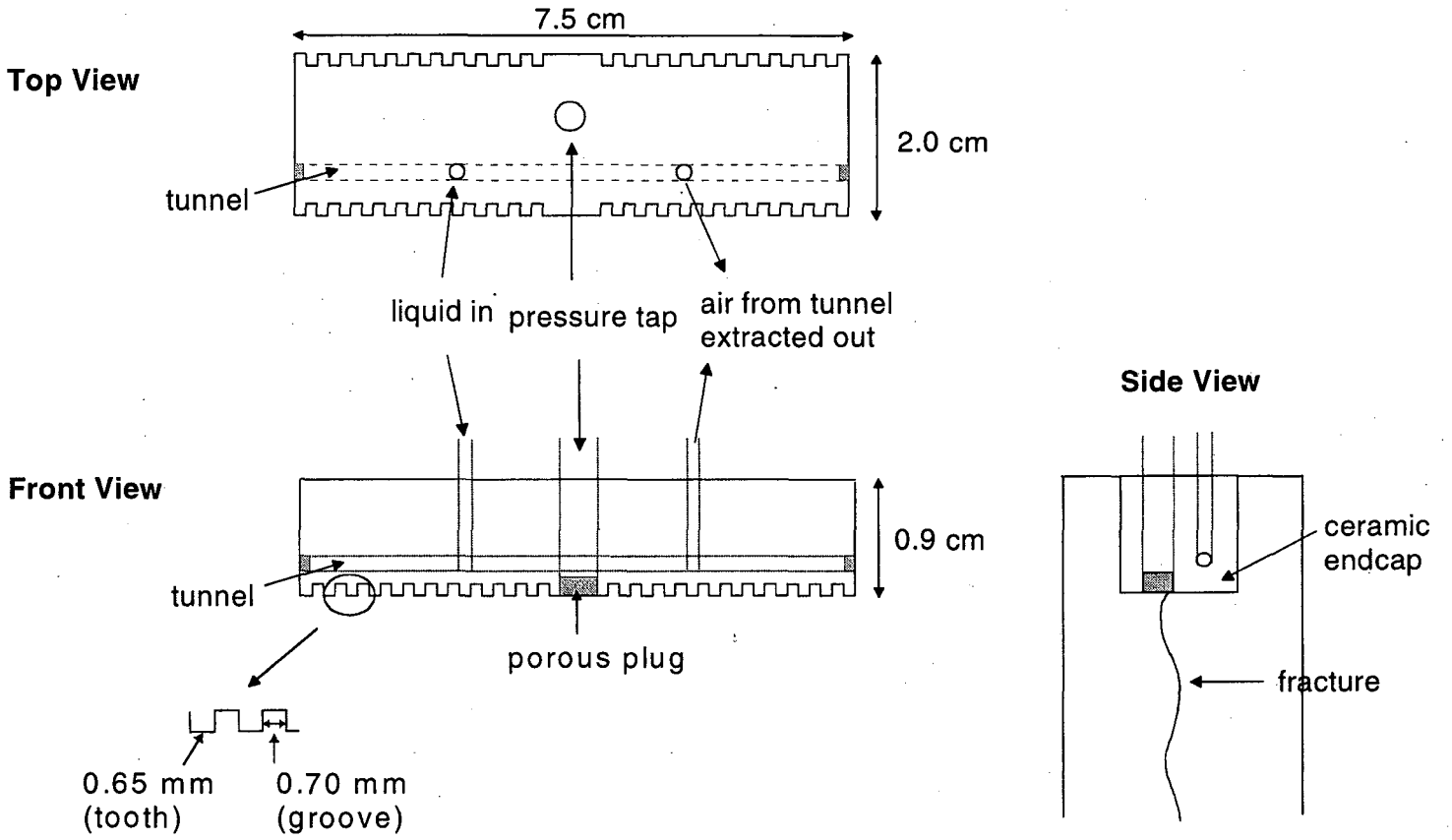

Figure 2.3. Detail of ceramic endcap used in Experiments 2.1 - 2.3 (modified from *Persoff and Pruess*, 1995). Liquid is distributed uniformly to the fracture inlet through the teeth of the endcap, while the grooves allow air to flow freely in and out of the inlet.

with the software that drives the camera and further processed with Global Lab Image (Data Translation, Marlboro, MA). The total pore volume of the fracture was computed from the binary image file, using the calibration curve of aperture width to light intensity. The apertures were calibrated over a range between 0.013 - 2.04 mm.

The fracture was saturated with de-aired water after initially flushing it with CO_2. Full saturation occurred after about two weeks, during which time approximately 650 L of water were pumped through the fracture. Images of the fracture saturated with clear water were made of the fracture without, and then with, 35 kPa gas confining pressure. Afterwards, the gas confinement was relieved and the fracture was saturated with dyed water. The fracture was determined to be saturated with dyed water by comparing consecutive measurements of light intensity as a function of the volume of dyed water injected, until there was no detectable difference. This took two days at a flow rate of 0.5 ml/min, for a total volume of approximately 1.5 L.

The aperture maps of the fracture replica are shown in Figures 2.4a and b. The maps are aligned in the same position that the fracture replica is during the flow visualization experiments described in this chapter. The general structure of the aperture distribution consists of a region of small apertures in the top and middle of the fracture that form a gently swirling region down the center of the fracture and to the lower edges. These smaller apertures, which presumably include asperity contacts, support the more open regions on the left and right sides of the fracture. The apertures are larger under gas confining pressure except along the edges near the rubber gasket, indicating that the gas confinement caused some buckling of the fracture. Since the fracture replica was cleaned and reassembled before each flow visualization experiment discussed in this chapter, the actual aperture distribution in these experiments may be slightly different from the aperture maps. Reflection and refraction of light also affects the accuracy of these measurements. The maps do, however, provide good definition of the relative magnitude of the apertures in this fracture replica.

The arithmetic mean aperture computed from the light intensity image for the fracture without confining pressure was 0.16 mm $\pm$ 0.11 mm (standard deviation), giving a total pore volume of 9.4 ml, and with the confining pressure the mean aperture was 0.17 mm $\pm$ 0.09 mm

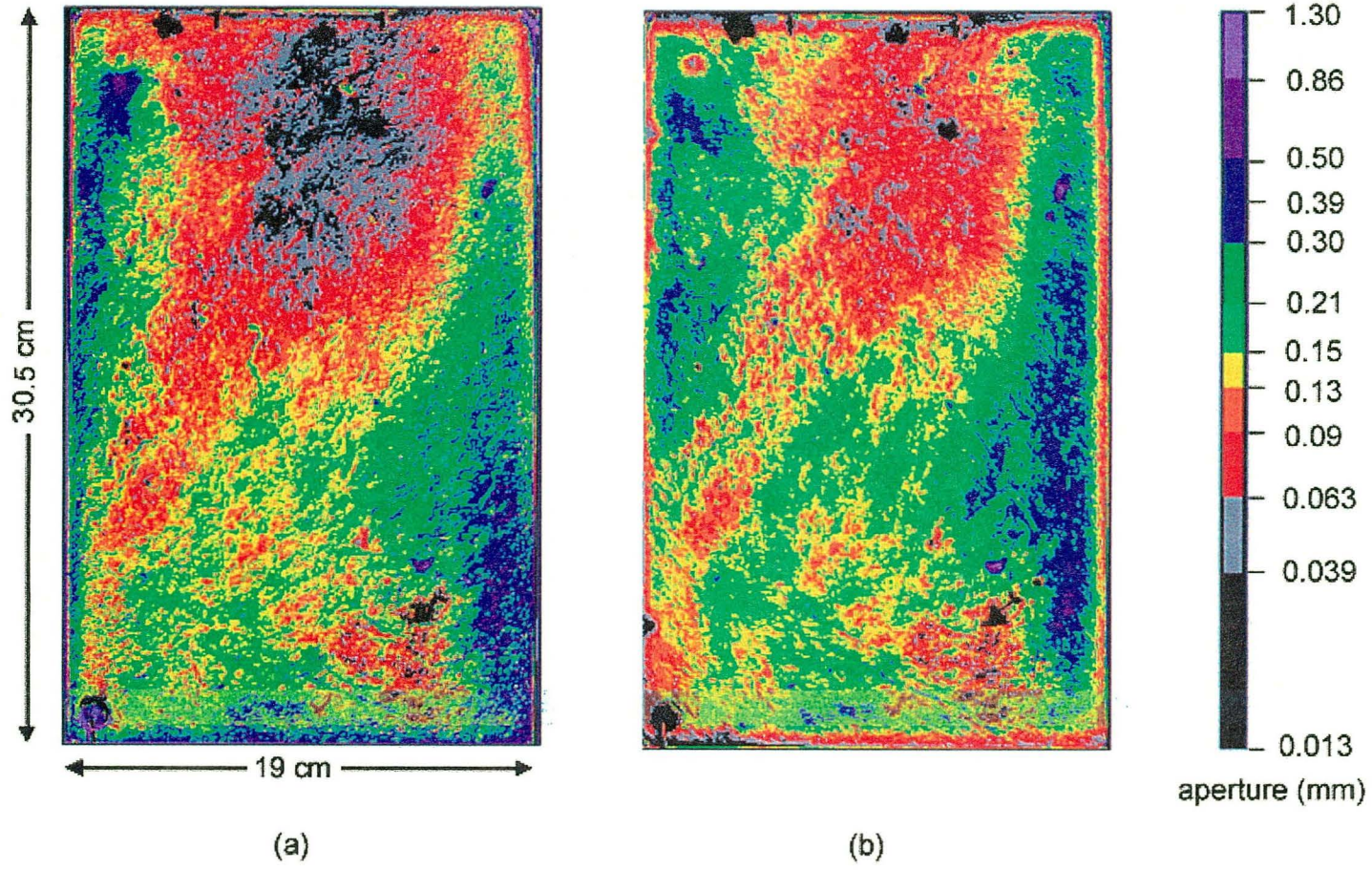

Figure 2.4. Aperture distribution maps of epoxy fracture replica. (a) Without confining gas pressure. (b) With 35 kPa confining gas pressure. Measurements were made without reassembling the fracture. Gas confinement caused some buckling of the fracture replica, resulting in the larger apertures seen in (b).

(standard deviation), giving a total pore volume of 9.5 ml. These small differences reflect the fact that the smallest apertures changed more significantly between the fracture with and without confining pressure. These values are for the exposed fracture only, and do not account for the fracture space obscured by the top and bottom flanges.

Fracture transmissivity, defined as the saturated hydraulic conductivity, K_s, multiplied by the average aperture width of the fracture, b, was measured with and without gas confining pressure from the linear regression of flow rate versus the pressure drop across the length of the fracture:

$$Q = -TW\frac{dh}{dx} = -K_s bW\frac{dh}{dx} \tag{2.1}$$

where Q is the flow rate, dh/dx is the pressure drop across the fracture, and W is the width of the fracture sample (21.5 cm). The saturated hydraulic conductivity of a fracture is given by the following relationship:

$$K_s = \frac{T}{b} = \frac{\rho_l g b^2}{12\mu_l} \tag{2.2}$$

whereρ_l is the density of the liquid, μ_l is the viscosity of the liquid, and g is the gravitational acceleration constant. Solving Equation 2.2 for b in terms of the measured transmissivity, one can calculate the average aperture of the fracture:

$$b = \left(\frac{12\mu_l T}{\rho_l g}\right)^{1/3} \tag{2.3}$$

The aperture obtained from Equation 2.3 is generally referred to as the hydraulic aperture. The measured transmissivity of the fracture was 0.258 cm^2/s without confining pressure and 0.207 cm^2/s with the gas confining pressure. The corresponding hydraulic apertures calculated from the

transmissivities were 0.31 mm and 0.29 mm, respectively. The hydraulic aperture measured under gas confining pressure was less than the value measured without the confining pressure, contrary to the aperture distribution shown in Figure 2.4. The edges of the fracture were compressed under gas confinement, resulting in some buckling of the fracture and the larger apertures in the center of the fracture shown in Figure 2.4b.

2.4. Summary of Visual Observations

This section describes the liquid distribution and behavior observed in the four flow visualization experiments conducted in the epoxy fracture replica. In the images obtained from Experiments 2.1 –2.3, the dark gray regions are assumed to be completely liquid saturated, except for the very pale gray areas adjacent to areas of darker gray (Figures 2.7 and 2.8), which indicate the presence of a water film or residual dye from water that has evaporated on the replica surface. The variation in the intensity of the gray reflects a change in aperture. The larger apertures have increased light attenuation, resulting in a darker color, while smaller apertures produce a lighter color.

2.4.1. Experiment 2.1: Varying Angle of Inclination with Constant Inlet Flow Rate Condition

Images of the initial invasion of water at 4 ml/hr into the initially dry fracture inclined at 19° from the horizontal are shown in Figure 2.5. Water enters the fracture non-uniformly, shown in Figures 2.5a and b, filling a region of the fracture immediately below the inlet plate. About 750 seconds after water is introduced, two small fingers begin to form below this broad, water-filled region or "capillary pool" (Figure 2.5c). Only one of these fingers eventually grows and forms a highly localized flow path extending down the middle of the fracture (Figures 2.5d – 2.5h). The initial finger drains as it progresses down the fracture (Figures 2.5f – 2.5h), leaving a film of water along the sides of the flow channel. Finger drainage under continuous liquid application has also been observed and measured in unsaturated porous media (e.g. *Glass et al.*,

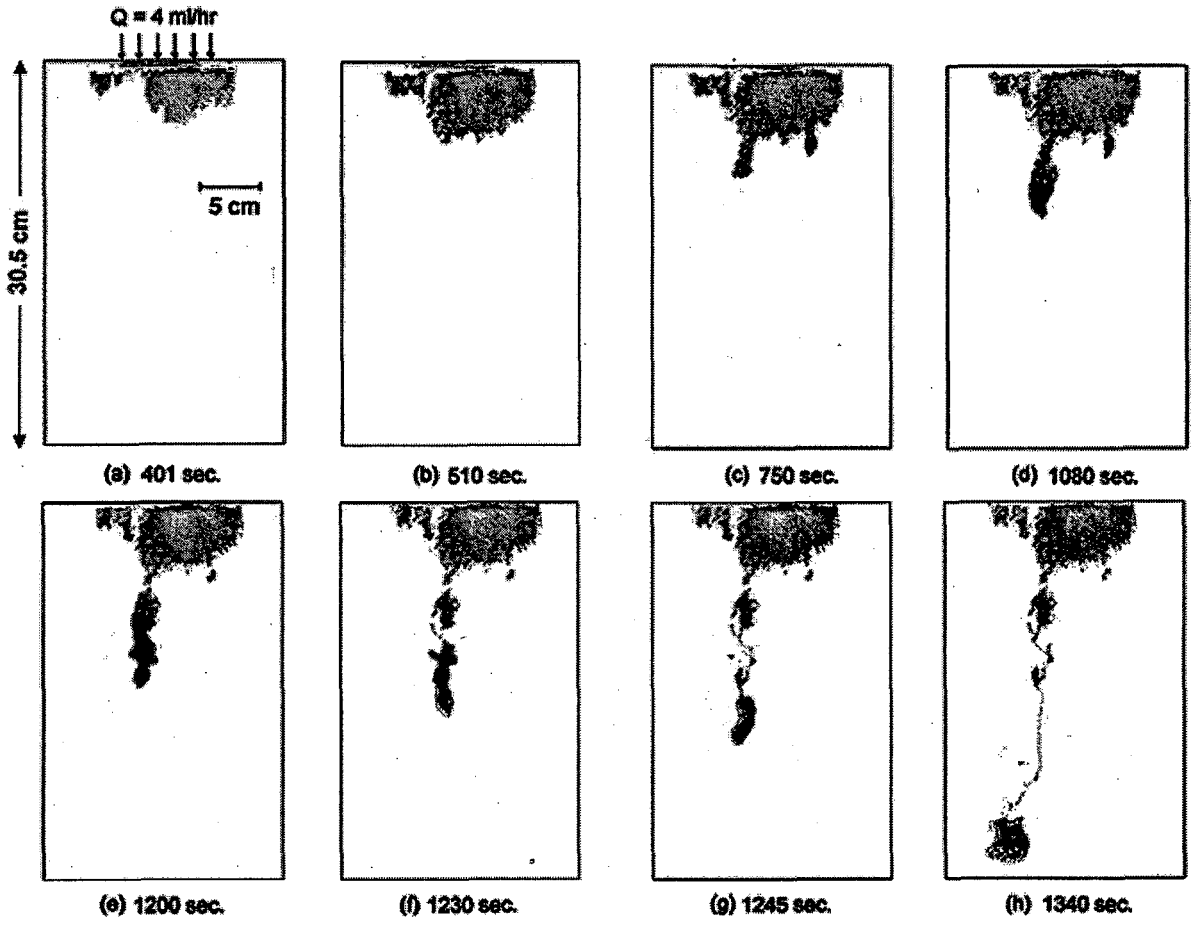

Figure 2.5. Water invasion into the initially dry fracture replica during Experiment 2.1, $\beta = 19°$ and $Q = 4$ ml/hr. Time denotes seconds after water was introduced into the fracture.

1989c; *Selker et al.*, 1992) and in unsaturated analog fractures (*Glass and Nicholl*, 1996).

The finger reaches the outlet of the fracture, traveling a total distance of 30.5 cm, in approximately 1340 seconds from the time the water is introduced into the fracture. These values correspond to an average seepage velocity of 0.02 cm/sec or 1.4 cm/min for the initial invasion. After the initial finger reached the fracture outlet, a constant flow rate of 2 ml/hr was applied to the fracture, resulting in a pressure at the fracture inlet of approximately -2.0 cm at the three angles of inclination. The flow rate was lowered from the rate used during the initial invasion to ensure that enough water was available for the duration of the experiment without having to refill the syringe pump.

The flow channel in Figure 2.5h consists of capillary pools connected by thin threads or rivulets of water. Some of the rivulets are so thin that it is difficult to see the connections between the capillary pools. A comparison of the water distribution at 19° (Figure 2.5) with the aperture map in Figure 2.4a shows that the capillary pools are located in portions of the fracture with smaller apertures, where capillary forces are large enough to induce lateral flow. The rivulets form in regions of the fracture where the apertures are relatively larger.

The fracture replica was initially inclined to 19° and then to 46° and 81.5° on consecutive days. The fracture was reassembled and cleaned between 19° and 46°, and then subsequently raised from 46° to 81.5° without reassembling it. Photographs of the water distribution in the top half of the fracture after flow had equilibrated at the three different angles of inclination are shown in Figure 2.6. The width of the flow channel decreases significantly as the angle of inclination increases, and a larger portion of the flow channel consists of rivulets. The reduction in lateral spreading occurs only in the capillary pools while the rivulets remain the same width regardless of the angle of inclination. The increase in gravity driven water flux relative to capillary forces is responsible for the reduction in lateral spreading of the water filled regions at the higher angles of inclination. Reassembling the fracture between 19° and 46° may have also affected the channel dimensions.

Although great care was taken to maintain uniform and steady boundary conditions at the fracture inlet, the flow of water generally proceeded in an unsteady manner through the flow channel. This unsteady flow behavior occurred at all angles of inclination, where the rivulets

along the flow channel underwent cycles of breaking and reforming. The rivulets typically broke following a period of no observable changes in liquid distribution. Figure 2.7 shows images of one cycle of intermittent flow occurring in the fracture that was inclined to 46°. After snapping, water accumulates behind the advancing air-water meniscus of the finger over a period of 60 seconds (Figures 2.7b – 2.7c) forming a blob. The advancing blob then migrates down the fracture over a period of 10 seconds, leaving behind a rivulet of liquid (Figures 2.7d – 2.7e). Over the 40 minutes that the experiment was videotaped at each angle, the location of snapping consistently occurred at approximately 14 cm below the fracture inlet for all three angles of inclination.

2.4.2. Experiment 2.2: Changing Inlet Pressure Head

Figure 2.8 contains images of the water distribution in the fracture during Experiment 2.2. An image of the liquid distribution in the fracture after a pressure of -3.5 cm was applied to the inlet is shown in Figure 2.8a. A capillary pool is present below the inlet plate and above the right channel due to the small apertures in this region; no such region formed above the left channel since the apertures are larger in this portion of the fracture (see Figure 2.4b). As in Experiment 2.1, the flow channels consist of wider regions of water connected by rivulets. After flow had equilibrated at h_w = -3.5 cm (approximately 24 hours) water continued to flow through the right channel only, while residual water from the initial invasion was held by capillary forces along what had been the left channel. During the initial invasion (not shown), the left-hand channel formed a few minutes after the saturated ceramic plate was placed at the inlet, and the right-hand channel formed after approximately half an hour.

Even though the mean and hydraulic apertures for the fracture with and without gas confining pressure were similar, the location of channeling was very sensitive to the changes in the aperture distribution caused by gas confinement. In Experiment 2.1, one flow path formed close to the middle of the fracture, while in Experiment 2.2, two flow paths formed close to the edges of the fracture. Introducing the water at a higher angle of inclination (70°) may have also created differences in the flow distribution. However, when water was introduced to the same

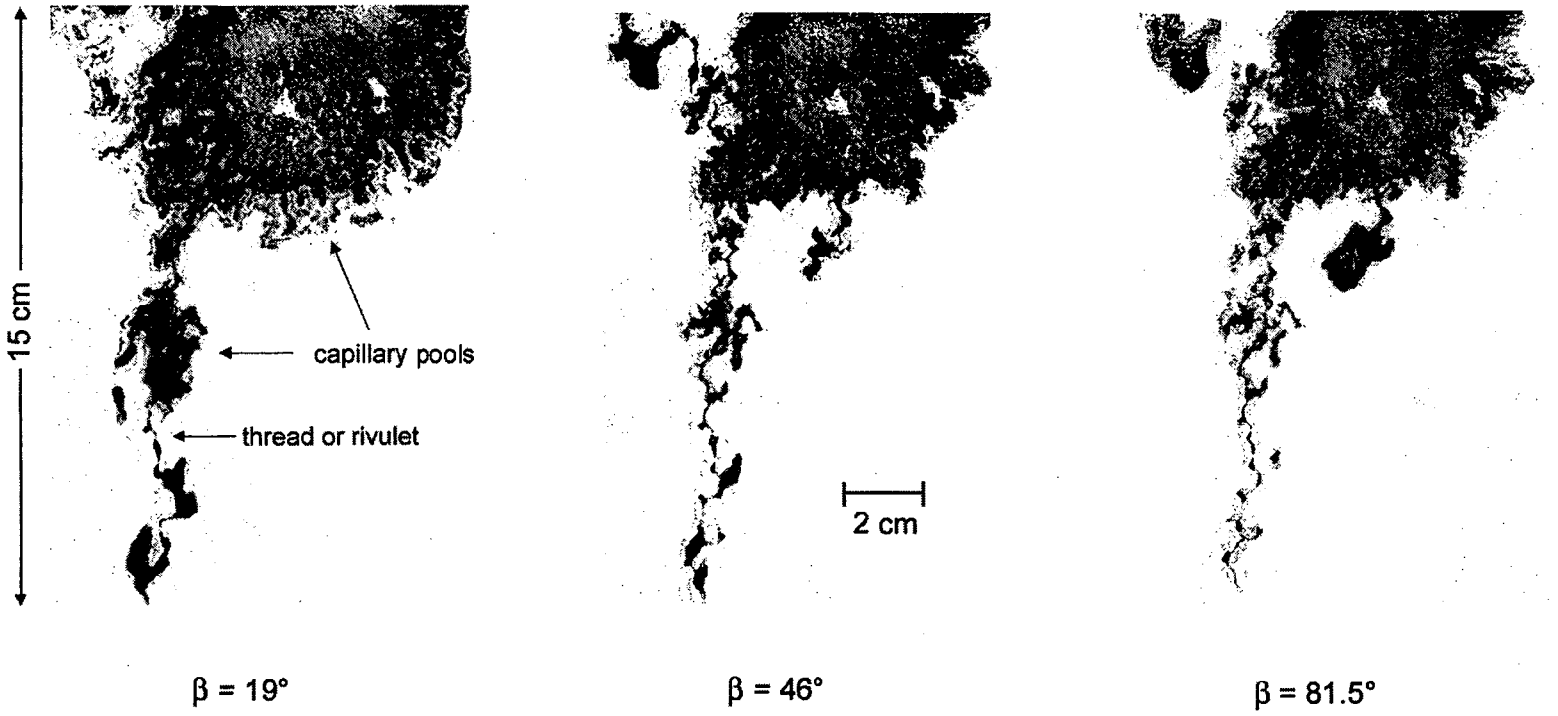

Figure 2.6. Images of the top half of the water distribution at the three angles of inclination during Experiment 2.1 after water had been flowing at each angle for approximately 24 hours. Fracture was disassembled between 19° and 46°, but was raised from 46° to 81.5° without disassembling it. The width of the flow channel decreases as the angle of inclination increases.

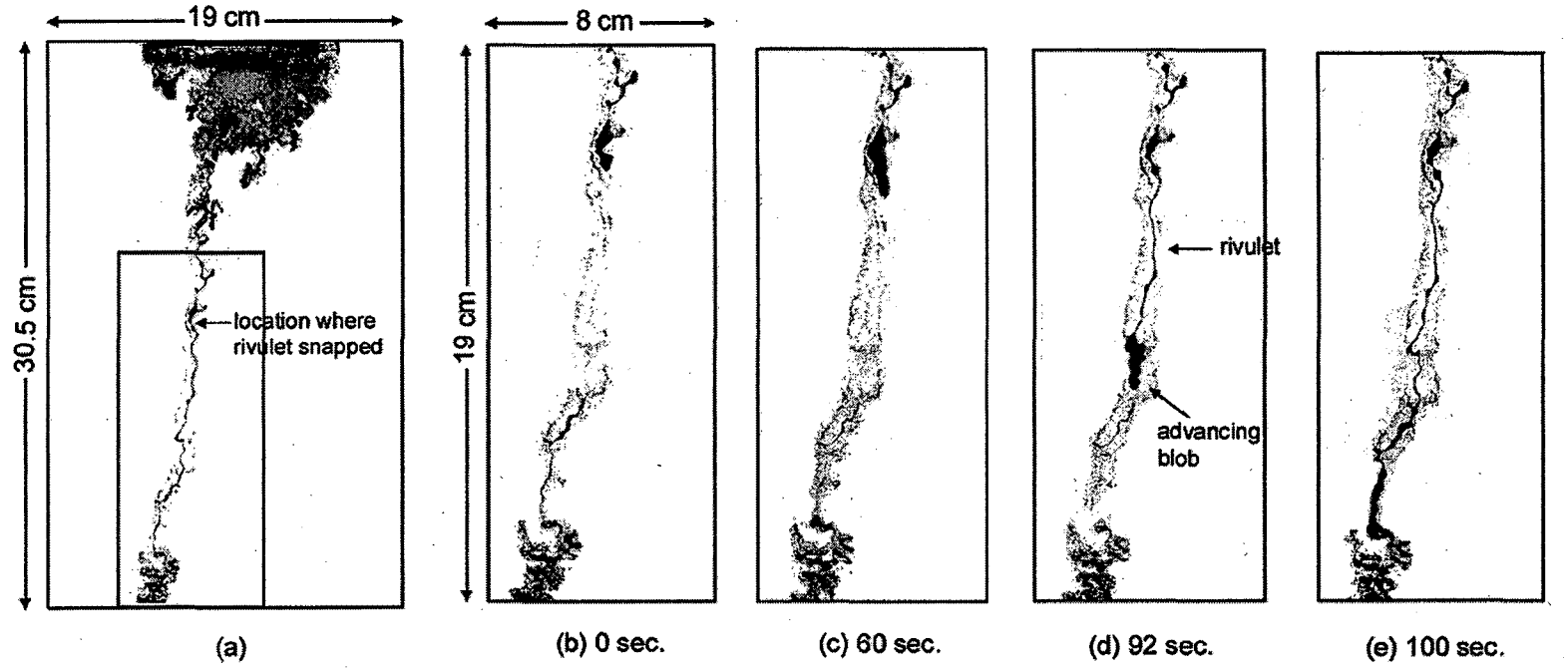

Figure 2.7. Liquid distribution during Experiment 2.1, β = 46° and Q = 2 ml/hr. (a) Full view of the liquid distribution in fracture. (b)-(e) are enlargements of the boxed region in (a) where flow in intermittent. Water accumulates behind the advancing air-water meniscus ((b)-(c)), and then forms a rivulet behind the advancing blob ((d)-(e)). Time indicates seconds after the rivulet had snapped.

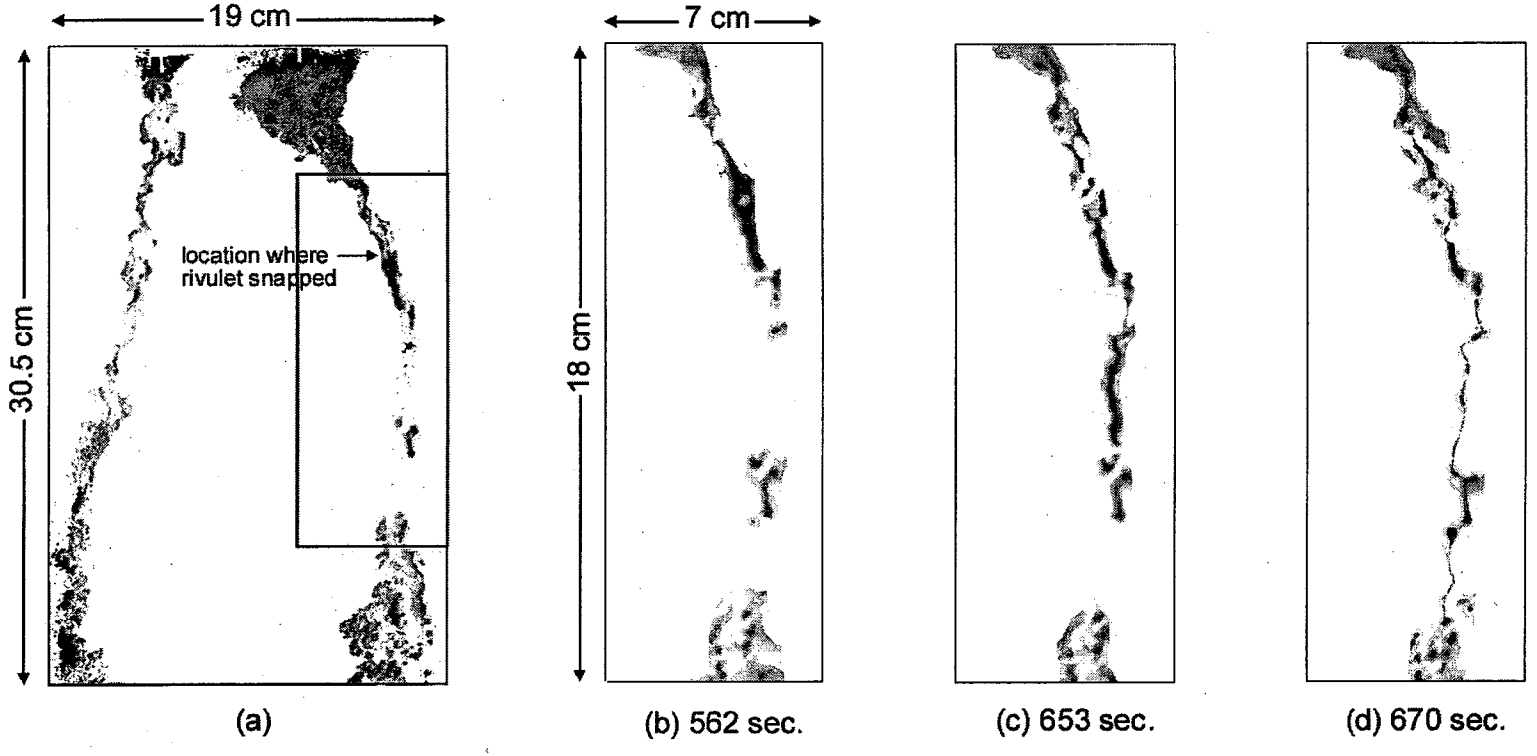

Figure 2.8. Liquid distribution during Experiment 2.2, $\beta = 70°$ and $h_w = -3.5$ cm. (a) Full view of the liquid distribution in fracture. Water only flows through the right channel at this pressure. (b)-(e) are enlargements of the boxed region in (a) where flow is intermittent. Time indicates seconds after the rivulet had snapped.

fracture replica without gas confining pressure at an inclination angle of 70°, the distribution was similar to Experiment 2.1 (*Geller et al.*, 1997).

Intermittent flow was also observed in Experiment 2.2. Figures 2.8b – 2.8d show an intermittent flow event through the right-hand channel at h_w = -3.5 cm. Water accumulates behind the advancing air-water meniscus (Figure 2.8b) and then forms a rivulet behind the advancing blob (Figures 2.8c – 2.8d). The advancing meniscus coalesced with residual water along its flow path before the rivulet snapped about 11 cm below the inlet of the fracture. The following day, the pressure was increased from -3.5 to -2.5 cm and water began to flow through both the left and right channels in an intermittent manner. As the pressure was increased in subsequent days from –1.5 cm to +2 cm in increments of +0.5 cm each day, the liquid distribution in the fracture remained nearly constant. Water continued to flow intermittently through the two flow paths without entering any other regions of the fracture or forming additional channels. At a pressure of +2 cm, flow in the left channel became steady while the right channel remained intermittent. Flow rates measured at each value of h_w are summarized in Table 2.3.

Table 2.3. Summary of Inlet Pressures and Corresponding Flow rates from Experiment 2.2

h_w (cm of H2O)	-3.5	-2.5	-1.5	-1.0	-0.5	0.0	+0.5	+1.0	+2.0
Q (ml/hr)	1.3	1.4	2.1	2.4	4.0	4.6	5.7	6.1	*NA*

2.4.3. Experiment 2.3: Effect of Liquid Properties on Seepage in Fractures

Two non-aqueous phase liquids (NAPLs), n-dodecane and PCE, were used to examine the effect of liquid properties on flow behavior in unsaturated fractures. n-Dodecane is less dense and more viscous than water, while PCE is more dense and less viscous than water. Drops of

these liquids immediately spread upon contact with the epoxy, indicating that both liquids strongly wet the epoxy surface.

Two different runs were conducted where each liquid was introduced into an initially dry fracture replica inclined to angles of 19° and 23°, for n-dodecane and PCE, respectively. Figure 2.9 is the distribution of these two liquids immediately before the finger from the initial invasion reaches the outlet. The flow channels formed in nearly the same location as the channel observed in Experiment 2.1 (Figure 2.6h) and also consisted of wider, liquid-filled regions connected by rivulets of liquid. The flow dynamics of the two NAPLs was different than the water, however. Figure 2.10 contains a sequence of images of the flow channel undergoing intermittent flow during the experiment with n-dodecane after flow had equilibrated to a flow rate of 2 ml/hr. A different mode of intermittent flow occurred in this experiment than the mode observed in Experiments 2.1 and 2.2. With n-dodecane, the rivulet snapped when the weight of the liquid in the advancing blob exceeded the capillary force, similar to a dripping faucet. The disconnected blob of liquid then migrated down the remainder of the flow path towards the fracture outlet. In Experiments 2.1 and 2.2, the flow channel remained steady over the length of the fracture for some time before snapping. The mode of intermittent flow that occurred during the experiment with n-dodecane also occurred with PCE. The rate that flow channels snapped and reformed in the experiments using the NAPLs was much faster than in the experiments with the water. Direct observations of the liquid distribution in the fracture indicated that films of n-dodecane and PCE spread throughout most of the fracture. The spreading of the NAPLs into films probably increased the rate at which the rivulets thinned and eventually snap.

2.4.4. Experiment 2.4: Water Seepage into a Rock-replica Combination

The rock-replica fracture was inclined to 31° for the initial invasion of water at a rate of 5 ml/hr. The water almost immediately began to form a finger below the left side of the inlet. The finger eventually drained, resulting in a finger consisting of a blob and rivulet. The rivulet snapped after the blob advanced about 6 cm down the fracture, leaving very little trapped water along the flow path. A second finger began to slowly form below the right side of the inlet

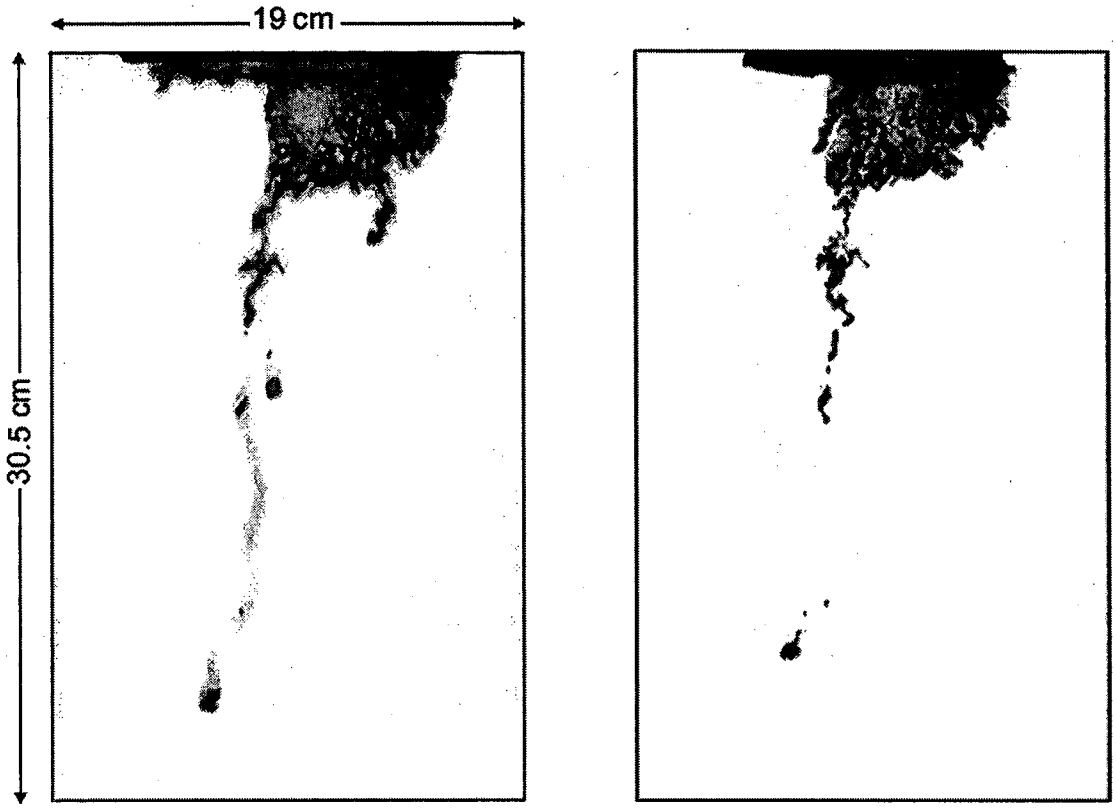

(a) n-dodecane
Q = 4 ml/hr
β = 23°

(b) PCE
Q = 6 ml/hr
β = 19°

Figure 2.9. Liquid distribution during seepage of (a) n-dodecane and (b) PCE into the initially dry fracture replica. Images were taken immediately before the initial invading finger broke through the fracture outlet.

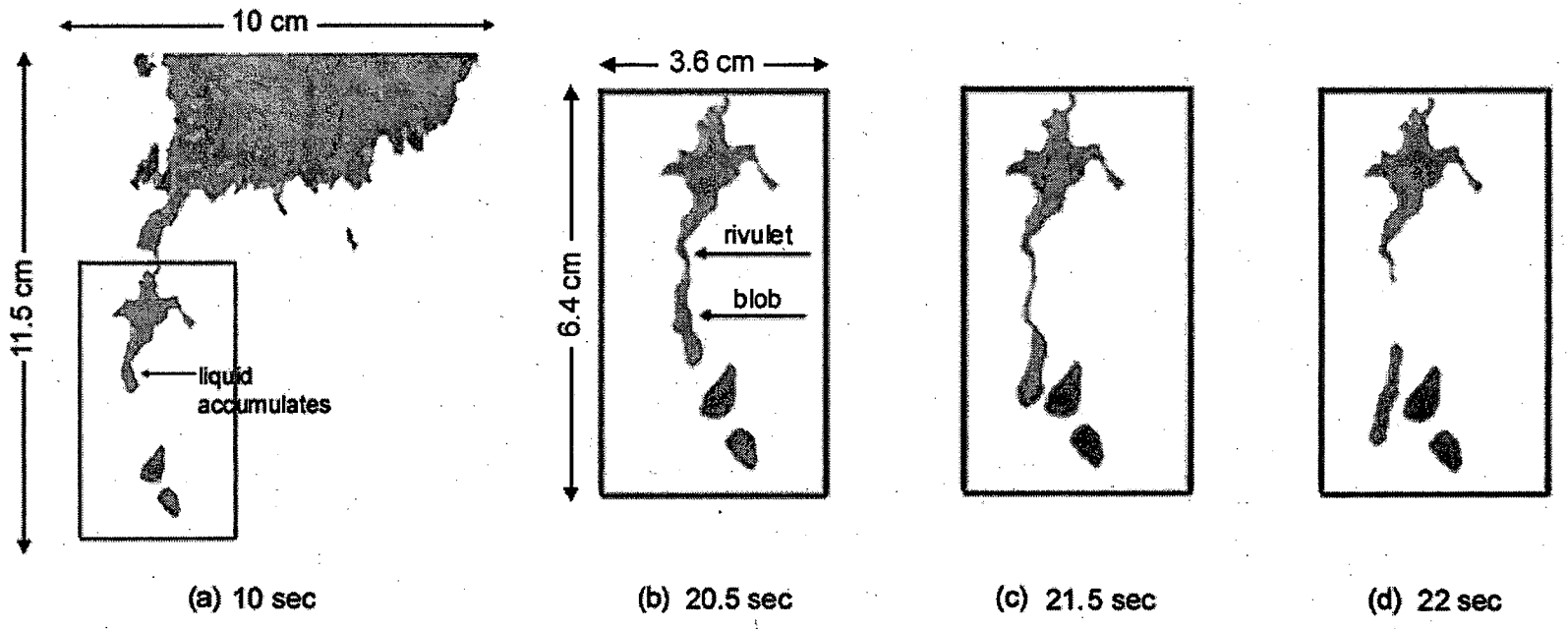

Figure 2.10. Intermittent flow of n-dodecane during Experiment 2.3, $\beta = 23°$ and $Q = 2$ ml/hr. (a) Liquid accumulates into a blob, (b)-(c) forms a rivulet behind the blob, and then (d) the advancing blob of liquid snaps from the weight of the liquid. Time denotes seconds after the previous rivulet had snapped.

after the left finger had snapped. The right finger also formed a blob of liquid which drained to a rivulet and snapped after the advancing blob reached about halfway down the fracture. Only a small drop of water remained entrapped in the fracture after the rivulet snapped. The flow continued to proceed in an intermittent manner through both flow channels at this flow rate. Several hours after the initial invasion, the flow rate was reduced to 2 ml/hr and the fracture was allowed to equilibrate to this rate (~24 hours), where the water only flowed through the right channel and proceeded in an intermittent manner. A sequence of intermittent flow in this rock-replica combination is shown in Figure 2.11. Water accumulates into a blob, and then the rivulet snaps from the weight of the drop, similar to Experiment 2.3.

The major difference in the liquid distribution of this rock-replica experiment compared with the replica only experiments was the lack of trapped water within the fracture, which indicates that the apertures in the rock-replica combination were larger. The capillary pool present near the top of the fracture in Experiments 2.1 – 2.3 was located in a region where the apertures were small, but was not present in this experiment. The fracture was loaded differently in Experiment 2.4, which apparently changed the aperture distribution from the replica only experiments. The effect of the actual rock properties on the liquid distribution is difficult to assess from this experiment since the aperture distribution was so dramatically affected. In saturated fractures, fluid flow has been shown to be affected by the magnitude of the normal stress applied (e.g. *Witherspoon et al.*, 1980; *Pyrak-Nolte et al.*, 1988; *Cook*, 1992). Increasing the magnitude of the normal stress and percentage of asperity contacts resulted in deviations from the cubic law equation.

2.5. Application of Characteristic Curves

The qualitative observations from these flow visualization experiments raise significant questions about approaches to quantitatively describe flow through unsaturated fractures. The multiphase approach for modeling seepage through fractures requires experimental data on the relationship between relative permeability and capillary pressure. If we assume that flow is under

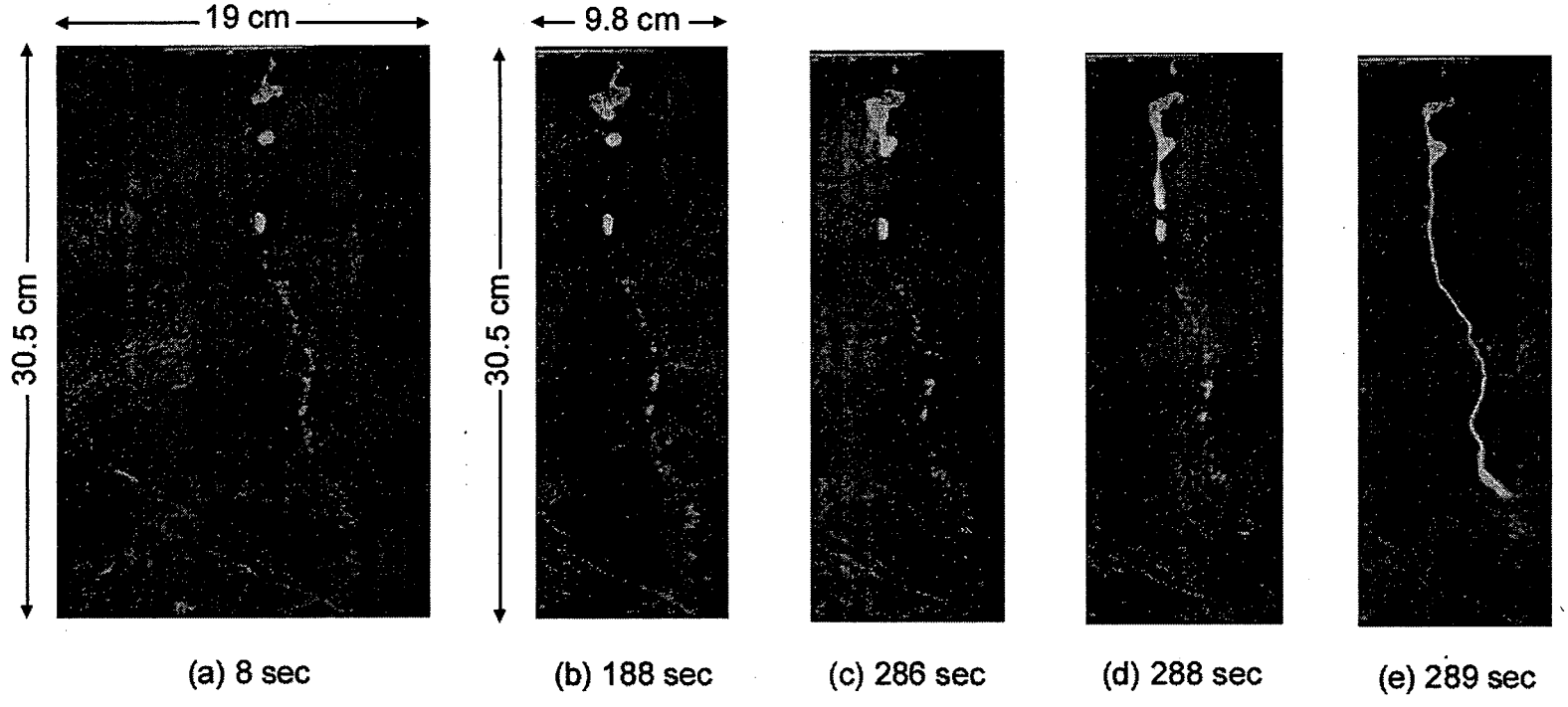

Figure 2.11. Intermittent flow during Experiment 2.4, $\beta = 31°$ and $Q = 2$ ml/hr. (a)-(b) Liquid accumulates into a blob, (c) the rivulet snaps, (d)-(e) blob of liquid migrates down the remainder of the flow path towards the outlet.

unit gradient flow when the inlet pressure heads are less than and equal to zero, relative permeabilities can be calculated from Experiment 2.2 by normalizing the flow rates measured when capillary control was maintained at the inlet ($h_w \leq 0$) by the flow rate measured when h_w = 0:

$$k_{r,l} = \frac{Q_{h_w<0}}{Q_{h_w=0}} \tag{2.4}$$

Theoretically, the relative permeability is unity for non-negative pressures. Figure 2.12 is a plot of the relative permeability as a function of capillary pressure head (P_c = - h_w) using the data from Experiment 2.2.

Capillary control was achieved with the ceramic endcap which had alternating teeth and grooves for water and air to simultaneously enter the inlet at constant pressures. The endcap had a bimodal pore-size distribution because of these grooves, and this affected the inlet conditions. At lower pressures, water only flowed through the teeth and
the grooves were occupied by air (capillary control). At higher pressures, the grooves filled with water, altering the cross-sectional area for flow at the inlet. The conditions of capillary control in Experiments 2.1 and 2.2 were determined by estimating the air entry pressure of the grooves using the Young-Laplace equation (*Adamson*, 1990):

$$P_c = P_{nw} - P_w = \frac{2\sigma}{b}\cos\gamma \tag{2.5}$$

where P_{nw} is the pressure of the non-wetting phase and P_w is the pressure of the wetting phase. The surface tension of the water dyed with 0.2% Liquitint by volume is 0.0664 N/m, the contact angle is assumed to be zero on the ceramic, and P_c = - P_w since the non-wetting phase, air, is at atmospheric pressure. Substituting the measured 0.07 cm groove width in Equation 2.5 for b gives an air entry pressure value of -190 Pa or -1.9 cm. At pressures greater than the air entry pressure, water should fill the grooves of the endcap. Therefore, capillary control was

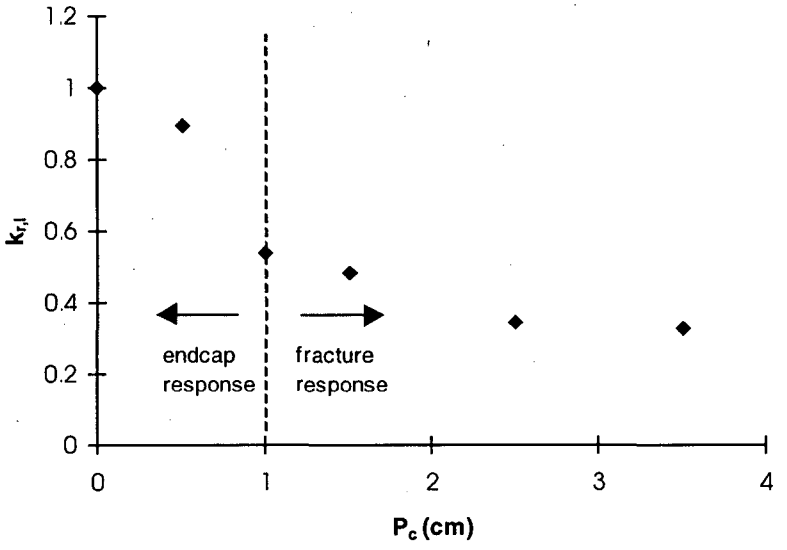

Figure 2.12. Relative permeability as a function of capillary pressure for Experiment 2.2. The data shows the response of the fracture for $P_c > 1.0$ cm and the behavior of the endcap (grooves filled with water) for $P_c < 1.0$ cm.

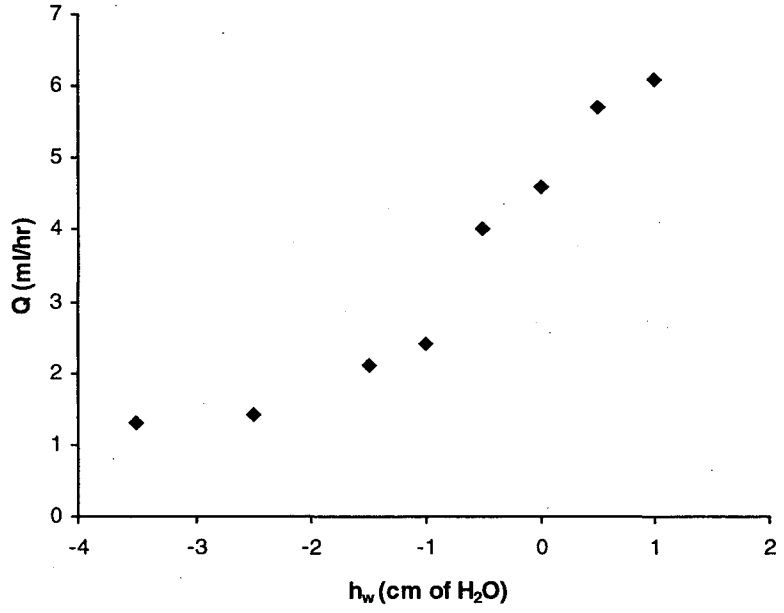

Figure 2.13. Flow rate as a function of inlet pressure head during Experiment 2.2.

maintained in Experiment 2.1, but not for the entire range of pressures used in Experiment 2.2. A plot of the flow rate as a function of inlet pressure from Experiment 2.2 is presented in Figure 2.13 and shows that the flow rate increases non-linearly with h_w above a value of -1 cm, indicating that the endcap grooves had filled above that pressure. Consequently, Figure 2.12 actually shows the response of the fracture when $P_c > 1.0$ cm and the endcap when $P_c < 1.0$ cm.

Capillary control at the fracture boundaries must be maintained to measure relative permeabilities, which can be difficult to achieve at higher wetting phase pressures and when air is at atmospheric pressure. End effects must be carefully examined before applying the capillary pressure-relative permeability curve since they can control experimental results.

2.6. Summary and Conclusions

Three flow visualization experiments were conducted on an initially dry, transparent epoxy replica of a natural rock fracture (replica only). A fourth flow visualization experiment was conducted where one half of the fracture replica was mated to the actual rock (rock-replica). A phenomenological approach was used in these experiments to identify important physical mechanisms controlling seepage of liquids in unsaturated fractures. Experiments were conducted with constant flow rate or constant pressure conditions at the inlet of the fracture, over a range of angles of inclination to vary the relative strength of gravity versus capillary forces.

Highly localized and non-uniform flow channels consisting of broader, water-filled regions or capillary pools, connected by rivulets of liquid were observed in the replica only experiments. The capillary pools drained at higher angles of inclination due to the relative increase in the gravity force. The location of the flow channel was very sensitive to changes in the aperture distribution caused by different confining pressures. The different loading used in the rock-replica experiment affected the location and liquid distribution of the flow channel. The flow channel was located in a different region of the fracture than the flow channels observed in the replica only experiments and very little water became trapped which indicated that the apertures in the rock-replica were larger than the replica only experiments.

The flow generally proceeded in an intermittent manner in all the experiments. Rivulets along the flow channel would undergo cycles of snapping and reforming. Different modes of intermittent flow were observed in the experiments. In the water seepage experiments, the flow channel generally remained steady over the length of the fracture for a period of time before the channel suddenly snapped and then reformed. When n-dodecane and PCE were used in the experiments, the rivulet snapped before the advancing blob reached the outlet of the fracture, resulting in a discrete blob of liquid that migrated down the remainder of flow path towards the fracture outlet. Intermittent flow also occurred during the rock-replica fracture combination experiment under the same mode observed in the experiments with n-dodecane and PCE. The persistent occurrence of intermittent flow suggests that this is an important feature of flow through unsaturated fractures.

The location and distribution of the preferential flow path was consistent even when different liquids were introduced, but the wettability of the liquid had a significant effect on the rate at which the rivulets snapped and reformed. A strongly wetting liquid will spread on the fracture surface, forming films which remove liquid from the rivulets and increase the rate at which they thin and subsequently snap.

3. Intermittent Flow in Unsaturated, Variable Aperture Fractures

3.1. Introduction

Flow oscillations are an important aspect of multi-phase flow in porous and fractured media. In two-phase flow experiments using etched micromodels, which are designed to represent two-dimensional porous media, the non-wetting fluid snaps off during the imbibition of the wetting fluid (*Lenormand et al.*, 1983). Two-phase flow experiments conducted in horizontal fractures have demonstrated that unsteady flow may occur as a result of the interplay between capillary effects and pressure drop due to viscous flow (*Persoff and Pruess*, 1995). Flow oscillations have also been observed during gravity drainage of water in coarse sands (*Prazák et al.*, 1992) and gravity flow in fractures (*Glass and Nicholl*, 1996). *Kneafsey and Pruess* (1998) observed intermittent rivulet and drop flow in natural and analog fractures under conditions of partial saturation and thermal drive. Pulsating gas-water displacement in fractures has been studied in numerical simulations performed by *Thunvik and Braester* (1990). Unsteady flow under two-phase conditions was observed in the field during the Stripa Validated Drift Experiments in Sweden (*Long et al.*, 1995).

Flow visualization experiments conducted in Chapter 2 indicate that intermittent flow is a persistent feature of flow in unsaturated fractures, where rivulets along the flow channel undergo cycles of snapping and reforming even in the presence of constant boundary conditions. Current analytical and numerical models based on Richards' equation describing water flow in unsaturated fractures do not predict intermittent flow. Efforts to describe the observed oscillatory nature of flow in unsaturated fractures using chaos theory are currently being investigated (*Geller et al.*, 1998; *Pruess et al.*, 1999). Two modes of intermittent flow were observed in the flow visualization experiments conducted in Chapter 2. In one mode, which will be referred to as the pulsating blob mode, a blob of liquid snapped from the flow channel when the gravitational force exceeded the capillary and viscous forces. During this mode, the flow channel never completely connected over the length of the fracture and disconnected blobs of liquid migrated down the flow path and towards the outlet. In a second mode of intermittent flow, referred to as the snapping rivulet mode, the flow channel would remain connected over the length of the

fracture for some time and then rivulets along the flow channel would suddenly snap and reform. A mechanism giving rise to the snapping rivulet mode will be proposed and examined in this chapter using idealized, variable aperture fractures. The frequencies of intermittent flow events during the snapping rivulet mode are measured in laboratory experiments and then related to the capillary and Bond numbers to characterize this flow behavior.

3.2. Conceptual Model for Intermittent Flow

The rivulet snapping mode of intermittent flow occurred during two of the flow visualization experiments conducted in Chapter 2, Experiments 2.1 and 2.2, where water was used as the infiltrating liquid. Intermittent flow was observed to occur along an aperture sequence progressing from small to large to small. An idealized sketch of this aperture sequence is shown in Figure 3.1. Water advances under gravity through the top section until it encounters the capillary barrier at the interface of the top and middle sections which allows the formation of a rivulet through the large aperture section. When the advancing meniscus reaches the bottom section, the strong capillary force provided by the smaller aperture section pulls the rivulet through at a faster rate than the supply of water through the top section, thereby causing it to snap in the middle section. The flow capacity, or permeability of the bottom section must be sufficient to pull the liquid away.

3.3. Experimental Apparatus and Procedures

The conceptual model for intermittent flow was tested in an idealized fracture cell containing the hypothesized aperture sequence. Two series of experiments, denoted as Experiments 3.1 and 3.2, were conducted. Table 3.1 lists the apertures, b, and lengths, L, of the three sections of the plates used in these two experiments. Experiment 3.2 contained a smaller middle aperture than the one used in Experiment 3.1, which was more representative of the aperture values measured in the fracture replica. The apertures in Experiment 3.1 progressed from medium to large to small while Experiment 3.2 contained apertures with a small to large to

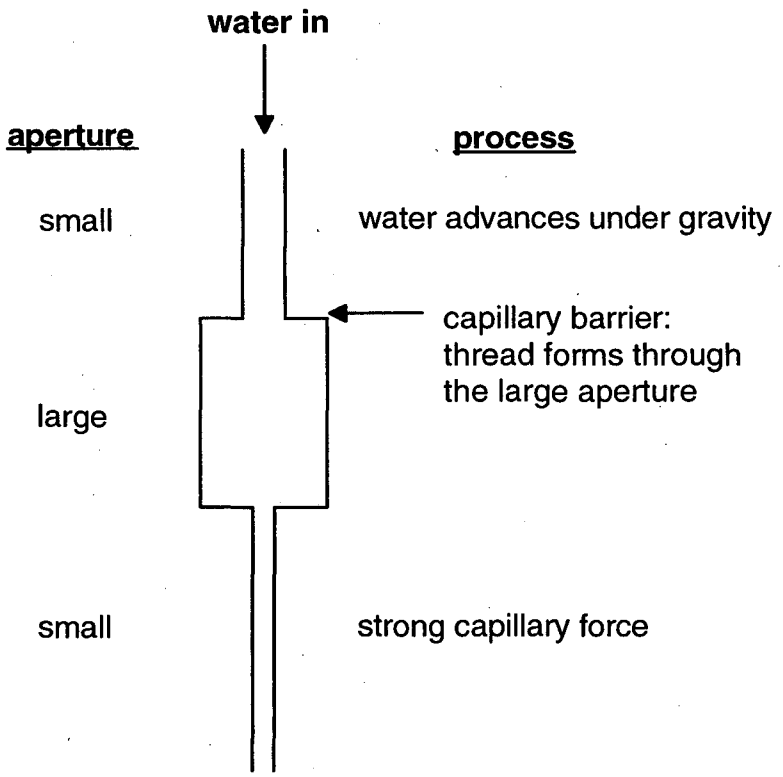

Figure 3.1. Cross-section of the hypothesized aperture sequence giving rise to intermittent flow.

medium sequence. Both configurations were investigated since intermittent flow occurred in the fracture replica along both types of aperture sequences.

The flow cells for Experiments 3.1 and 3.2 were assembled by placing shims of desired aperture between a continuous lower glass plate and three upper glass plates for each section, shown in Figure 3.2. A thin bead of silicone was applied along the outside edges between the adjacent plates to hold the three sections together. The plates were then held between lucite plates and the metal flange used in the flow visualization experiments conducted in Chapter 2. The assembly was then placed over an inclined light table. Water dyed with 0.2% Liquitint by volume was used and the experiments were videotaped for a duration of 30 - 60 minutes at each flow rate. The properties of the dyed water are summarized in Table 3.2.

In Experiment 3.1, water was introduced to the top edge of the plates from a Mariotte bottle. Felt was used as a wicking medium connecting the tube where it contacted the middle third of the plate edge. The Mariotte bottle was placed at an elevation higher than the inlet of the plates and a needle valve was used to control the flow rate to the plates. A flow meter was used to measure the inlet flow rate (Gilmont shielded flowmeter, micro, Cole Parmer, IL). Filter paper (Whatman qualitative filter paper #1, Clifton, NJ) was placed in the lower 6.5 cm of the bottom section to promote drainage of water out of the plates. The sides of the cell were left open to the atmosphere. The cell was initially inclined to 58° from the horizontal and then raised to 70° without reassembling the plates. Three flow rates were applied to the plates at 58° and four flow rates were applied to the plates at 70°. In Experiment 3.2, water was introduced at a constant flow rate to the plates with a syringe pump (Model 33, Harvard Apparatus, South Natick, MA). The ceramic endcap used in the flow visualization experiments conducted in Chapter 2 was placed along the top edge of the plates to deliver water to the flow cell. Water was introduced differently in these experiments to ensure that flow cycling occurred regardless of the method of application. Felt was clamped to the outlet of the cell and the sides of it were left open to the atmosphere. The cell was inclined to 76° and three flow rates were applied to the plates.

Table 3.1. Dimensions of the Glass Plates used in Experiments 3.1 and 3.2

Aperture, b, and length, L	Experiment 3.1	Experiment 3.2
b_1 (mm)	0.25	0.10
b_2 (mm)	0.66	0.35
b_3 (mm)	0.10/filter paper	0.25
L_1 (cm)	7.6	7.3
L_2 (cm)	8.9	8.4
L_3 (cm)	16.5	9.7

1, 2, 3 denote the top, middle, and bottom sections, respectively;
width of each section is 21.6 cm

Table 3.2. Physical Properties of Distilled Water with 0.2% Liquitint by Volume

Surface tension[a,c]	0.0664 N/m
Density[b]	995.6 kg/m^3
Viscosity[b]	1.013 x 10^{-3} kg/(m-s)
Contact angle on glass [a,d]	33°
Contact angle on epoxy[a,d]	63°

[a] measured at T = 20°C
[b] measured at T = 19.7°C
[c] measured with a CSC Du Nouy Tensiometer (CSC Scientific Company, Inc., Fairfax, VA)
[d] measured with a goniometer (Ramé-Hart, Inc., Mountain Lakes, NJ)

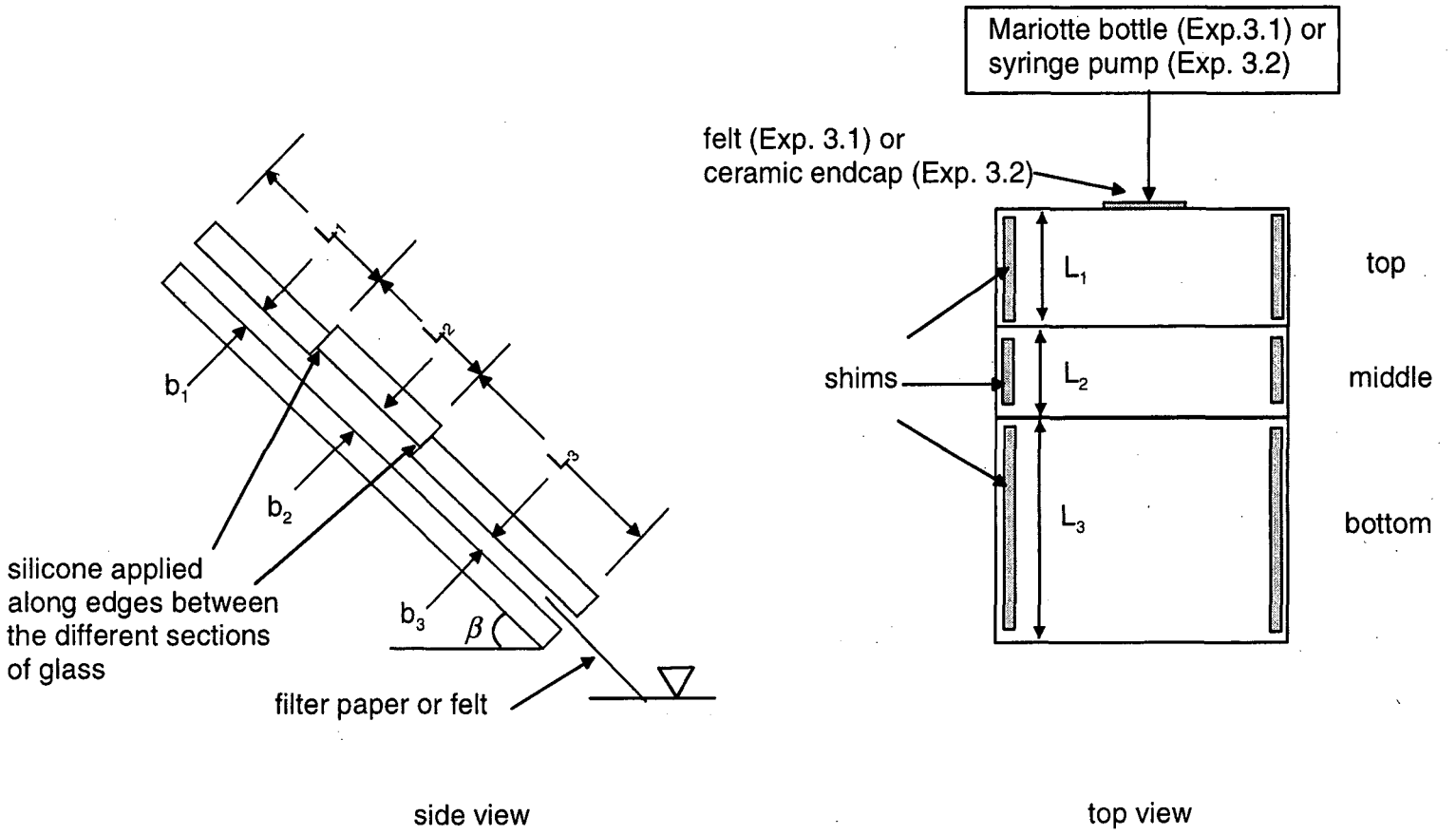

Figure 3.2. Side and top view of the three-aperture fracture cell. The apertures, b, and the lengths, L, of the top, middle, and bottom section are denoted with subscripts 1, 2, and 3, respectively

3.4. Observations of Flow Behavior

Intermittent flow was successfully reproduced in Experiments 3.1 and 3.2 using the small to large to small aperture sequence. At the lowest flow rates, the pulsating blob mode occurred, where the rivulet formed in the middle section and snapped before the advancing blob reached the bottom of the middle section. This mode of intermittent flow was also observed in experiments conducted by *Glass and Nicholl* (1996) and is similar to the phenomenon of the dripping faucet, where a drop of liquid snaps off when the gravitational force overcomes the capillary force. At intermediate flow rates, the rivulet snapping mode occurred, where the rivulet spanned the entire length of the middle section, remained connected for a period of time after the advancing blob drained into the bottom section and then snapped. Finally, at higher flow rates, a steady rivulet formed in the middle section that did not snap. A sequence of images of the two modes of intermittent flow were captured from the videotape during Experiment 3.1 and are shown in Figures 3.3a and b with a 5 second time interval between two subsequent images. A photograph of the steady liquid distribution is shown in Figure 3.3c.

Although the viscosity of the liquid was not varied in these experiments, increasing the viscous force should result in a longer rivulet forming behind the advancing blob before it snaps during the blob snapping mode. Experiments conducted to examine the effect of viscosity on the shape of drops falling from a faucet indicate that as the viscosity increases, a much longer thread of liquid or "neck" forms behind the drop before it breaks off (*Shi et al.*, 1994). During the rivulet snapping mode, the rivulet should remain stable for longer periods of time as the viscous force increases.

The range of flow rates over which the rivulet snapping mode occurred in Experiments 3.1 and 3.2 are summarized in Table 3.3. Below the lowest flow rate in this range, the pulsating blob mode dominated in these experiments. Steady flow occurred at flow rates above the maximum value where the rivulet snapping mode was observed. A higher flow rate was required for the rivulet to become steady when a larger aperture in the middle section was used. The length of the section with the large aperture should also affect the magnitude of the threshold

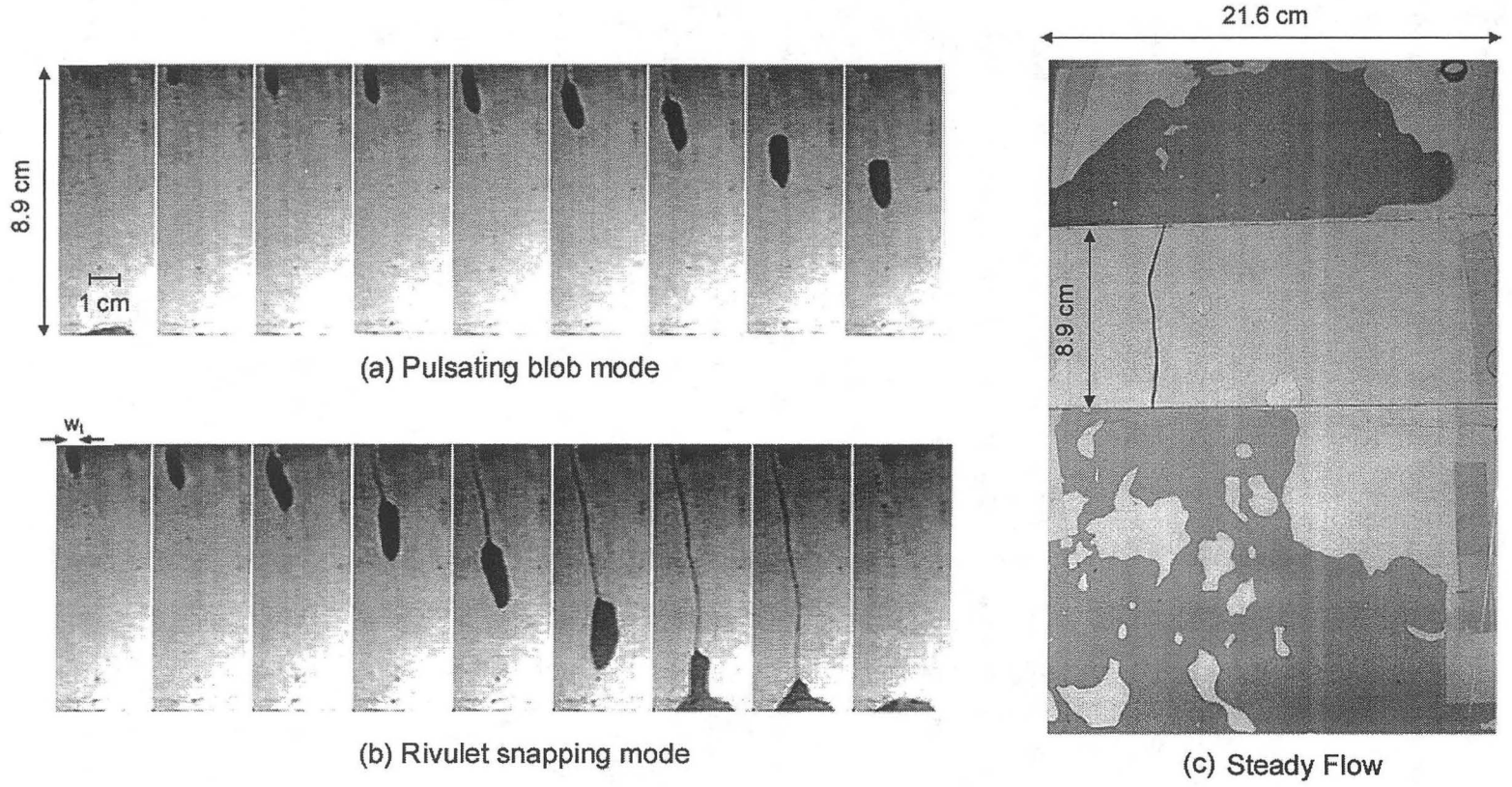

Figure 3.3. Images taken from Experiment 3.1, $\beta = 58°$ of the flow modes observed in the three aperture fracture cell experiments. (a) Pulsating blob mode, Q = 6 ml/hr and (b) snapping rivulet mode, Q = 10.6 ml/hr. Time between subsequent images in (a) and (b) is 5 seconds. (c) Liquid distribution in the three sections when flow becomes steady, Q = 18 ml/hr.

flow rates for the different modes to occur, but this length was kept nearly the same in Experiments 3.1 and 3.2.

The location where the rivulet snapped was constant in Experiment 3.1 and occurred at the top of the middle section. In Experiment 3.2, the rivulet snapped between 1-6 cm below the top of the middle section. A new finger immediately began to form at the point where the rivulet snapped. The formation of the blob and rivulet in these experiments appeared very similar to the observations of intermittent flow during the flow visualization experiments conducted in Chapter 2.

Table 3.3. Approximate Range of Flow rates over which the Rivulet Snapping Mode occurred in Experiments 3.1 and 3.2

Experiment	β	Range of flow rates (ml/hr)
3.1	58	8.5 – 12
3.1	70	8.5 – 24
3.2	76	2 - 5

3.5. Characterization of Intermittent Flow

An intermittent flow event is defined as one cycle of the finger snapping, reforming, and then snapping again. In this section, intermittent flow is characterized by relating the frequency of intermittent flow events to dimensionless numbers expressing the forces controlling this behavior. A similar type of analysis has been performed in studies of snap-off during two-phase flow in capillary tubes and drops from a faucet (e.g. *Gauglitz et al.*, 1988; *Schulkes*, 1994). The frequencies of intermittent flow events are measured from two experiments conducted in Chapter 2 where the rivulet snapping mode occurred, Experiments 2.1 and 2.2, and from the idealized, three-aperture fracture experiments conducted in this chapter, Experiments 3.1 and 3.2.

The frequency of intermittent flow events is a function of gravity, capillary, and viscous forces. The dimensionless numbers expressing the relative magnitude of these forces are the Bond and capillary number. The ratio between gravity and capillary forces is expressed using the Bond number (*Bo*):

$$\text{Bond number} = \frac{\text{gravity force}}{\text{capillary force}} = \frac{\Delta\rho b^2 g \sin\beta}{\sigma\cos\gamma} \tag{3.1}$$

The ratio between viscous and capillary forces is the capillary number (*Ca*):

$$\text{capillary number} = \frac{\text{viscous force}}{\text{capillary force}} = \frac{\mu_l u_l}{\sigma\cos\gamma} \tag{3.2}$$

where $\Delta\rho$ is the density difference between the infiltrating liquid and the air, g is the gravitational acceleration constant, β is the angle of inclination of the fracture measured from the horizontal, b is the aperture, σ is the liquid surface tension, μ_l is the viscosity of the liquid, u_l is the velocity of the liquid, and γ is the contact angle of the wetting phase on the solid surface. The contact angle of water on the epoxy fracture replica used in Experiments 2.1 and 2.2 is approximately 63° and 33° on the glass plates used in the Experiments 3.1 and 3.2. The Bond and capillary numbers are also used in studies of entrapment of oil and non-aqueous phase liquids in porous media, where the saturation of the non-wetting phase is correlated to the Bond and capillary number (e.g. *Morrow and Songkran*, 1981; *Zhou and Orr*, 1995; *Dawson and Roberts*, 1997).

The frequency of intermittent flow events measured from the experiments were non-dimensionalized (denoted as f^*) with the following relationship:

$$f^* = \frac{fb^3}{Q} \tag{3.3}$$

where f is the average frequency of intermittent flow events.

In our experiments, the apertures corresponding to the location where the rivulet snapped (b_i) were used to calculate the Bond number and f^*. In Experiments 2.1 and 2.2, b_i was estimated by locating the point where the rivulet snapped on the aperture map of the fracture replica measured in Chapter 2. In Experiments 3.1 and 3.2, b_i corresponded to the aperture of the middle section. The error in measuring b_i was approximately $\pm$ 0.1 mm for the fracture replica experiments due to the uncertainty in the aperture measurements. For the three-aperture fracture cell experiments, the error in b_i was $\pm$ 0.02 mm, the resolution of the caliper used to measure the shims. The finger velocities used to tabulate the capillary number are discussed in the next section.

3.5.1. Finger Velocities

Measurements of the finger velocity were made from the videotaped images. In this investigation, a finger was defined as the rivulet connected to the advancing blob of water. Plots of the distance of the advancing air-water meniscus as a function of time as the finger advances in Experiment 2.1 are presented in Figure 3.4 for one cycle of an intermittent flow event at each angle. This distance was measured from the top of the fracture to the tip of the advancing meniscus. At all three angles of inclination, a gradual increase in the distance traveled for the first 100-140 seconds is followed by a rapid increase in the distance traveled for the next 10 seconds. The velocity of the advancing meniscus changes to a faster rate after the finger drains and forms a rivulet behind the advancing blob.

For the particular cycles shown in Figure 3.4, the velocities increase as the angle of inclination increases before the rivulet forms, but the velocities after the rivulet forms are smaller at the two higher angles than at the lowest angle. When an additional cycle was analyzed for each angle, the velocity of the finger after the rivulet formed increased as the angle of inclination increased. The velocities of the finger before the rivulet formed were consistent over the two cycles, however, and are presented in Table 3.4. The inconsistencies in the finger velocities after the rivulet formed may be due to varying amounts of residual water left by the previous finger.

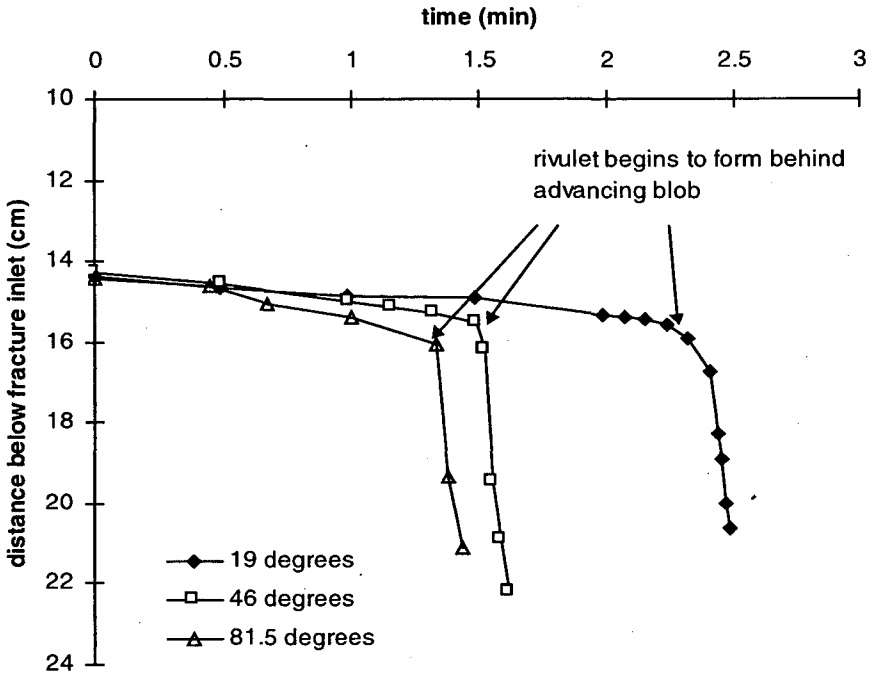

Figure 3.4. Rate of finger advancement in Experiment 2.1 for the three angles of inclination. Finger accelerates to a faster rate of advancement after the rivulet forms behind the advancing blob.

Table 3.4. Summary of intermittent flow parameters from Experiments 2.1, 2.2, 3.1, and 3.2

Exp.	β	*Inlet Pressure* (cm of H_2O)	Q (ml/hr)	*Velocity of Finger*, u_l (cm/min)		f (min^{-1})	b_i (mm)	*Ca* ($x10^5$)		*Bo*	f^*
				before rivulet forms	after rivulet forms			before rivulet forms	after rivulet forms		
	19	-2.3	2.0	0.5	43	0.34	0.20	0.3	24	0.004	8.1×10^{-5}
2.1	46[a]	-2.2	2.0	0.8	43	0.29	0.20	0.5	24	0.009	7.0×10^{-5}
	81.5	-1.9	2.0	1.1	47	0.36	0.20	0.6	26	0.013	8.6×10^{-5}
		-3.5	1.3	0.4	6.6	0.13	0.30	0.2	3.6	0.027	1.6×10^{-4}
2.2[b]	70	-2.5	1.4	1.0	7.6	0.16	0.30	0.5	4.1	0.027	1.8×10^{-4}
		-1.5	2.1	0.9	8.6	0.30	0.30	0.5	4.7	0.027	2.4×10^{-4}
		-1.0	2.4	1.2	16	0.25	0.30	0.7	8.6	0.027	1.7×10^{-4}
		NA	8.8	3.4	18	0.39	0.60	1.0	5.4	0.053	1.1×10^{-3}
3.1	58	*NA*	10.6	3.7	30	0.66	0.60	1.1	9.1	0.053	8.1×10^{-4}
		NA	11.8	5.8	37	0.69	0.60	1.8	11	0.053	7.6×10^{-4}
		NA	8.6	5.3	35	1.40	0.60	1.6	11	0.059	2.1×10^{-3}
3.1	70	*NA*	10.1	5.3	39	1.38	0.60	1.6	12	0.059	1.8×10^{-3}
		NA	14.5	5.8	48	1.08	0.60	1.8	15	0.059	9.7×10^{-4}
		NA	23.7	7.7	48	0.89	0.60	2.3	15	0.059	4.9×10^{-4}
		NA	2.0	1.2	*NA*	0.30	0.35	0.4	*NA*	0.021	4.0×10^{-4}
3.2[c]	76	*NA*	4.0	1.5	*NA*	0.49	0.35	0.5	*NA*	0.021	3.2×10^{-4}
		NA	5.0	2.8	*NA*	0.70	0.35	0.9	*NA*	0.021	3.6×10^{-4}

[a]fracture was reassembled between 19° and 46° in Experiment 2.1

[b]flow proceeded along two channels from -2.5 to -1.0 cm H2O; f^* calculated using half of measured flow rate

[c]increase in the rate of finger advancement did not occur in Experiment 3.2

NA: Not available

We observed that the finger had a larger velocity when it encountered residual water along the flow path. Because of the discrepancies in the velocities after the rivulet forms in Experiment 2.1, velocities were measured and averaged over three cycles and are summarized in Table 3.4. In Experiment 2.2, flow proceeded along two flow channels, except at the lowest pressure head applied (-3.5 cm) where flow proceeded only along the right channel. The velocities of the left and right channels were measured and averaged to obtain the velocities before and after the rivulet formed, which are summarized in Table 3.4. We assumed that each flow channel took approximately half of the total volumetric flux measured.

Figures 3.5a-c are plots of the distance traveled by the advancing meniscus as a function of time for one cycle of the finger entering the middle section in Experiments 3.1 and 3.2. The distance was measured from the top of the middle section to the tip of the advancing meniscus. One cycle at each flow rate and angle of inclination of rivulet formation to snapping, representative of the average frequency of events, was selected for analysis. The trend in Figures 3.5a and b is similar to the result from the fracture replica experiment shown in Figure 3.4, where there is a gradual increase in the distance traveled with time, followed by a rapid acceleration to a faster rate of advancement. When the advancing meniscus reaches a distance of approximately 2 cm in Experiment 3.1, a distinct change in the slope occurs in the plots corresponding to when drainage behind the advancing blob occurred. The width of the finger measured at the top of the middle section (w_f), defined in Figure 3.3a, is plotted in Figure 3.5d as a function of the distance of the advancing meniscus below the middle section. Plots of only two flow rates, one at each angle from Experiment 3.1, are shown in this figure since the plots are very similar regardless of the flow rate or angle of inclination. The fingers in Experiment 3.2 generally left a portion of the trailing rivulet a few centimeters below the top of the middle section after snapping. A change in the rate of advancement did not occur with these fingers (Figure 3.5c) since not enough room was left in the middle section for the blob to accumulate to the critical length which would result in a faster rate of finger advancement.

The velocities of the fingers before and after the rivulet forms were calculated from the slopes of the plots in Figure 3.5 and are presented in Table 3.4. A second cycle was also

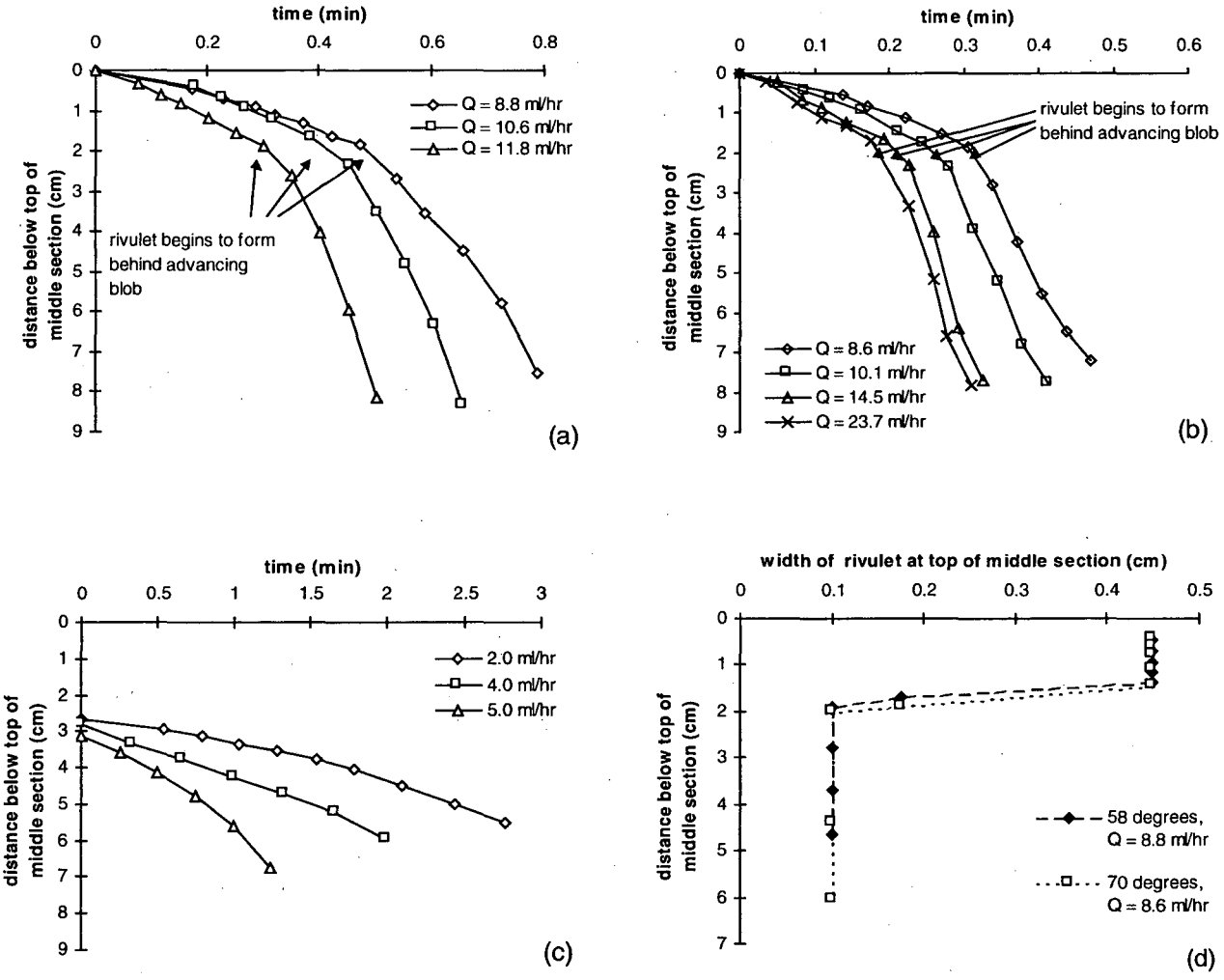

Figure 3.5. (a)-(b) Rate of finger advancement during Experiment 3.1 at $\beta = 58°$ and 70°, respectively. (c) Rate of finger advancement during Experiment 3.2. (d) Change in width of the finger measured at the top of the middle section.

measured for comparison, and the velocity measurements were consistent in both cycles. The velocity of the finger generally increases with applied flow rate at a given angle of inclination and at higher angles of inclination for a given flow rate. The capillary numbers were calculated using the velocities obtained both before and after the rivulet formed in these experiments since they correspond to distinct stages of the finger advancement during the rivulet snapping mode.

3.5.2. Frequency of Intermittent Flow Events

The time interval between intermittent flow events was noted from inspection of the video recordings from Experiments 2.1, 2.2, 3.1 and 3.2 to determine whether or not this behavior was periodic. A plot of the cumulative number of intermittent flow events versus time from Experiment 2.1 is presented in Figure 3.6. The number of events grows nearly linearly with time in this plot, indicating periodic behavior. Plots of the cumulative number of events versus time for the remaining experiments are also approximately linear (*Geller et al.*, 1996; *Geller et al.*, 1997). The slopes of these lines provided a quantitative measure of the average frequencies of intermittent flow events (f), which are summarized in Table 3.4. The frequencies were determined based on measurements taken over 30 to 60 minute periods.

The effect of varying the relative strength of the gravity force on the frequency of intermittent flow events can be examined from the results of Experiments 2.1 and 3.1. Intuitively, increasing the relative strength of gravity should make the rivulet less stable and consequently increase the frequency of events. In Experiment 2.1, the frequency decreased slightly from 19° to 46°, which may have been theresult of the fracture being reassembled between these experiments and slightly altering the aperture distribution and the loading of the fracture. When the fracture was raised in Experiment 2.1 from 46° to 81.5° without reassembling it, the frequency increased slightly, which was consistent with the experiment conducted by *Geller at al.* (1996). In Experiment 3.1, the frequency also increased at higher angles of inclination for a given flow rate.

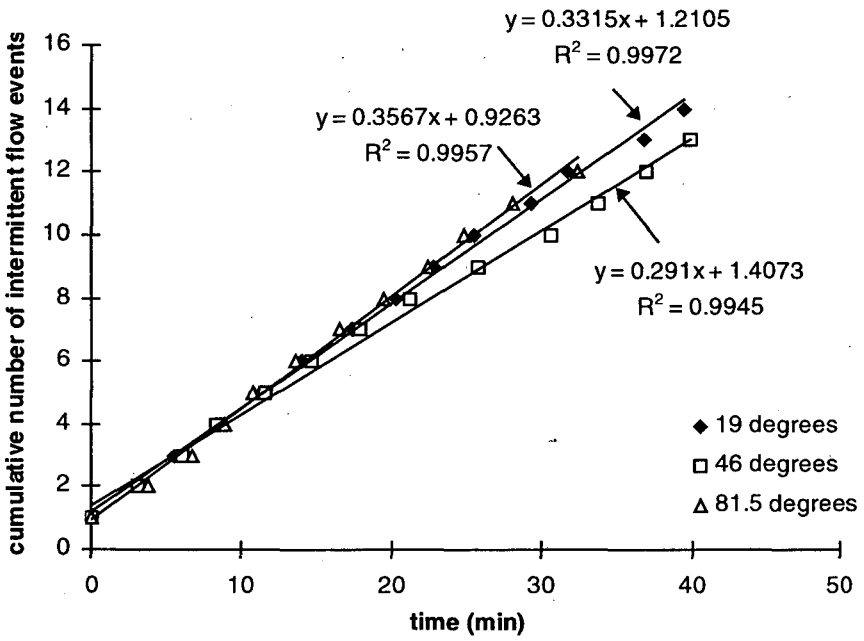

Figure 3.6. Cumulative number of intermittent flow events as a function of time for Experiment 2.1. The number of intermittent events grows linearly with time indicating periodic behavior. Average frequencies of these events are obtained from the slopes of these lines.

The frequencies of events were non-dimensionalized with Equation 3.3 and these values are summarized in Table 3.4. The dimensionless frequencies of events do not have a consistent trend as a function of the capillary or Bond number. The data was therefore examined as a function of the ratio of the capillary to Bond number squared (Ca/Bo^2) and a plot of this data is presented in Figure 3.7. This ratio was chosen since the capillary, viscous, and gravity forces are all represented in Ca/Bo^2. In Figure 3.7a, the values of Ca/Bo^2 were calculated using the finger velocities before the rivulet formed, while in Figure 3.7b, they were calculated using the finger velocities after the rivulet had formed. The data from Experiment 3.2 are not included in Figure 3.7b since the finger did not accelerate to a faster rate of advancement in that experiment. The data have a consistent trend in both plots, where the dimensionless frequencies decrease with increasing Ca/Bo^2. The trend of the data is consistent with expectations since higher values of Ca/Bo^2 indicate that the relative strength of gravity has decreased and/or the viscous and capillary forces have increased, which should stabilize the rivulet and lower the frequency of events.

The values of Ca/Bo^2 where flow transitioned from one mode to another can be obtained from Experiments 3.1 and 3.2. In Experiment 3.1, the transition from the pulsating blob to rivulet snapping mode occurred at a Ca/Bo^2 of approximately 0.025 and the transition from the rivulet snapping to steady flow occurred at Ca/Bo^2 equal to 0.04. In Experiment 3.2, the critical values of Ca/Bo^2 for these transition points were 0.008 and 0.02. More data is needed to determine whether a consistent range of values for these transition points can be obtained. For a given liquid, the degree of fracture roughness will be an important factor affecting when the flow changes into the different modes. In relatively smooth fractures, the pulsating blob mode is more likely to occur than the rivulet snapping mode since regions of small to large to small apertures, which are necessary for the rivulet snapping mode to occur, will not be as common in smoother fractures. Therefore, in smoother fractures, the pulsating blob mode will probably transition directly to steady flow as the flow rate increases, whereas in rougher fractures, flow will probably change from the pulsating blob mode to the rivulet snapping mode and finally to steady flow as the flow rate increases.

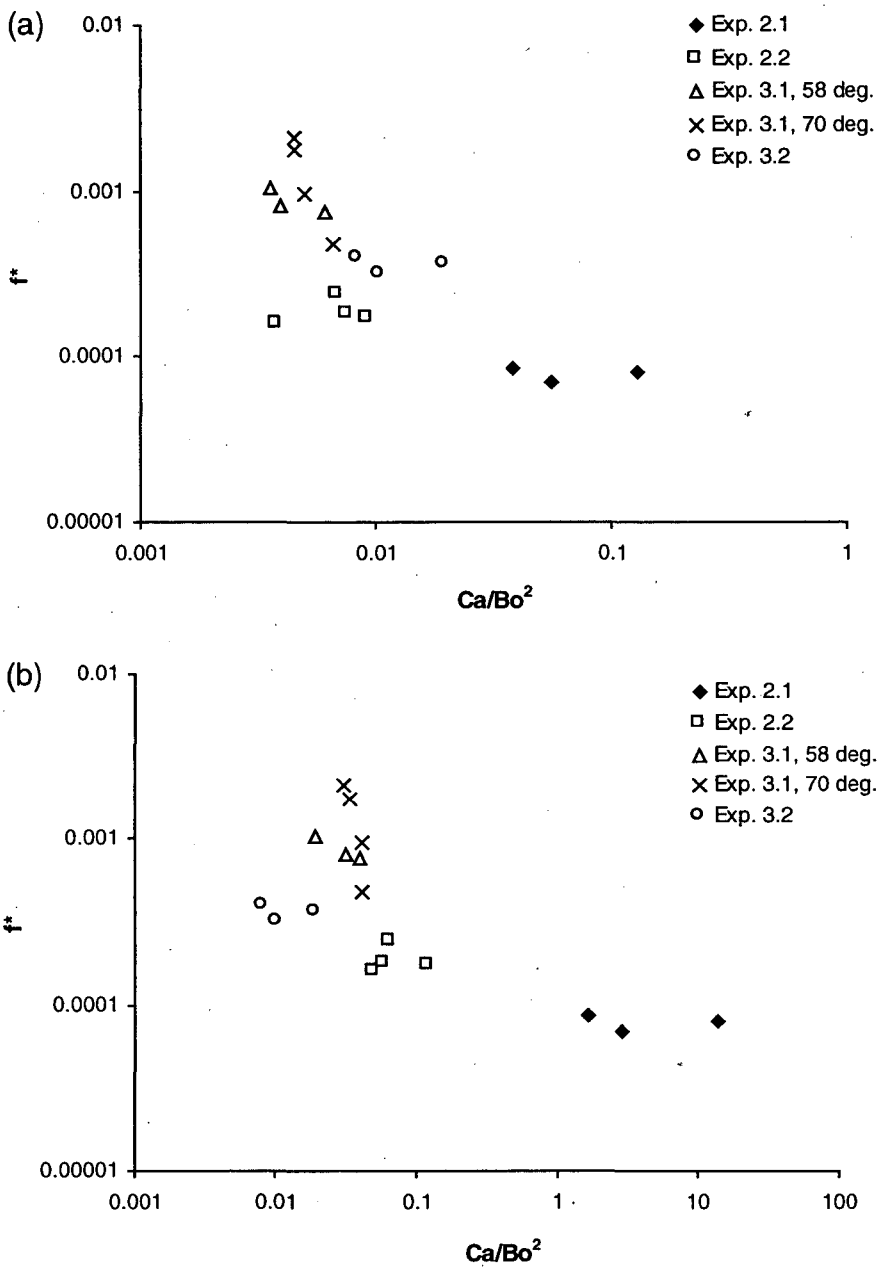

Figure 3.7. Plot of dimensionless frequency of events as a function of Ca/Bo^2 calculated using the (a) velocities before the rivulet formed and (b) velocities after the rivulet formed.

3.6. Summary and Conclusions

The cyclic formation and snapping of rivulets observed in a replica of a natural fracture is due to the interplay of capillary, viscous, and gravity forces and the geometry of the apertures along the flow path. A conceptual model for intermittent flow was proposed and then tested using an idealized fracture with a small to large to small aperture sequence (three-aperture fracture cell). Two modes of intermittent flow were observed as a function of flow rate in the idealized fracture. At the lowest flow rates, the pulsating blob mode occurred, where the rivulet snapped before the advancing blob of water reached the bottom, smaller aperture. At intermediate flow rates, the rivulet snapping mode occurred, where the rivulet remained connected for a period of time upon reaching the bottom aperture, and then snapped and reformed. At the highest flow rates, the rivulet remained steady. The rivulet snapping mode was similar to the mode of intermittent flow observed in the water seepage experiments conducted on the fracture replica in Chapter 2. The frequencies of intermittent flow events for this mode of intermittent flow were measured from experiments conducted in the fracture replica and the idealized, three-aperture fracture. The frequencies of events were non-dimensionalized and then related to the Bond and capillary numbers to generalize the results. The dimensionless frequency had a consistent trend as a function of Ca/Bo^2, where the dimensionless frequencies decreased with increasing Ca/Bo^2.

4. Characteristic Flow Features in Unsaturated Fractures

4.1. Introduction

Laboratory and field experiments have provided considerable evidence that flow through unsaturated fractures proceeds as fingers or preferential flow paths (*Scanlon*, 1992; *Nicholl et al.*, 1994; *Nativ et al.*, 1995; *Su et al.*, 1999). Fingering is the focusing of flow into narrow channels with seepage velocities dramatically increased compared to spatially uniform flow (*Pruess*, 1998). Predictions of contaminant migration require an accurate representation of actual fluid velocities, particularly within the unsaturated zone.

Visualization experiments have demonstrated the importance of gravity on the flow observed during unsaturated flow in fractures and porous media (*Nicholl et al.*, 1994; *Glass and Nicholl*, 1996; *Su et al.*, 1999). Wetting fronts entering non-horizontal fractures can be much different than wetting fronts entering horizontal fractures due to gravitational effects. During the initial invasion of liquid into dry, inclined fractures, fingers often consist of a wider portion of liquid at the advancing front, defined as a blob in this study, that are connected to a narrow thread or rivulet of liquid. These features have not been observed in horizontal fractures. Gravity also gives rise to flow oscillations in unsaturated fractures, where rivulets along the flow channel undergo cycles of snapping and reforming (*Su et al.*, 1999). Flow oscillations have also been observed during two-phase flow in horizontal fractures and etched micromodels (*Lenormand et al.*, 1983; *Persoff and Pruess*, 1995; *Keller et al.*, 1997). Snap-off of the non-wetting phase occurs in horizontal systems whereas the wetting phase undergoes intermittent flow in inclined, unsaturated fractures.

Wettability affects the size of the advancing blob during the initial invasion and the frequency at which intermittent flow occurs in unsaturated fractures. For strongly wetting liquids, the advancing blob was much smaller and the flow channels underwent much more frequent cycles of snapping and reforming compared to an intermediate wetting liquid (*Geller et al.*, in press).

Blob migration and rivulet flow in unsaturated fractures have not been examined quantitatively in previous studies. These flow features are not predicted by current analytical and numerical models of flow in unsaturated fracture and may have significant effects on seepage rates and transport predictions. In this chapter, theoretical aspects of finger drainage, blob migration, and rivulet flow are discussed and compared with observations from laboratory experiments conducted on idealized fractures with controlled apertures. The effect of wettability and surface roughness on the rate of blob advancement is quantified by calculating the contact angle hysteresis associated with each surface. The effects of wettability and aperture variability on rivulet flow are also examined in this chapter.

4.2. Background

4.2.1. Wettability

Wettability describes the tendency of a fluid to spread along a solid surface in the presence of another immiscible fluid (*Crocker and Marchin*, 1988). Natural mineral surfaces are generally assumed to be strongly water-wetting, but natural hydrophobic organic materials on the mineral surface can alter the wettability of surfaces (*Bradford and Leij*, 1995). Petroleum reservoir rocks have long been recognized to have fractional wettabililty, where portions of the pore surface area are preferentially oil-wet or water-wet (*Dullien*, 1992). *Powers et al.* (1996) found a wide range of wetting conditions for sands that had been exposed to different organic liquid contaminants. Wettability is often quantified through contact angle measurements. The contact angle of water on clean sand and glass is generally close to zero. However, relatively large contact angles have been measured even for nominally clean natural mineral surfaces. *Selker et al.* (1998) measured contact angles as high as 58° for water on grains of sand and *Geller et al.* (1996) measured contact angles of approximately 60° for water on a smoothed piece of granite.

In homogeneous materials, contact angle hysteresis, manifested by the difference in the receding and advancing contact angles, is affected by surface roughness and contamination

(*Dullien*, 1992). The advancing contact angle is always larger than the receding one. For water on glass beads, *Laroussi and DeBacker* (1979) obtained an advancing angle of 66° and a receding angle of 46°. *Bradford and Leij* (1995) measured an advancing angle of 32.7° and a receding angle of 0° for water on silica sand. For an intermediate wetting surface, the advancing contact angle may become greater than 90° while the receding contact angle remains less than 90°. The advancing and receding contact angles are dependent on the velocity. The advancing contact angle increases with increasing velocity while the receding contact angle decreases with increasing velocity (*Adler and Brenner*, 1988). The radius of curvature at the advancing air-water interface also becomes larger as the gravity force increases (*Iwata et al.*, 1995).

4.2.2. Finger Drainage

Formation of a narrow thread of liquid or rivulet behind an advancing blob under continuous liquid application in unsaturated fractures has been observed by *Nicholl et al.* (1993) and *Su et al.* (1999). In their experiments, they defined the narrow region of liquid behind the advancing blob as a desaturated region. In coarse soils, a drained or desaturated region behind a nearly saturated advancing fingertip has also been observed and measured, but the desaturated region remains the same width as the fingertip (e.g. *Glass et al.*, 1989; *Selker et al.*, 1992).

The hypothesis for finger drainage was originally proposed by *Raats* (1973). If the finger is viewed as a hanging column of liquid, the pressure head at the top of the finger decreases as the finger lengthens. When the pressure at the top of the finger falls below the air entry pressure, the finger begins to drain or desaturate. Finger drainage has been observed qualitatively in flow visualization experiments conducted in sands and fractures (*Glass et al.*, 1989; *Glass and Nicholl*, 1996). *Selker et al.* (1992) quantitatively verified the hypothesis for finger drainage in experiments conducted on homogeneous, coarse sand. If the rate at which liquid is supplied to the finger is slow, the critical length for drainage, L_{crit}, is simply a balance of gravity and pressure forces:

$$h_{bot} = L_{crit} \sin\beta + h_{top} \tag{4.1}$$

where h_{bot} is the pressure head at the bottom of the finger and h_{top} is the pressure head at the top of the finger and is equal to the air entry pressure head. In a homogeneous fracture modeled as parallel plates, these pressures are defined as:

$$h_{bot} = -\frac{2\sigma \cos \gamma_a}{\rho g b} \tag{4.2}$$

$$h_{top} = -\frac{2\sigma \cos \gamma_r}{\rho g b} \tag{4.3}$$

where b is the aperture width between two parallel plates, σ is the surface tension, μ is the viscosity of the liquid, ρ is the density of the liquid, g is the gravitational acceleration constant, γ_a is the advancing contact angle, and γ_r is the receding contact angle. Substituting Equations 4.2 and 4.3 into Equation 4.1 and solving for L_{crit}, we obtain:

$$L_{crit} = \frac{2\sigma(\cos \gamma_r - \cos \gamma_a)}{\rho g b \sin \beta} \tag{4.4}$$

The blob that forms after finger drainage in fractures generally has a parallel-sided shape. Liquid drops on an inclined plane have also been observed to have similar shapes (*Bikerman*, 1950). A balance of the gravitational and surface tension forces of a drop on an inclined plane is (*Furmidge*, 1962):

$$(\rho V g \sin\beta)/W = S\sigma(\cos \gamma_r - \cos \gamma_a) \tag{4.5}$$

where S is the shape factor for the drop, and W and V are the width and volume of the drop, respectively. In parallel plates, the volume of the blob is approximately equal to bWL. When this value is substituted into Equation 4.5, the equation becomes the same as Equation 4.4, except for the shape factor. In the case of parallel plates, $S = 2$, which corresponds to the value of the shape

factor for parallel-sided drops on a single plane (*Extrand and Kumagai*, 1995), which is similar to the shape of the blob that forms in fractures. The shape of the blob will be affected by differences in wettability and heterogeneities in natural rock fractures, although the blob during the initial invasion into an epoxy replica of a natural fracture also had a similar parallel-sided shape (*Su et al.*, 1999).

4.2.3. Blob Migration

A cross-section of a blob of liquid advancing down an inclined parallel plate is shown in Figure 4.1. Assuming that the motion of the blob is controlled only by the gravitational force and the difference in capillary pressures at the bottom and top of the blob, the velocity of the blob can be described using Darcy's Law written in the following form:

$$u_b = -K_s\left[\frac{h_{b,bot} - h_{b,top}}{L_b} - \sin\beta\right] \tag{4.6}$$

where u_b is the blob velocity, K_s is the saturated hydraulic conductivity, L_b is the length of the blob, and β is the angle of inclination. The pressure heads at the bottom and top of the blob, $h_{b,bot}$ and $h_{b,top}$, are given by Equations 4.2 and 4.3, respectively. *Nicholl et al.* (1994) used an equation similar to Equation 4.6 to analyze the velocities of disconnected fingers as a function of the length of the fingers in obscure glass plate fractures. The saturated hydraulic conductivity in parallel plates is given by:

$$K_s = \frac{\rho g b^2}{12\mu} \tag{4.7}$$

Substituting Equations 4.2 and 4.3 into Equation 4.6, the expression for the blob velocity becomes:

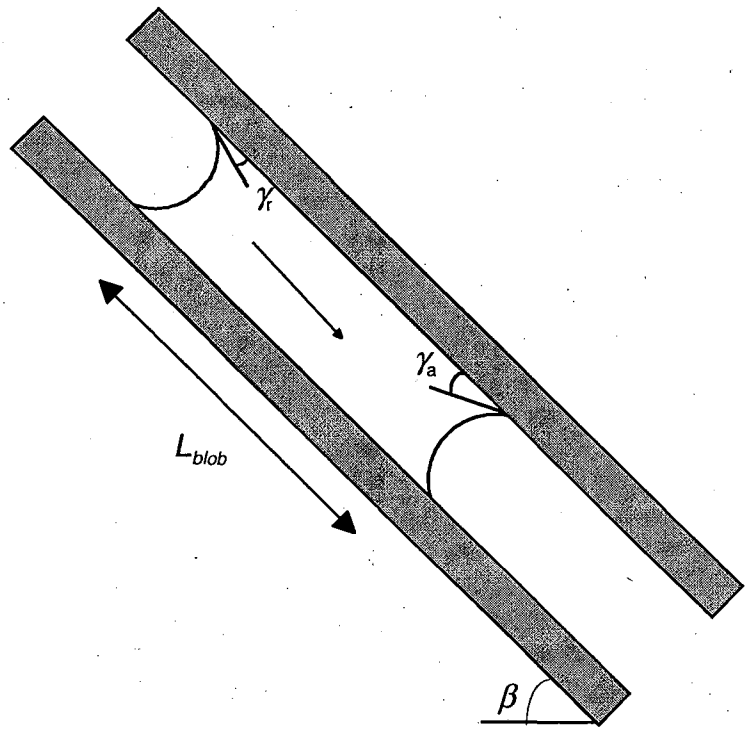

Figure 4.1. Cross-section of a blob migrating down an inclined parallel plate fracture.

$$u_b = -K_s\left[\frac{2\sigma(\cos\gamma_r - \cos\gamma_a)}{L_b\rho g b} - \sin\beta\right] \tag{4.8}$$

The difference in the cosines of the receding and advancing contact angles quantifies contact angle hysteresis, which is given by the following expression after rearranging Equation 4.8:

$$\cos\gamma_r - \cos\gamma_a = \frac{L_b\rho g b}{2\sigma}\left[\sin\beta - \frac{u}{K_s}\right] \tag{4.9}$$

The effect of contact angle hysteresis on the rate of blob advancement will be examined later in the chapter using experimental data.

4.2.4. Rivulet Flow

Rivulets are another important feature of flow in unsaturated fractures. Rivulets affect contaminant transport since they contact a small rock surface area, reducing the potential for fracture-matrix interaction, and can transport contaminants quickly over considerable depths. During intermittent flow, the rivulets become unstable and undergo cycles of snapping and reforming. Assuming that the liquid in the rivulet spans the aperture, the velocity through a stable rivulet should be approximately equal to the saturated flow velocity. In parallel plates, the rivulet width (w_r) can be predicted using the cubic equation for saturated fractures (*deMarsily*, 1986), provided that $w_r >> b$:

$$w_r = \frac{12Q\mu}{b^3\rho g} \tag{4.10}$$

where Q is the applied flow rate. During unsaturated flow, the curvature of the air-liquid meniscus will affect the rivulet width, but this is not accounted for in Equation 4.10. A cross-section of a rivulet on a strongly wetting and intermediate wetting surface is illustrated in Figure

4.2. A portion of the flow will enter the "corner regions" of the rivulet, as indicated in Figure 4.2, which should result in a reduction of the measured rivulet width from the predicted width. For a given flow rate, the rivulet will also be narrower on the strongly wetting surface compared to the intermediate wetting surface because a larger portion of the flow will enter the corner regions on the strongly wetting surface due to the smaller contact angle. Intermittent flow is more likely to occur when a liquid strongly wets a surface since a thinner rivulet is less stable. The frequencies of intermittent flow events measured in experiments conducted on an epoxy fracture replica were up to five times greater for a strongly wetting liquid than for an intermediate wetting liquid (*Geller et al.*, in press).

The assumption that the liquid in rivulet completely spans the aperture width may no longer occur when the aperture becomes large, resulting in the formation of streamlets, which are rivulets that have one contact and one free surface. The instability criterion derived by *Philip* (1975) to predict the onset of fingering in a heterogeneous porous medium will be used in this study to predict the location where the streamlets begin in a fracture with apertures increasing linearly from the top to bottom (wedge fracture). *White et al.* (1977) studied fingering instability in a wedge fracture and accurately predicted the location where fingering began using the criterion derived by *Philip* (1975). In the experiments performed by *White et al.* (1977), the liquid was distributed uniformly over the width of the plates and the advancing front broke up into multiple fingers at the critical distance. In the experimental results that will be presented in this chapter, the liquid will be supplied to a wedge fracture as a point source so that only a single finger forms. Therefore, the advancing front will be too narrow to break up into multiple fingers, but we expect streamlets to form instead at the distance where fingering is predicted to occur.

The criterion for the instability is that the pressure gradient behind the wetting front opposes flow. The general expression for the pressure gradient (G) in a heterogeneous fracture derived by *Philip* (1975) using Darcy's Law, is:

$$G = \frac{h_f - h_o - z_d \sin\beta}{K(z_d)\int_0^{z_d} K^{-1} dz} + \sin\beta \qquad (4.11)$$

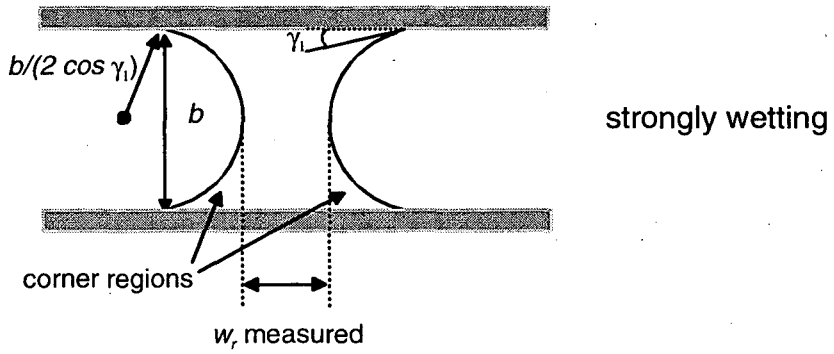

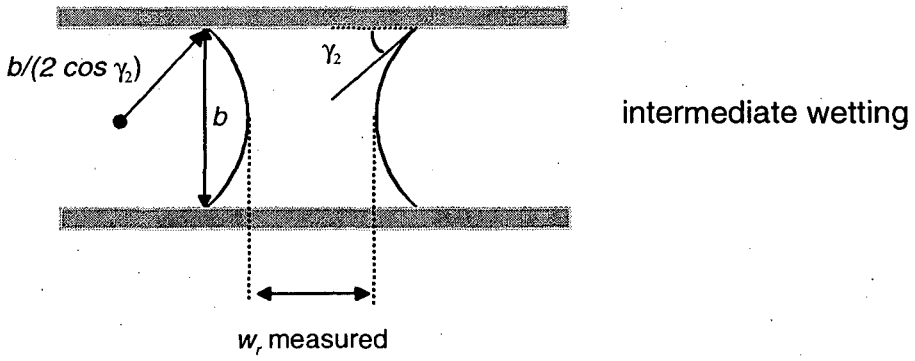

Figure 4.2. Cross-section of a rivulet on a strongly wetting and intermediate wetting surface.

where K is the hydraulic conductivity and z_d is the distance along the flow path. When $G = 0$, the pressure gradient is zero and gravity is just balanced by capillarity. For a wedge geometry, h_f is given by:

$$h_f = -\frac{2\sigma}{\rho g b_o (1 + z_d / d)} \cos\gamma \tag{4.12}$$

where d is a constant that is determined by the slope of the wedge fracture and b_o is the aperture width at the top of the fracture. The hydraulic conductivity as a function of depth in a wedge fracture is:

$$K = c(1 + z/d)^2 \tag{4.13}$$

where c is a constant. Substituting Equation 4.13 into 4.11 and integrating the denominator, we obtain:

$$G = \frac{h_f - h_o - z_d \sin\beta}{\left(1 + \frac{z_d}{d}\right)^2 \left(\frac{-d}{1 + z_d/d} + d\right)} + \sin\beta \tag{4.14}$$

Simplifying the expression in Equation 4.14, G becomes:

$$G = \frac{h_f - h_o - z_d \sin\beta}{\left(\frac{z_d d + z_d^2}{d}\right)} + \sin\beta = \frac{d(h_f - h_o) + z_d^2 \sin\beta}{z_d (d + z_d)} \tag{4.15}$$

Setting $G = 0$ in Equation 4.15 and substituting Equation 4.12 for h_f results in the following expression which has to be solved iteratively for the critical value of z_d:

$$z_{d,crit} = \left[\frac{d(h_o + 2\sigma \cos\gamma)}{b_0 \rho g \sin\beta (1 + z_{d,crit}/d)} \right]^{1/2} \quad (4.16)$$

4.3. Experimental Procedures

4.3.1. Methods

Parallel plate fractures and a wedge fracture were used in this investigation to maintain control of the aperture widths. Three series of experiments were conducted and the experimental conditions of each series are presented in Table 4.1 and a schematic of the experimental set-up is shown in Figure 4.3. The fractures were assembled using 1/4 inch thick flat plate glass, 3/16 inch thick obscure plate glass (both from UC Glass Company Inc., Berkeley, CA) or 1/4 inch thick acrylic plates (Polycast Technology Corp., Stamford, CT). Acrylic was used to represent a fracture surface that had been altered by organic substances, while glass is used as an analog for a "clean" natural fracture surface. Except for the obscure-flat glass plate combination, the aperture widths for the fractures indicate the size of the shims placed between two plates. A capillary rise measurement determined the aperture width for the obscure-flat plate combination. Before each experiment, the plates were washed with distilled, de-ionized water. Excess water was wiped off and then the plates were allowed to air dry. The flow cells had dimensions of 20 x 33 cm and were loaded in a metal frame with six confining bolts. The flow cell was then mounted over an inclined light table. The properties of the liquids used in the three series of experiments are summarized in Table 4.2. Observations were videotaped using a video camera (JVC KY-F55BU with motorized zoom lens JVC TY-10x6 MDPU) and recorded on a video recorder (Sony SVHS SVO-5800) with a time resolution of 1/30 s. Measurements from captured images were made using Adobe Photoshop®.

The first series of experiments were conducted to examine the effect of wettability and surface roughness on finger advancement and drainage. Four fractures were assembled for these

Table 4.1. Summary of Experimental Conditions

Experiment	Plates	β (deg)	b (mm)	Liquid	Q (ml/hr)
Series 1: Finger advancement and drainage	Glass	85	0.15	Dyed water	5
		20, 85	0.25	Dyed water	5
	Acrylic	20, 85	0.25	Dyed water	5
	Obscure glass	20, 85	0.13 – 0.20	Dyed water	5
	Sand-blasted glass	15	*NA*	Water without dye	2
Series 2: Blob velocity	Acrylic	85	0.25	Dyed water	Injected manually with syringe
	Acrylic	20, 85	0.25	n-Dodecane	Injected manually with syringe
Series 3: Rivulet flow	Glass	20	0.25	Dyed water	5, 9.5, 27, 55
	Acrylic	20	0.25	Dyed water	5, 9.5, 27, 55
	Glass	85	0.08 (top) – 1.58 (bottom)	Dyed water	5, 15, 20, 25

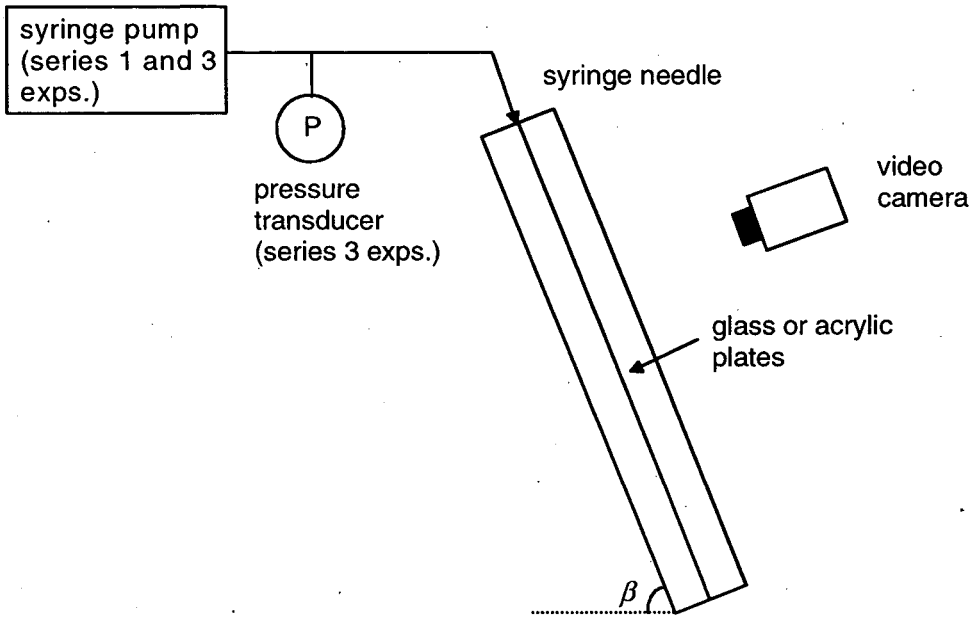

Figure 4.3. Schematic of experimental apparatus.

Table 4.2. Liquid Properties at 20°C

Experiment	Liquid	Density[a] (kg/m^3)	Viscosity[a] (kg/(m-s))	Surface Tension[b] (mN/m)
Series 1	De-ionized, distilled water (without dye)	998	1.002×10^{-3}	71.1
Series 1 - 3	Dyed, de-ionized, distilled water[c]	998	1.002×10^{-3}	66.4
Series 2	Dyed n-dodecane[d]	745	1.378×10^{-3}	25.2

[a]values obtained from CRC Handbook of Chemistry and Physics
[b]measured with a CSC Du Nouy Tensiometer (CSC Scientific Company, Inc., Fairfax, VA)
[c]dyed with 0.2% Liquitint (Milliken Chemical, Inman, SC)
[d]dyed with 0.5 g/L Spectra oil red (Spectra Colors Corp., Kearny, NJ)

experiments. Two of the fractures consisted of smooth, flat glass and acrylic parallel plates. A third fracture was assembled by mating an obscure glass plate to a flat glass plate. The fourth fracture used in these experiments consisted of a piece of obscure plate glass sandblasted with 80 grit alumina silica mated to a flat glass plate. The surface roughness created by sandblasting is on the order of 10 μm (*Kneafsey and Pruess*, 1998). In this series of experiments, water was supplied to the initially dry plates at a constant flow rate by means of a syringe pump (Model 33, Harvard Apparatus, South Natick, MA). A hypodermic needle (26G1, Becton-Dickinson, Rutherford, NJ) was placed at the top of the plates to deliver water into the plates.

A second series of experiments was conducted to measure the blob velocities in acrylic parallel plates. In these experiments, water or n-dodecane was manually injected into the plates using a syringe since a constant flow rate did not have to be maintained for these measurements.

In a third series of experiments, rivulet flow was examined using glass and acrylic plates. The plates were assembled in two different ways. Parallel plates were used to measure the rivulet width as a function of flow rate and a wedge fracture which had apertures increasing linearly from top to bottom was used to examine the effect of aperture variability on rivulet flow. To create the wedge fracture, shims with thicknesses of 0.08 mm to 1.58 mm were placed at the corners of the top and bottom of the plates, respectively. For the length and apertures used in our wedge fracture, b_o = 0.08 mm and d = 1.69 cm in Equation 4.13. In the experiments conducted on the parallel plates, the flow rate was increased from 5 ml/hr to 55 ml/hr without reassembling the plates. In the experiment conducted on the wedge fracture, the plates were reassembled each time a different flow rate was used. The pressure at the inlet of the wedge fracture was monitored with a pressure transducer (DP15-26, Validyne Engineering Corp., Northridge, CA), as shown in Figure 4.3.

4.3.2. Characterization of Surfaces and Apertures

Side-view images of drops of dyed water on the glass, acrylic, and obscure glass were captured using the video camera and contact angles were measured from the images. The static contact angle of water dyed with 0.2% Liquitint was approximately 15° on the flat glass, 60° -

65° on acrylic, and 40° - 45° on the obscure plate. The contact angle measured on a rough surface is also referred to as the apparent contact angle (*Dullien*, 1992). Water with and without dye spread immediately upon contact with the sandblasted plates and therefore has a contact angle of zero.

A capillary rise experiment was performed to estimate the apertures in the obscure-flat glass plate combination. For vertical parallel plates, the aperture corresponding to the height of rise of the liquid (h) is given by:

$$b = \frac{2\sigma \cos\gamma}{\rho g h} \tag{4.17}$$

where σ is the surface tension and γ is the static contact angle of the water on the surface. Water dyed with 0.2% Liquitint by volume was used for this measurement. The height of water rise in these plates varied between 5.1 and 7.0 cm and the maximum and minimum static contact angles measured for the obscure plate (40° and 45°) were used to obtain the largest possible ranges of apertures. Using these values, the range of apertures is estimated to be between 0.13 – 0.20 mm.

4.4. Results and Discussion

4.4.1. Visual Observations

Images of the liquid distribution in the four plates used in the finger advancement and drainage experiments are shown in Figures 4.4a-d. As the water entered the plates, a finger with a width between 0.5 – 1.0 cm formed in the plates. The length of the finger increased while the width remained approximately constant until the finger drained in the glass, acrylic, and obscure glass plates. The liquid distribution before and after drainage in the glass, acrylic, and obscure plates is shown in Figures 4.4a-c. After drainage, the finger consists of a blob and rivulet, similar to observations from the flow visualization experiments conducted by *Su et al.* (1999). The blob of water on the glass plates is considerably smaller than the blobs in the acrylic and obscure glass

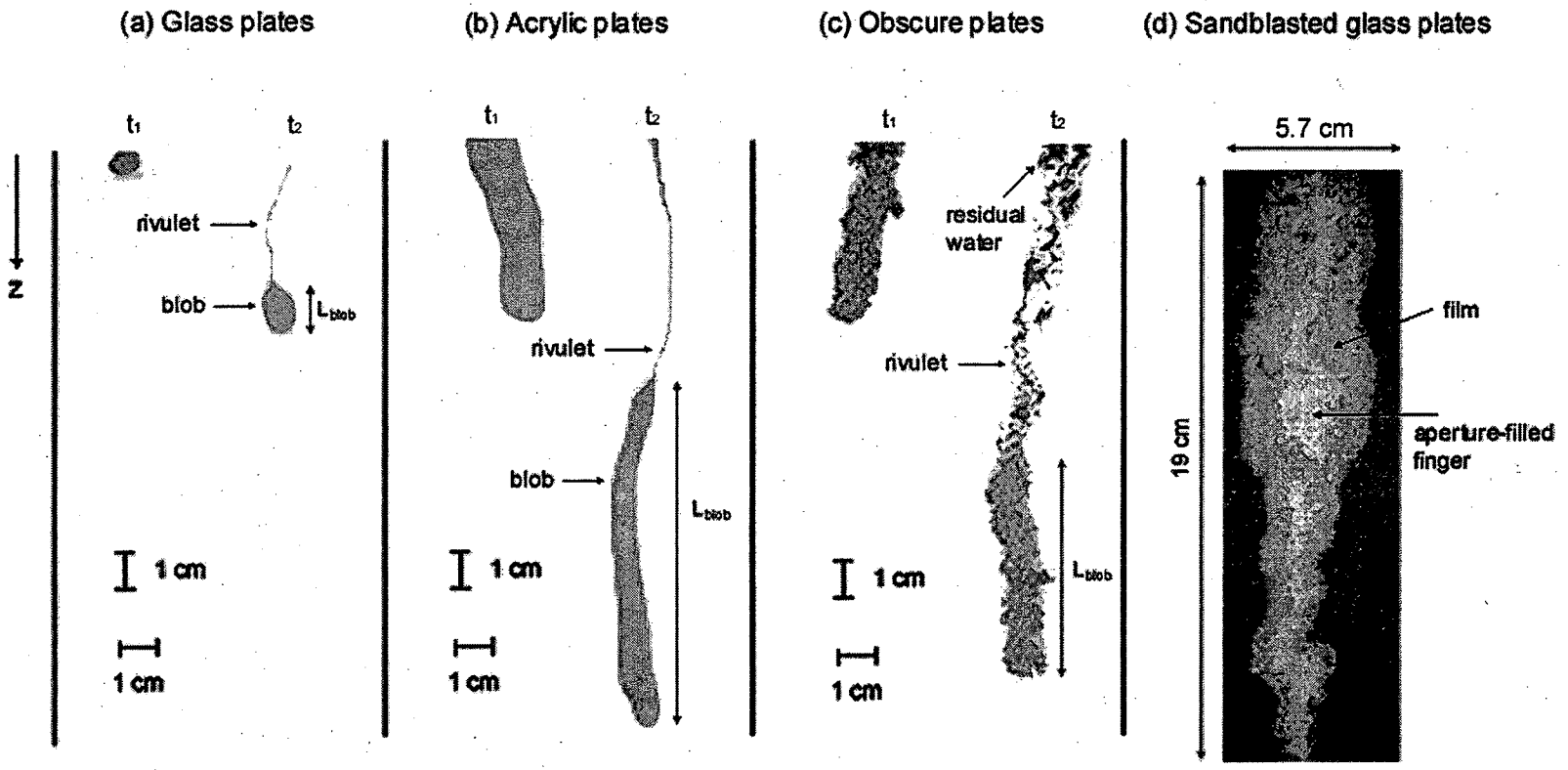

Figure 4.4. (a)-(c) Liquid distribution on three different surfaces, Q = 5 ml/hr and β = 85°. Before drainage (t_1) and after drainage (t_2). (d) Liquid distribution in sandblasted plates, Q = 2 ml/hr, β = 15°.

plates. Water becomes trapped across portions of the width of the region wetted by the advancing finger because of the roughness of the obscure plates. The rivulet in the obscure plates is also more tortuous than the rivulet which forms in the flat plates. The critical length at which the finger drained for these different surfaces is summarized in Table 4.3. The critical length is larger on the acrylic and the obscure plates compared to the glass plates because of the differences in wettability and surface roughness.

The liquid distribution of the water in the sandblasted plates is shown in Figure 4.4d and is considerably different than the distribution in the other three plates. In the sandblasted plates, a saturated finger formed that did not drain regardless of the angle of inclination. Almost immediately after water was introduced, films spread adjacent to this saturated finger due to the small-scale roughness on the plates. Since the water was not dyed, the saturated regions appear brighter than the films surrounding it in Figure 4.4d. The formation of films surrounding the finger is similar to the wetted regions that form adjacent to the nearly saturated fingers in porous media that do not fill the pores and move as a vapor or film (*DiCarlo et al.*, 1999).

4.4.2. Finger Velocities and Contact Angle Hysteresis

The finger velocities were obtained from plots of the finger front as a function of time shown in Figure 4.5. Data for the smooth glass (b = 0.25 mm) and acrylic plates are shown in Figure 4.5a and the advancing meniscus in the glass (b = 0.15 mm) and obscure plates are shown in Figure 4.5b for $\beta = 85°$. The break in the slope of the curve indicates the transition to finger drainage. The results from the sand-blasted plates are not evaluated in this section since we are interested in comparing the rates of advancement where finger drainage occurred. Measurements of the finger velocities before and after drainage are summarized in Table 4.3. Measurements were also made for $\beta = 20°$ on the different surfaces (except for the smooth glass plates with b = 0.15 mm) and those results are also included in Table 4.3. After drainage, the finger velocity increases on all the surfaces and at all the angles of inclination except for the obscure plates inclined to 20° where the velocity remained constant before and after drainage. The finger

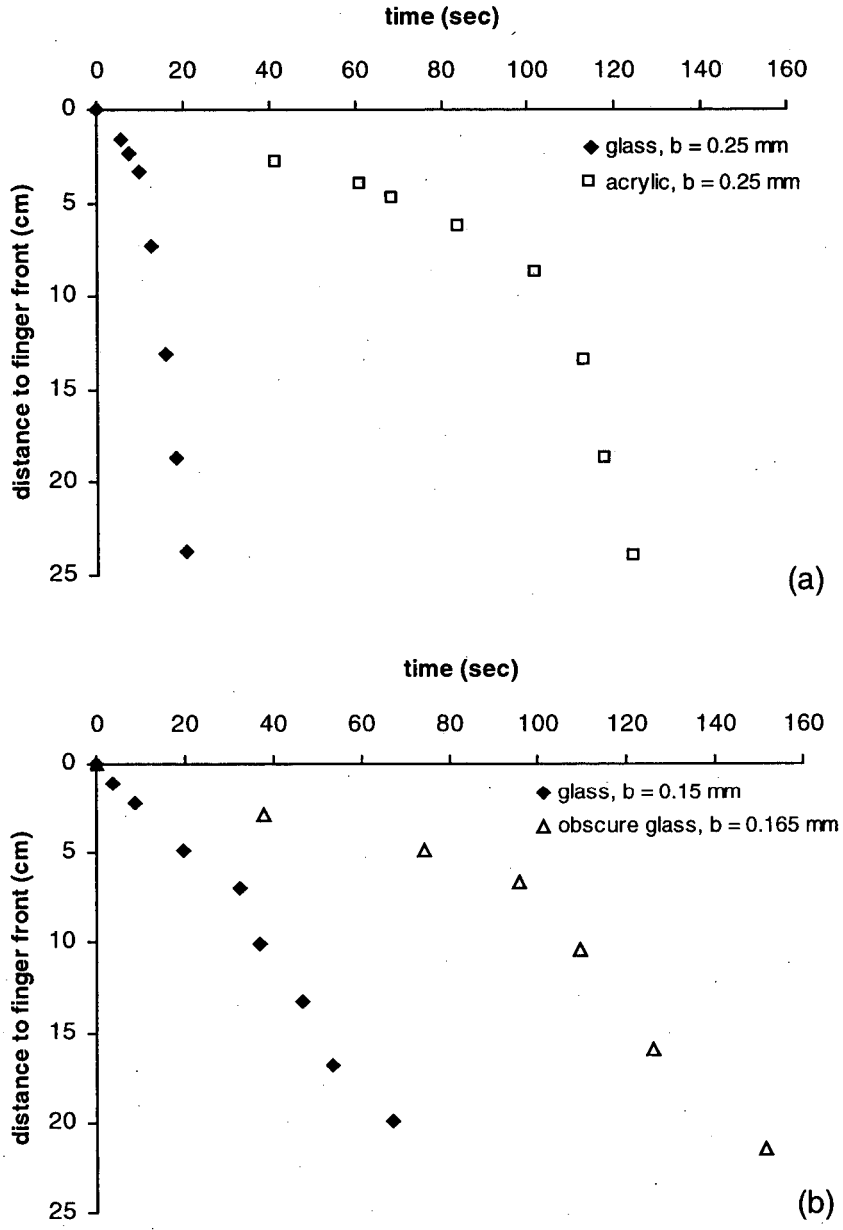

Figure 4.5. Plots of the advancing meniscus of the finger as a function of time on the (a) glass and acrylic plates and (b) glass and obscure plates. $Q = 5$ ml/hr and $\beta = 85°$.

Table 4.3. Summary of Parameters from the Finger Advancement and Drainage Experiments, Q = 5 ml/hr

Surface	Liquid	b (mm)	β (deg)	u_f (cm/s) before drainage	u_f (cm/s) after drainage	L_{crit} (cm)	L_b (cm)	$\cos\gamma_r - \cos\gamma_a$
Glass	water	0.15	85	0.25	0.44	2.0	3.2 ± 0.1	0.31
		0.25	20	0.10	0.77	2.0	3.0 ± 0.5	0.11
		0.25	85	0.31	1.87	1.0	1.7 ± 0.1	0.20
Acrylic	water	0.25	20	0.03	*NA*	14.0	*NA*	--
		0.25	85	0.07	0.68	5.0	7.8 ± 0.5	1.28
Obscure glass	water	0.165	20	0.10	0.10	18.0	19.0 ± 1.5	0.62
		0.165	85	0.07	0.26	6.5	7.4 ± 0.9	0.65

velocity is slower on the acrylic and obscure plates compared to the glass plates with the same aperture.

Assuming that the finger velocity after drainage is controlled by the blob, the contact angle hysteresis due to the moving blob can be calculated using Equation 4.9. The average length of the blob measured after drainage was used in the calculations (Table 4.3). For a particular surface, the hysteresis was slightly larger at the higher angle of inclination. The hysteresis increased at the higher angle because the velocity of the blob and the radius of curvature at the advancing air-water interface became larger, which increased the difference in the cosines of the advancing and receding contact angles. The change in contact angle hysteresis is not too significant from the low to high inclination angle, but depends strongly on the wettability and surface roughness. Contact angle hysteresis is more significant on surfaces that are less wetting. On rough surfaces, contact angle hysteresis can be reduced or enhanced compared to smooth, flat plates. Contact angle hysteresis was eliminated when the roughness was on the order of 10 μm (sandblasted plates), but became significant when the roughness was on the order of 100 μm (obscure plates).

For liquids that perfectly wet a surface under static conditions, finger drainage in fractures is not expected to be significant because the difference in the advancing and receding contact angles is small. In the flow visualization experiments described in *Geller et al.* (in press), n-dodecane, which perfectly wets epoxy, did not experience significant drainage as it advanced down an initially dry epoxy fracture replica, whereas water, which is intermediate wetting on epoxy, drained. Liquid films and residual liquid will also affect drainage of liquids. Liquid films present on the fracture surface after drainage will reduce the advancing contact angle for subsequent infiltration events. Finger drainage did not occur when water was introduced into obscure glass plates with residual water (*Glass and Nicholl,* 1996).

4.4.3. Blob Migration

In order to determine whether the finger velocities after drainage are controlled by the advancing blob, the velocities of disconnected blobs, u_{blob}, (no longer attached to the rivulet)

were measured to compare with the finger velocities measured when the rivulet was still connected to the blob. Measurements of the velocities and lengths of our disconnected blobs of water in the acrylic plates are presented in Table 4.4. The disconnected blob velocities change dramatically depending on the length of the blob. Two blobs had lengths of approximately 6 cm while the other two blobs had lengths over 8 cm. Comparison of the disconnected blob velocities with the velocities in Table 4.3 (β = 85°, acrylic plates) indicate that the shorter disconnected blob velocities are similar in magnitude to the velocity of the finger before drainage occurred. The velocities of the longer blobs are closer in magnitude to the velocity of the finger measured after drainage occurred. The lengths of the longer, disconnected blobs are also close to the average length of the blob after the finger drained in the acrylic plates (Table 4.3). Therefore, these measurements indicate that the blob was controlling the velocity after the finger drained in our experiments.

Blob migration is also dependent on the magnitude of contact angle hysteresis. If the contact angles are zero, the blob velocity should be approximately equal to the gravity-driven flow velocity. This was examined by measuring the velocity of disconnected n-dodecane blobs at two angles of inclination (20° and 85°) in acrylic plates with a constant aperture of 0.25 mm. The velocities of the blobs, which are summarized in Table 4.4, are still about half the magnitude of the saturated gravity-driven flow velocity even though the static contact angle of n-dodecane on the acrylic is zero. These results indicate that the advancing contact angle becomes non-zero when the blob moves, which reduces the velocity from the saturated hydraulic conductivity. Therefore, when flow proceeds as a series of blobs migrating down the fracture, contact angle hysteresis still plays an important role in velocity and transport predictions even if the liquid is perfectly wetting under static conditions.

4.4.4. Rivulet Flow Through Parallel Plates

The measured width of the rivulet on glass and acrylic plates as a function of flow rate is summarized in Table 4.5 and plotted in Figure 4.6. The width is assumed to be the distance

Table 4.4. Summary of Parameters from Blob Velocity Experiments

Surface	Liquid	b (mm)	β (deg)	u_{blob} (cm/s)	u_{sat} (cm/s)	u_{blob}/u_{sat}	L_{blob} (cm)	$\cos\gamma_r - \cos\gamma_a$
Acrylic	water	0.25	85	0.04	5.08	0.008	5.7	1.06
				0.05		0.01	6.3	1.17
				0.65		0.13	8.1	1.33
				0.75		0.15	8.5	1.36
Acrylic	n-dodecane	0.25	20	0.51	0.94	0.54	3.2	0.18
	n-dodecane	0.25	85	1.38	2.75	0.50	1.8	0.32

Table 4.5. Rivulet widths Measured in Glass and Acrylic Parallel Plates

Q applied (ml/hr)	Predicted width (mm)	Measured width on glass plates (mm)	Measured width on acrylic plates (mm)	Q_{calc}, glass plates (ml/hr)	Q_{calc}, acrylic plates (ml/hr)
5	0.3	0.1	0.4	--	--
9.5	0.6	0.2	0.5	--	--
27	1.7	0.9	1.3	10	21
55	3.6	2.1	2.8	28	44

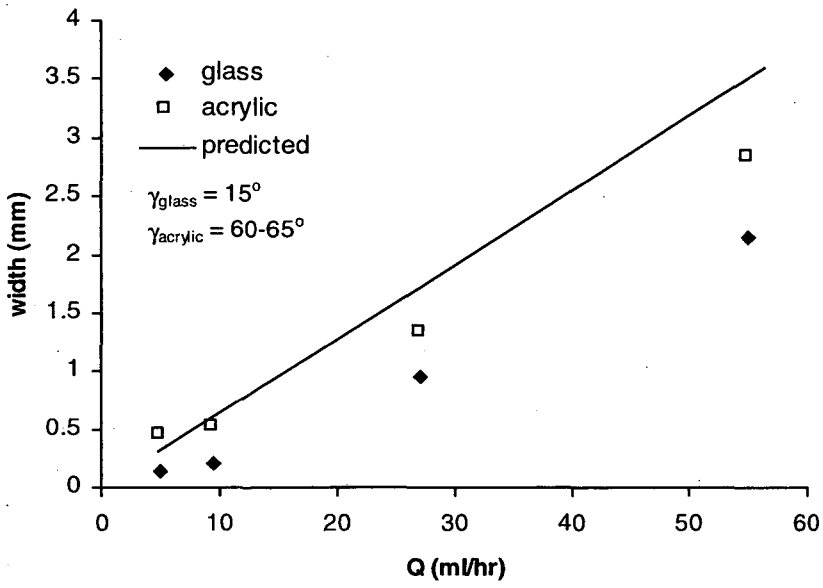

Figure 4.6. Rivulet width in parallel plates as a function of flow rate.

between the two air-water menisci, w_r, as indicated in Figure 4.2. The solid line in Figure 4.6 is the predicted width of the rivulet obtained by substituting the applied flow rate into Equation 4.10. The rivulet widths on the acrylic plates are larger and much closer to the predicted values calculated flow rates, Q_{calc}, corresponding to the rivulet widths measured at the two highest flow rates applied are summarized in Table 4.5. These flow rates were also calculated using Equation 4.10. The flow rates through the rivulet at the two lower flow rates applied were not calculated since the measured widths were too narrow for Equation 4.10 to be valid. On the glass plates, the calculated flow rates are considerably lower than the applied values, indicating that a significant portion of the volumetric flux must occur through the corner regions of the rivulet. Therefore, the contribution of flow through these corner regions is important when rivulet flow occurs on strongly wetting surfaces.

4.4.5. Effect of Aperture Variability on Rivulet Flow

Figure 4.7 is the plan view of the liquid distribution in the wedge fracture. A wider region of water, or capillary pool, is present at the top of the fracture where the apertures are smaller, and below this region, a rivulet forms. The liquid distribution is very similar to the distribution of water in the flow visualization experiments conducted on an epoxy fracture replica by *Su et al.* (1999). The rivulet underwent cycles of snapping and reforming at all the flow rates used in this experiment. A sequence of the intermittent rivulet in a wedge fracture is shown in Figure 4.8 with a corresponding side view sketch of the liquid distribution in the rivulet. The plates were than the widths measured on the glass plates. The too narrow to obtain actual images of the liquid distribution from the side.

An image of the rivulet and advancing blob is shown in Figure 4.8a. Different numbered regions are shown in the figure to indicate changes in the liquid distribution across the rivulet as the apertures become progressively large. In region 1, the liquid at the top of the rivulet completely spans the aperture, as indicated in sketches of the cross-section shown towards the bottom of Figure 4.8. In region 2, the liquid across the rivulet is barely connected by a thin liquid

bridge. The rivulets do not connect across the aperture and form two streamlets in region 3. The advancing blob is located in region 4 and the liquid spans the entire aperture in the blob. After the advancing blob migrates some distance, the rivulet detaches just above the blob due to the weight of it (Figure 4.8b). Once the connection with the blob is broken, the streamlets become unstable and the liquid spreads on the surface, as shown in region 5 in Figure 4.8c. The portion of the rivulet in region 2 recoils into the smaller apertures due to surface tension (Figure 4.8c-d).

The distance traveled by the advancing blob before the rivulet detached from the advancing blob was not constant, but the distance where the streamlets began was consistent. This distance measured from the top of the plates is plotted in Figure 4.9 as a function of the inlet pressure and is also summarized in the Table 4.6. The aperture widths corresponding to where the streamlets begin are also given in Table 4.6. The predicted curve using Equation 4.16 is shown in the plot as a solid line. The predicted curve for the distance where the streamlets begin agrees well with the measured data, indicating that the instability criterion is applicable for predicting the maximum stable length of the finger.

Table 4.6. Summary of Distances and Apertures Corresponding to Streamlet Formation in a Wedge Fracture

Q (ml/hr)	h_o (cm of H_2O)	Distance where streamlets begin (cm)	Aperture width where streamlets begin (mm)
5	6	3.7	0.25
15	8.2	4.7	0.30
20	14	5.8	0.35
25	20	6.1	0.37

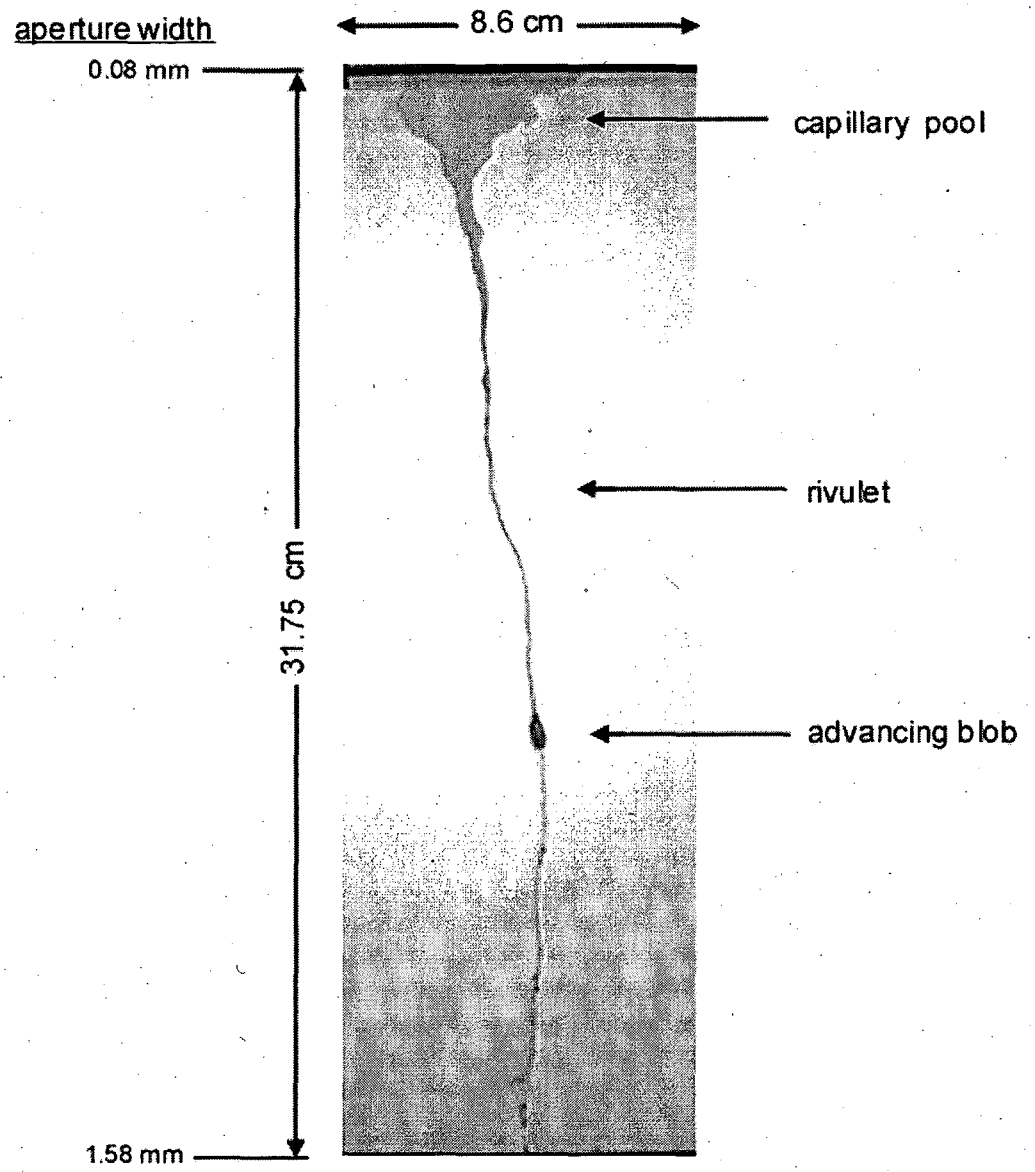

Figure 4.7. Plan view of the liquid distribution in a wedge fracture.

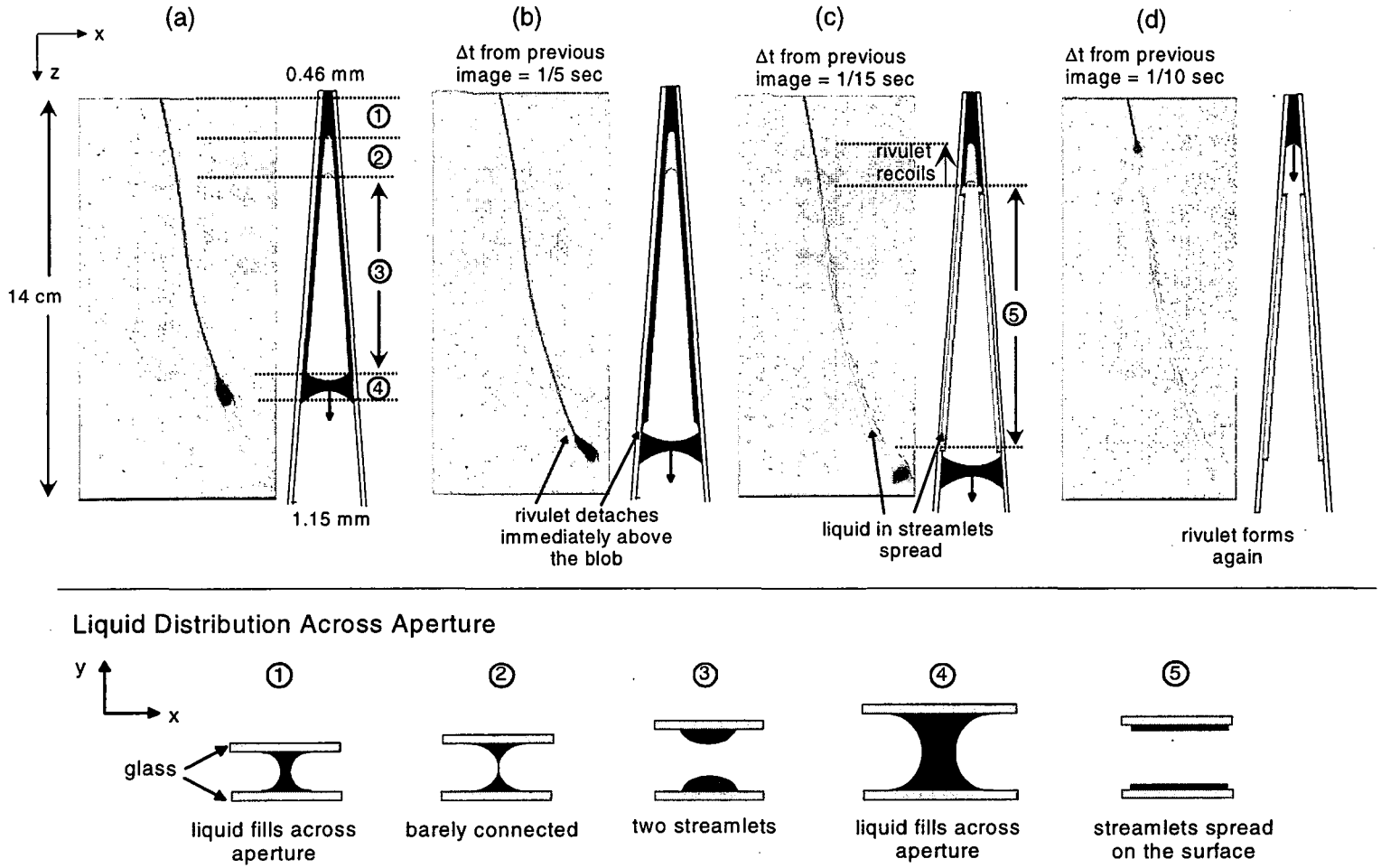

Figure 4.8. Rivulet dynamics in a wedge fracture and the corresponding liquid distribution from the side and across the aperture.

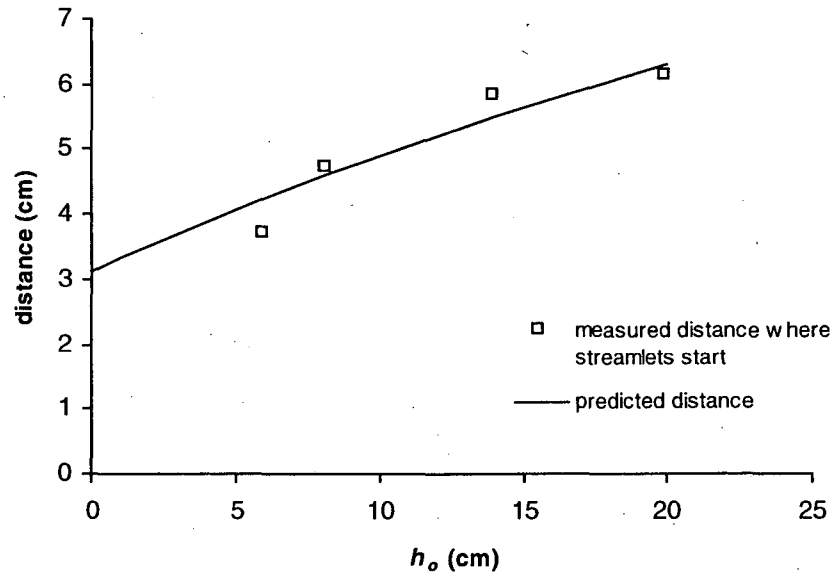

Figure 4.9. Distance where the streamlets begin in a wedge fracture as a function of the inlet pressure head.

4.5. Summary and Conclusions

Observations of finger advancement into homogeneous fractures indicated that finger drainage, or the formation a rivulet behind an advancing blob, is an important feature of unsaturated flow in fractures for a range of wettabilities and certain scales of surface roughnesses. The length of the finger before it drained was significantly longer on surfaces with intermediate wettability and surfaces with roughness on the order of 100 μm compared to a smooth, flat water-wetting surface. Finger drainage did not occur, however, on surfaces with smaller scale roughness on the order of 10 μm.

Contact angle hysteresis due to a moving blob can substantially reduce the rate of finger advancement from the saturated hydraulic conductivity of the fracture. Even when a liquid with a static contact angle of zero was used, the blob velocities were always less than the saturated gravity-driven flow velocity because of contact angle hysteresis, indicating that liquid-solid interactions play a significant role in blob migration. Understanding blob migration is important for describing intermittent flow in unsaturated fractures.

The existence of rivulets is another important feature of unsaturated fracture flow. The rivulet width was dramatically affected by the wettability of the surface. For strongly-wetting liquids, the width of the rivulet was significantly less than predicted due to flow occurring through the corner regions of the rivulet. Rivulet flow was also examined in a variable aperture fracture with apertures increasing linearly from top to bottom. In sufficiently large apertures, the liquid in the rivulet did not completely span the aperture, forming two streamlets of liquid on either side of the fracture. The rivulet underwent intermittent flow in a fracture with this type of geometry. When the streamlets detached from the advancing blob, the water in the streamlets spread nearly instantaneously along the flow path. The distance where streamlets formed in a wedge fracture was accurately predicted using a criterion originally derived to predict fingering instability.

Blob migration and rivulet flow significantly affect liquid velocities in unsaturated fractures. These flow features were examined in this chapter by varying the wettability, surface roughness, and aperture width using idealized glass and acrylic fractures. Further work to

characterize the effect of surface properties and aperture variability on flow should be performed using a variety of actual rock samples since the surface chemistry and porosity of the rock may significantly impact flow. Developing conceptual models for unsaturated fracture flow requires an understanding of how individual factors affect flow since this information will help to determine the relative contributions of these factors in more complicated systems.

5. Solute Transport Along Preferential Flow Paths in Unsaturated Fractures

5.1. Introduction

Rock fractures in the unsaturated zone can provide fast pathways for the transport of contaminants into the groundwater. Laboratory, field, and theoretical studies have demonstrated that flow proceeds along localized preferential flow paths through unsaturated fractures (e.g. *Scanlon*, 1992; *Nicholl et al.*, 1994; *Liu et al.*, 1995; *Pruess*, 1998; *Su et al.*, 1999). Preferential flow paths can dramatically decrease the residence times of contaminants compared to conceptual models that predict spatially uniform flow in fractures, subject to strong capillary imbibition effects from the rock matrix that draws the flowing liquid from the fracture (*Nitao and Busheck*, 1991; *Wang and Narasimhan*, 1993). Transport of dissolved radionuclides along preferential flow paths in unsaturated fractures is a concern at Yucca Mountain, Nevada, which is a site currently being evaluated as a potential nuclear waste repository. Evidence of fast flow through the unsaturated zone at Yucca Mountain was observed by *Fabryka-Martin et al.* (1996), where elevated levels of bomb-pulse ^{36}Cl were measured at approximately 300 m depth, indicating that infiltrating water had reached those depths within only 50 years.

Fracture roughness was recognized early on to play an important role during flow and solute transport through saturated fractures (e.g. *Witherspoon et al.*, 1980). The parallel plate idealization could not adequately describe fluid flow since the contact areas and constrictions in fractures resulted in flow taking place along preferential flow channels, which significantly impacted solute transport. The breakthrough curves (BTC's) measured in laboratory experiments conducted on saturated fractures had a steep rise at early times and multiple peaks due to preferential flow channels (*Neretnieks et al.*, 1982; 1985). The effect of flow channeling on solute transport under unsaturated conditions has been primarily limited to studies in soils. The breakthrough curves measured in soils with macropores (*Wildenschild et al.*, 1993) and in heterogeneous sands (*Wildenschild and Jensen*, 1999) had similar features as the BTC's measured in saturated fractures, such as the steep rise at early times and multiple peaks. *Birkholzer and Tsang* (1997) performed numerical simulations of flow and transport in

unsaturated, heterogeneous porous media and obtained tracer breakthrough curves that also exhibited these features.

The mechanisms controlling fast flow in unsaturated fractures have been examined in a number of laboratory experiments (*Nicholl et al.*, 1994; *Tokunaga and Wan*, 1997; *Su et al.*, 1999), but laboratory studies of transport in unsaturated fractures have been very limited. A number of field transport experiments have been performed in unsaturated fractured rocks (*Scanlon*, 1992; *Liu et al.*, 1995; *Nativ et al.*, 1995), but interpretation of field measurements is often difficult because detailed characterization of the subsurface is impossible and flow and transport in unsaturated fractures is still not well-understood. Data from laboratory experiments is generally easier to interpret than data from the field since conditions are controlled and the system is easier to characterize. In addition, laboratory experiments complement field and numerical studies by furthering the understanding of smaller-scale mechanisms which may affect processes at a larger scale.

The objective of this chapter is to conduct laboratory studies of solute transport along preferential flow paths in unsaturated, variable-aperture fractures. A miscible dye tracer experiment is conducted on a transparent epoxy replica of a natural granite fracture to identify the qualitative features of transport. Breakthrough curves of a conservative tracer are measured in several fractures to study how different flow regimes and the relative strength of gravity affect solute transport along an established flow path. These breakthrough curves are analyzed with three transfer function models and a model is also developed to describe solute transport when flow undergoes cycles of snapping and reforming, or intermittent flow. A water breakthrough curve is also calculated from measurements of the outflow rate over time after water was introduced into an initially dry and wet fracture.

5.2. Background

5.2.1. Advection-Dispersion Equation

Solute transport in porous media has traditionally been modeled with the advection-dispersion equation (ADE). The ADE for one-dimensional transport of conservative solutes in homogeneous, unsaturated media, assuming steady flow and constant cross-sectional area for flow, fluid density, dispersion coefficient, and water saturation distribution is:

$$nS_w \frac{\partial C}{\partial t} = D\frac{\partial^2 C}{\partial x^2} - u\frac{\partial C}{\partial x} \tag{5.1}$$

where n is the porosity of the porous medium, S_w is the water saturation, C is the concentration of the solute, D is the dispersion coefficient, u is the Darcy velocity, t is time, and x is distance. The dispersion coefficient quantifies the spread of the tracer due to molecular diffusion and velocity variations and is given by the following expression:

$$D = D_{mol} + \alpha u \tag{5.2}$$

where D_{mol} is the molecular diffusion coefficient and α is the dispersivity. Dispersivity values obtained from experimental breakthrough curves where fingering or preferential flow occurred were large relative to the length of the sample (e.g. *Mannhardt and Nasr-El-Din*, 1994; *Babel et al.*, 1995), violating the assumption of a small dispersivity value for the ADE to be applicable. In unsaturated fractures, conventional continuum models do not include film flow (*Tokunaga and Wan*, 1997) and temporal instabilities in the presence of constant boundary conditions (*Glass et al.*, 1996; *Su et al.*, 1999). These mechanisms may significantly affect solute transport in fractures and the interpretation of breakthrough curves.

5.2.2. *Transfer Functions*

Due to the complexity of flow in unsaturated fractures, transfer functions have been suggested as a potential alternative for field-scale transport predictions (*Chesnut et al.*, 1992; *Pruess et al.*, 1999). This approach simplifies complex systems by characterizing the output solute flux as a function of the input flux (*Jury*, 1982; *Jury* 1990). During solute transport, the transfer function is the probability density function (pdf) of the solute travel times. In reactor modeling, the pdf is referred to as the residence time distribution instead of the transfer function. The transfer functions that will be used to analyze the solute breakthrough curves in this study are the axial dispersion, reactors in series, and the lognormal models. The pdf's of the solute travel times can be characterized by the first and second moments, which are defined as follows, respectively:

$$\mu = \int_0^\infty tE(t)dt \tag{5.3}$$

$$\sigma^2 = \int_0^\infty (t-\mu)^2 E(t)dt \tag{5.4}$$

where $E(t)$ is the pdf of the breakthrough curve.

The axial dispersion transfer function model is derived from the one-dimensional advection-dispersion equation. It is assumed that the medium is homogeneous and that the velocity and dispersion coefficient are constants in the domain studied. The pdf of this model is given by (*Levenspiel*, 1972):

$$E(t) = \frac{1}{2\sqrt{\pi}}\left(\frac{Pe}{t_m t}\right)^{1/2} \exp\left[-\frac{t_m Pe}{4t}(1-t_m)^2\right] \tag{5.5}$$

where t_m is the mean residence time given theoretically by L/u, where L is the length of the sample. Pe is the Peclet number and is defined as:

$$Pe = \frac{uL}{D} \tag{5.6}$$

The first moment of the axial dispersion model is given by:

$$\mu = t_m\left(1+\frac{2}{Pe}\right) \tag{5.7}$$

The second moment for this model is given by:

$$\sigma^2 = t_m{}^2\left(\frac{2}{Pe}+\frac{8}{Pe^2}\right) \tag{5.8}$$

Information of the first and second moments allows one to determine the two unknown parameters in the axial dispersion model, t_m and Pe.

In the reactor in series model, the system is modeled as a series of perfectly mixed tanks of equal size. The pdf for n-reactors in series is given by the following expression (*Levenspiel*, 1972):

$$E_n(t) = \frac{1}{(n-1)!}\frac{t^{n-1}}{\left(\frac{\mu}{n}\right)^n}\exp\left(-\frac{nt}{\mu}\right) \tag{5.9}$$

where n is an integer describing the number of reactors. The first moment of this model is equal to the mean residence time of the solute and the second moment is a function of n and μ:

$$\sigma^2 = \frac{\mu^2}{n} \tag{5.10}$$

Equation 5.10 can be used to determine the number of reactors that best represents the measured data.

The lognormal transfer function has been successful in predicting BTC's in heterogeneous porous media (*Jury*, 1982) and has also been suggested to model breakthrough curves in heterogeneous fractured media (*Chesnut*, 1992). The pdf for the lognormal transfer function is (*Jury*, 1982):

$$E(t) = \frac{1}{t\sqrt{2\pi}\sigma_{\ln t}} \exp\left\{-\frac{1}{2}\left[\frac{1}{\sigma_{\ln t}} \ln\left(\frac{t}{\mu_{\ln t}}\right)\right]^2\right\} \tag{5.11}$$

The first and second moments of a lognormally distributed function are defined as follows (*Benjamin and Cornell*, 1970):

$$\mu_{\ln t} = \mu \exp\left(-\frac{1}{2}\sigma^2{}_{\ln t}\right) \tag{5.12}$$

$$\sigma^2{}_{\ln t} = \ln\left(\frac{\sigma^2}{\mu^2} + 1\right) \tag{5.13}$$

5.3. Apparatus and Experimental Procedures

The conditions of five experiments performed in this study are summarized in Table 5.1. A miscible dye tracer experiment was performed in Experiment 5.1, where the flow channel was initially saturated with the dyed water before water without dye was introduced into the flow channel. The water was dyed with 0.2% Liquitint by volume

Table 5.1. Summary of Experimental Conditions

Experiment	Description	Flow Cell	Q (ml/hr)	β (degrees)
5.1	Miscible dye tracer test	Epoxy replica I	5	47
5.2	Solute transport and breakthrough curves	Epoxy replica II	3 and 5	20, 45, 80
5.3		Epoxy replica I	5	20, 80
5.4		Rock-replica	5	20, 45, 80
5.5	Water breakthrough curves	Rock-replica	4	48

(Milliken Chemical, Inman, SC). The dyed water was allowed to equilibrate before the clear water was introduced into the fracture at the same flow rate. Experiments 5.2 – 5.4 were conducted to measure breakthrough curves of a conservative tracer along an established preferential flow path in an unsaturated fracture. Experiment 5.5 was conducted to measure the water breakthrough curves after water had been introduced into an initially dry and wet fracture.

An epoxy replica of a natural granite fracture was used in Experiments 5.1 – 5.3. The procedures for fabricating these epoxy replicas are detailed in *Persoff and Pruess* (1994). The same replica was used in Experiments 5.1 and 5.3 and is denoted as epoxy replica I in Table 5.1. A different replica of the same rock fracture, epoxy replica II, was used in Experiment 5.2. In Experiments 5.4 and 5.5, one half of an actual granite rock fracture from the Stripa Mine in Sweden was mated to an epoxy replica of the other half (rock-replica). The fracture used in the rock-replica experiments was a different granite fracture than the one used in Experiments 5.1 – 5.3. The rock-replica combination was used to incorporate the effects of the rock matrix and surface chemistry of the rock while still providing for flow imaging. The back of the rock was cut flat so that the rock-replica fracture could be loaded in the same manner as the replica-only experiments.

Before each experiment, the fracture replica and the actual rock fracture were washed with distilled, deionized water. The replica was then rinsed with methanol and allowed to air dry, while the rock fracture was allowed to air dry for approximately 20 hours after it had been

washed with water. The relative humidity of the room was around 50%. The dimensions of the replica-only fracture were 21.5 x 33 cm, while the rock-replica fracture had dimensions of 18.5 x 20.5 cm. The fracture replica and rock-replica were loaded between an aluminum frame with six confining bolts and then mounted over an inclined light table. The fracture replica was also compressed between two ½ inch thick transparent lucite plates. Observations from the experiments were obtained with a video camera (JVC KY-F55BU with lens JVC TY-10x6 MDPU). The video recorder (Sony SVHS no. SVO-5800) had time coding, which provided a temporal resolution of 1/30 s. Water was supplied at a constant flow rate with a syringe pump (Model 33, Harvard Apparatus, South Natick, MA) in these experiments. A small piece of filter paper (Whatman glass microfibre filters GF/D, Clifton, NJ) was placed along the center of the fracture inlet to provide capillary continuity as water was introduced into the fracture. Several pieces of filter paper were also placed at the outlet to prevent build-up of water at the outlet. Endcaps with fittings for injecting and collecting water were placed over the filter paper. A schematic of the experimental apparatus is shown in Figure 5.1.

The angle of inclination was changed without reassembling the fracture in Experiments 5.2 – 5.4. At each angle, the fracture was allowed to equilibrate to a given flow rate for about 24 hours before a step-input of a 0.5 g/L chloride tracer solution was introduced. The syringe pump operated two syringes, one containing distilled, de-ionized water and the other with the tracer solution. The water and the tracer solution were not dyed during these experiments. A three-way valve near the inlet of the fracture was used to switch from distilled water to the tracer solution without interrupting the flow. Breakthrough curves of the tracer were obtained by measuring the conductance of the water at the outlet of the fracture using gold wire electrodes. The wires were glued to the endcaps and connected to a data acquisition board (Validyne Engineering Corp., Northridge, CA) which recorded the data to a computer. The conductance at the inlet of the fracture was also measured to determine the time when the tracer reached the fracture inlet.

Comparison of the density and gravity-driven velocities can be performed to determine whether buoyancy effects are likely to be significant upon switching to the tracer solution during Experiments 5.2 – 5.4. The ratio of the gravity driven velocity (u_{grav}) and the density driven velocity ($u_{density}$) is given by:

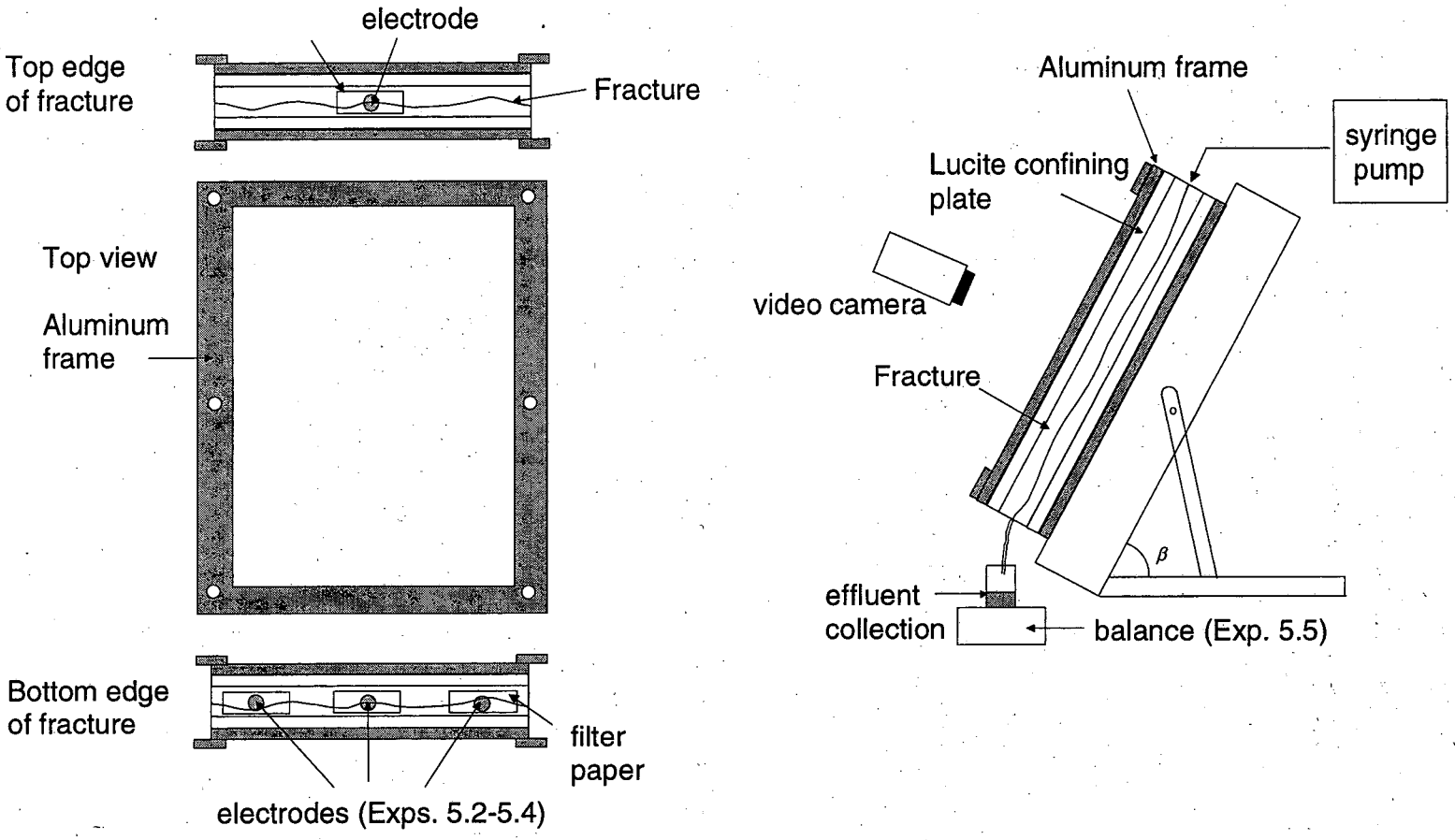

Figure 5.1. Schematic of apparatus for Experiments 5.1 – 5.5.

$$\frac{u_{grav}}{u_{density}} = \frac{\rho_w}{\rho_s - \rho_w} \tag{5.14}$$

where ρ_w is the density of water and ρ_s is the density of the solute solution. The density of water at 20°C is 998.2 kg/m^3 and the density of a solution with a chloride concentration of 0.5 g/L is 1.0041 times greater than the density of water (CRC Handbook of Chemistry and Physics). Using these values, the magnitude of the ratio in Equation 5.14 is 244, indicating that buoyancy effects are not significant.

In Experiment 5.5, water was dyed with 1 g/L fluorescein (MCB Manufacturing Chemists, Inc.) and imaged under near-UV light to observe the distribution of the flow channel as it entered the fracture. Water was introduced into the fracture with the syringe pump and the effluent mass of water was measured with a balance (Ohaus, Model TS4KD, Florham Park, NJ) and recorded every 2 s to a computer.

5.4. Miscible Dye Tracer Test

Images from the miscible dye tracer test are shown in Figure 5.2, where the clear water is introduced into the preferential flow path containing dyed water. The flow channel consists of wider regions of liquid, or capillary pools, connected to narrow channels or rivulets of liquid. Similar features were also observed in other flow visualization experiments (*Su et al.*, 1999). For this dye tracer experiment, conditions were maintained such that the flow channel did not undergo cycles of snapping and reforming, or intermittent flow. Figure 5.2a is a photograph of the flow channel before the clear water was introduced. The subsequent distribution of the clear and dyed water is shown in Figures 5.2b-d. Flow within an unsaturated preferential flow channel is quite complex, where faster flowing regions occur along the center of the flow channels. Diffusion and dispersion of the dye occurs in the flow path as evidenced by the change in the dye concentration over time. Capillary pools act as long term sources or sinks for the tracer, while rivulets transport the tracer rather quickly since they are so narrow.

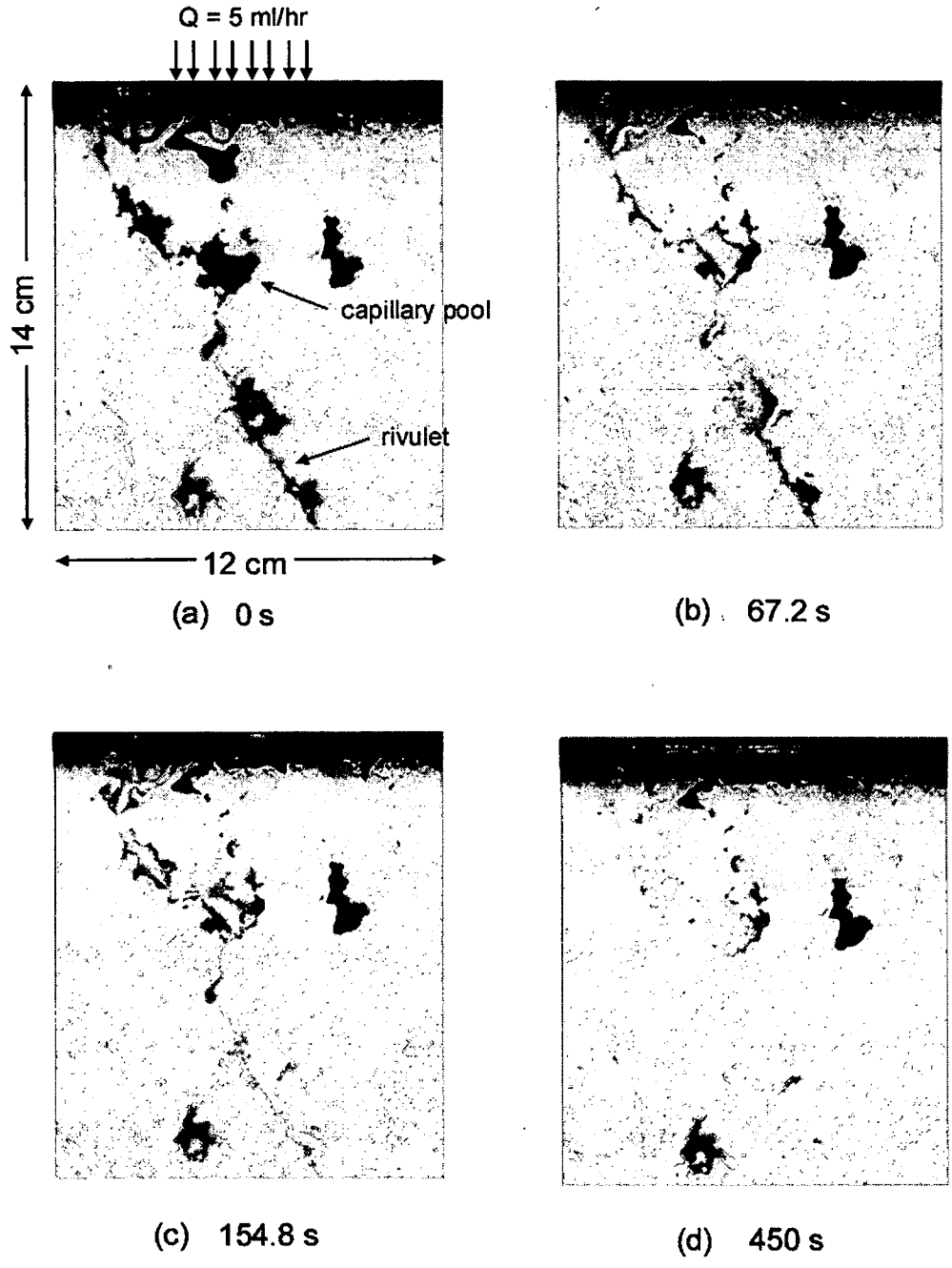

Figure 5.2. Images from Experiment 5.2 (a) before clear water was introduced and (b) – (d) at various times after the clear water was introduced.

5.5. Solute Transport Experiments

5.5.1. Observations and Results

The liquid distribution during Experiments 5.2 - 5.3 are shown in Figures 5.3 - 5.4. The flow paths from Experiments 5.2 and 5.3 were traced from captured images of the videotaped liquid distribution. Only one flow channel formed in each of these experiments, which consisted of capillary pools connected by rivulets of liquid. Even in the presence of constant boundary conditions, the flow underwent intermittent flow, where rivulets along the flow channel would snap and reform. Figures 5.3b-e and Figures 5.4b-e contain images of the flow channel undergoing one cycle of snapping and reforming during Experiments 5.2 and 5.3, respectively. The images in these figures were recorded at 45° for Experiment 5.2 and 80° for Experiment 5.3. Different modes of intermittent flow occurred in these two experiments, which have also been observed in previous experiments conducted on fractures with an idealized geometry (*Su et al.*, 1999). In Experiment 5.2, the rivulet snapping mode occurred, where the flow channel remained steady over the length of the fracture for some time before a rivulet suddenly snapped and reformed. The liquid distribution in the flow channel 2 sec after the rivulet snapped is shown in Figure 5.3a. A blob of water then forms at the location of snapping (Figure5.3b), advances down the flow path leaving a trailing rivulet (Figure 5.3c), and then reconnects with residual water downstream (Figure 5.3d). In Experiment 5.3, the pulsating blob mode of intermittent flow occurred, where blobs of water snapped from the flow channel before the channel became fully connected over the length of the fracture. In Figures 5.4a-b, the water accumulates into a blob near the top of the flow path. Figure 5.4c is an image of the liquid distribution immediately after the blob snaps and coalesces with a residual pool of water. Water in the residual pool drains and a new blob accumulates (Figures 5.4d-e).

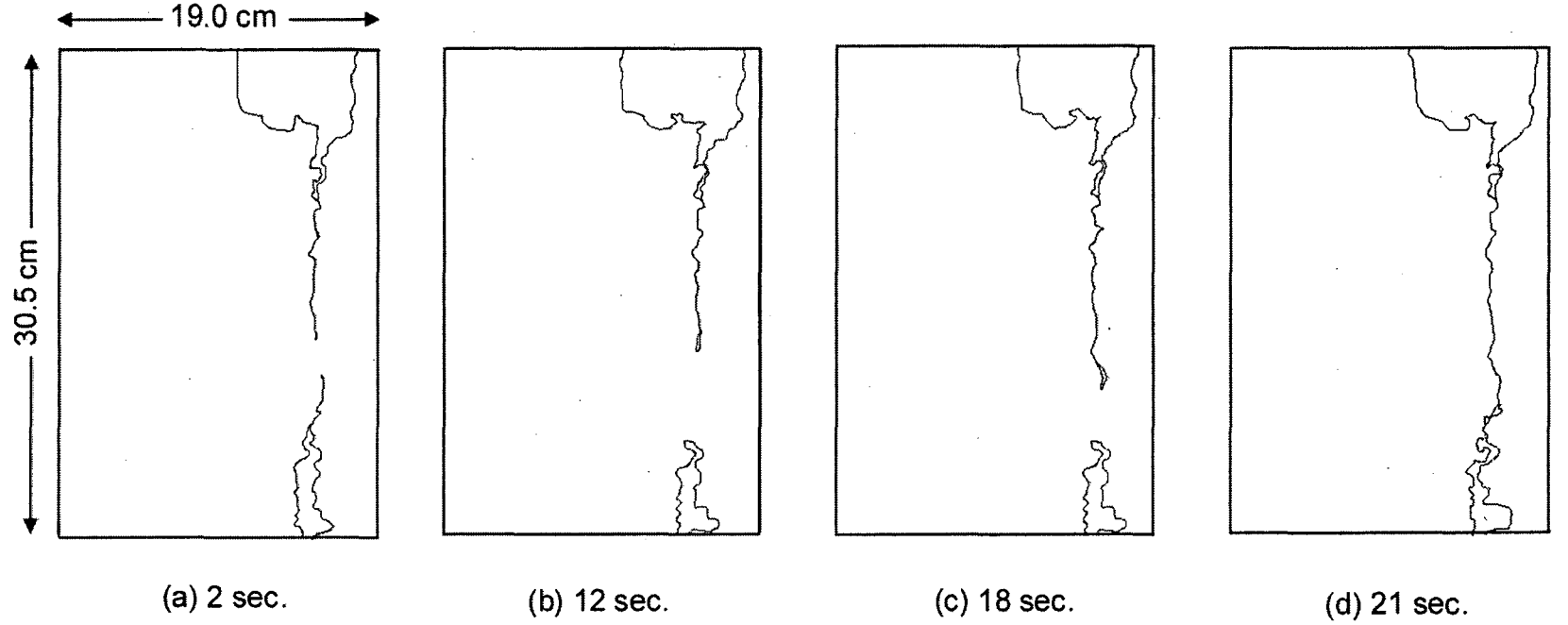

Figure 5.3. Liquid distribution during Experiments 5.2, $\beta = 45°$, $Q = 5$ ml/hr. One cycle of intermittent flow is shown in the sequence of images. Time denotes seconds after the channel had snapped.

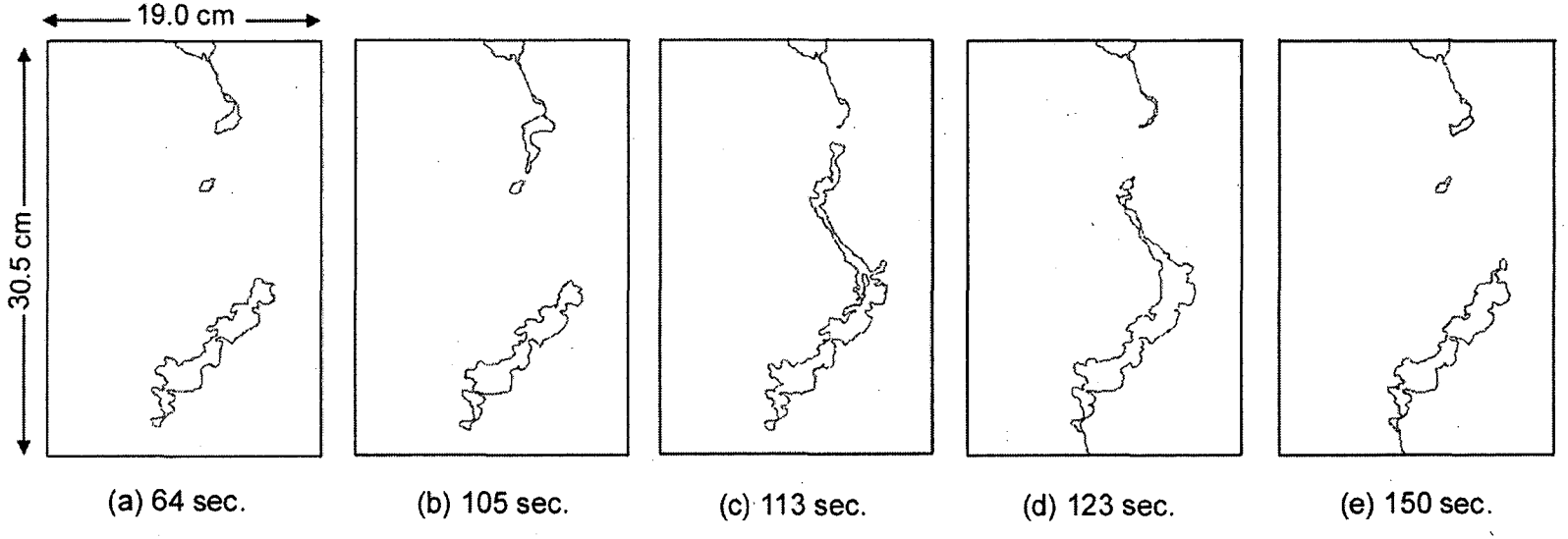

Figure 5.4. Liquid distribution during Experiment 5.3, $\beta = 80°$, $Q = 5$ ml/hr. One cycle of intermittent flow is shown in the sequences of images. Time denotes seconds after the channel had snapped.

The liquid distribution at 20° from Experiment 5.4 is shown in Figure 5.5. The flow path from Experiment 5.4 was traced by placing a transparency directly over the rock-replica fracture. Visual observations of intermittent flow in Experiment 5.4 were not recorded since undyed water was used in this rock-replica fracture and was not visible when recorded. Direct observations of the flow distribution in Experiment 5.4 indicated that the flow channel was generally steady at 20° and 45° and was intermittent at 80°.

Solute transport was quantified in Experiments 5.2 - 5.4 by measuring the BTC's of a conservative tracer. The breakthrough curves from Experiments 5.2 - 5.4 are presented in Figures 5.6a-e. The conductance of the effluent solute was normalized by the maximum conductance measured to obtain the relative solute concentration. Calibration verified that the solution conductance was linearly related to the solute concentration. The BTC's from Experiments 5.2 and 5.4 have an S-shaped curve as expected for a step-input function of solute at all the angles of inclinations and flow rates used. Tailing is also evident in these BTC's and is due to solute mixing in the capillary pools, as evidenced in the miscible dye tracer experiment. Cumulative breakthrough curves from numerical simulations of transport in unsaturated fractures also have similar features (*Liou*, 1999). The BTC's from Experiment 5.3 have very large fluctuations due to intermittent flow occurring in this experiment. The peaks in the BTC's occur whenever a blob of water from an intermittent event reaches the outlet. The fluctuations in the BTC's from Experiments 5.2 and 5.4 were not as pronounced even though intermittent flow occurred in these experiments because the time interval that the water did not contact the outlet was relatively short compared to Experiment 5.3.

The BTC's from Experiment 5.2 at 3 ml/hr do not overlap at the different angles of inclination, while the BTC's at 5 ml/hr are almost identical at all three angles of inclination, except during the early breakthrough times where there are slight differences at each angle. The trend of the travel times of the solute as a function of angle of inclination is unexpected. At both flow rates, the lowest angle has the fastest initial breakthrough, while the highest angle has the slowest initial breakthrough, which is contrary to what we would expect as the relative strength of gravity increases. The reason for the unexpected trend in the travel times as a function of gravity is because the rivulet snapping mode occurred and the total time that the flow channel

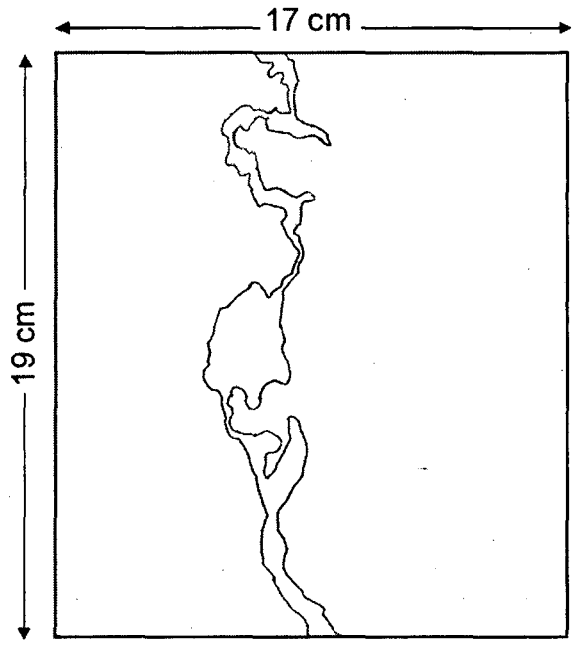

Figure 5.5. Liquid distribution during Experiment 5.4 at 20° and Q = 5 ml/hr.

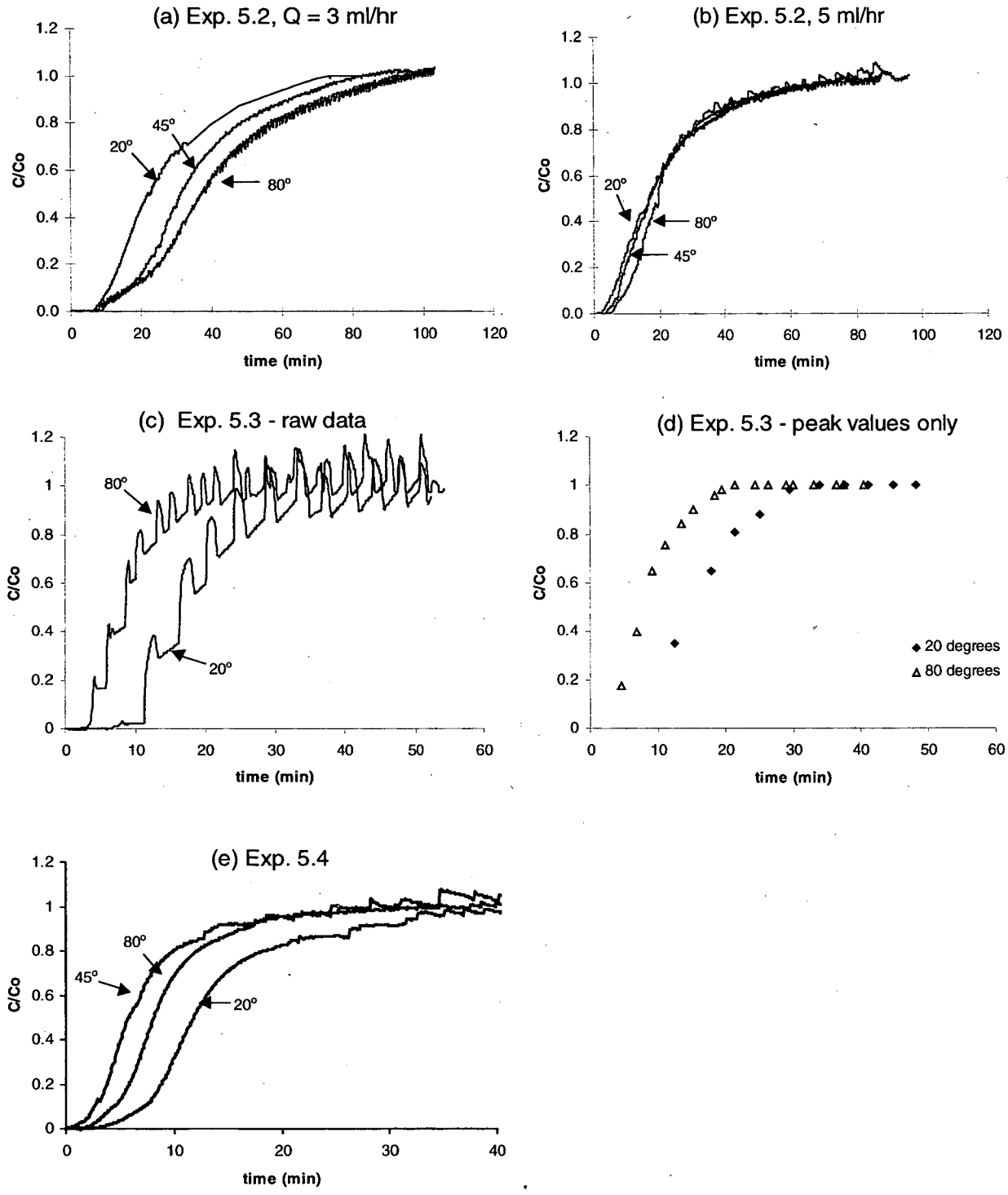

Figure 5.6. Summary of breakthrough curves from Experiments 5.2 – 5.4.

was disconnected increased at the higher angles, preventing the solute from reaching the outlet and thereby increasing the travel time.

In Experiment 5.3, the concentration reported between the peaks in the BTC's is from the conductance of the solute retained in the filter paper. The electrodes are in contact with the filter paper at the outlet and the conductance changes due to salt concentration and because the water saturation in the filter paper decreases between events. In order to examine the concentration profile without the influence of the filter paper, the average concentration of each peak was obtained from Figure 5.6c and is plotted as a function of time in Figure 5.6d. The initial arrival of solute has peak values of 20 and 40 percent of the total solute concentration before increasing more gradually. In this experiment, the travel times decrease with increasing angle of inclination, consistent with expectations. Since the pulsating blob mode occurred, the travel time of the solute was controlled by how quickly the disconnected blob reached the outlet. The velocity of the blobs increases as the relative strength of gravity increases.

In Experiment 5.4, the travel times of the solute decrease as the inclination angle increases from 20° to 45° under steady flow conditions. At an inclination of 80°, intermittent flow occurs and a longer travel time is observed. The increase in travel times of the solute at 80° is attributed to flow changing from a nearly steady regime at the two lower angles to an intermittent flow regime at 80°. This experiment suggests that intermittent flow tends to increase travel times compared to when flow is steady.

In order to summarize the results of Experiments 5.2 – 5.4, the average travel times were obtained from each of the BTC's and are presented in Table 5.2. The average travel time (t_{ave}) is defined as the time it takes for the solute to reach one half of its final concentration. The average velocities (u_{ave}) of the solute are also given in Table 5.2 and were calculated by dividing the total length of the fracture by the average travel time. In Experiments 5.2 and 5.3, the total distance from the inlet to outlet of the fracture was 32 cm and in Experiment 5.4, the distance was 20.5 cm.

Table 5.2. Parameters obtained from the BTC's in Experiments 5.3 - 5.5

Experiment	Q (ml/hr)	β (deg)	$sin\ \beta$	t_{ave} (min)	u_{ave} (cm/min)
5.2	3	20	0.36	23.0	1.4
		45	0.72	31.0	1.0
		80	0.98	37.0	0.9
5.2	5	20	0.36	17.0	1.9
		45	0.72	17.0	1.9
		80	0.98	19.5	1.6
5.3	5	20	0.34	16.5	2.0
		80	0.98	8.5	3.7
5.4	5	20	0.34	12.0	1.7
		45	0.71	6.0	3.4
		80	0.98	8.0	2.5

5.5.2. Analysis of Breakthrough Curves: Experiments 5.2 and 5.4

The pdf's of the measured BTC's were obtained by differentiating the BTC's so that the data could be analyzed with different transfer function models. Before the measured BTC's were differentiated, the fluctuations in the BTC's were smoothed out by averaging the data over two minute intervals in Experiment 5.2 and a one minute interval in Experiment 5.4. The results from Experiment 5.3 are not analyzed in this section because the initial increase in the concentration occurred over such a short time period that the pdf would have an infinite peak during the early portion of it if the BTC's had been differentiated. The breakthrough curves from Experiment 5.3 will be analyzed in the next section. The pdf's obtained from Experiments 5.2 and 5.4 are shown in Figures 5.7a-c for $\beta = 45°$. The pdf's are not symmetrical and have peaks at the early times. The first and second moments calculated from the measured data at all the angles of inclination are summarized in Table 5.3. These values were used in Equations 5.5, 5.9, and 5.11 to obtain the theoretical pdf's corresponding to the axial-dispersion, reactor in series, and the lognormal models, respectively. The number of reactors used in the reactor in series model was calculated using Equation 5.10 and is summarized in Table 5.3. The Peclet numbers obtained from the axial

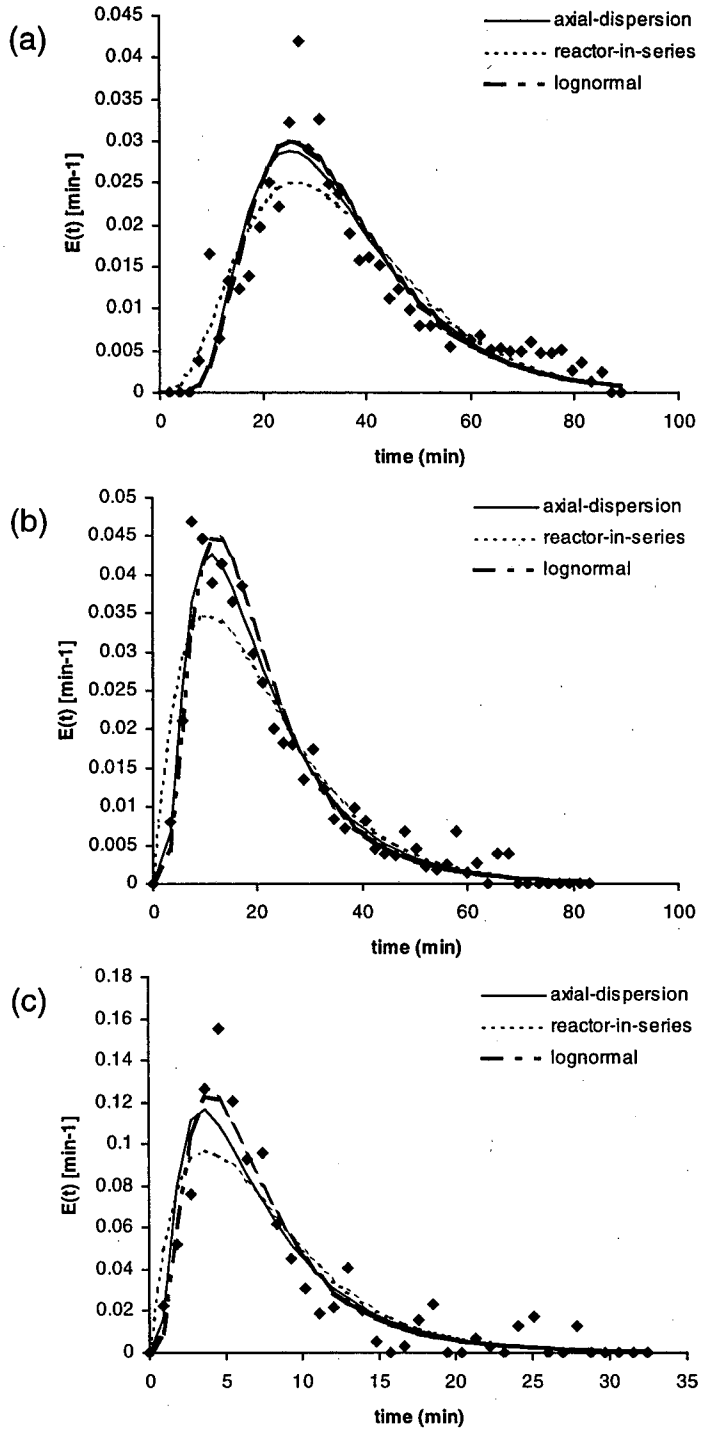

Figure 5.7. PDF's of the measured cumulative BTC's at $\beta = 45°$ and the corresponding predictions with the different transfer function models for (a) Experiment 5.2, $Q = 3$ ml/hr (b) Experiment 5.2, $Q = 5$ ml/hr and (c) Experiment 5.4.

Table 5.3. Summary of the first and second moments obtained from the pdf's and the parameters used in the different transfer functions.

Experiment	Q (ml/hr)	μ	σ^2	$\mu_{ln\,t}$	$\sigma^2_{ln\,t}$	n	Pe
5.2	3	28.2	325.0	23.8	0.34	2	3.4
		35.7	301.4	32.1	0.21	4	5.1
		39.1	364.8	35.1	0.21	4	5.1
5.2	5	20.0	191.7	16.5	0.40	2	3.1
		21.1	196.8	17.6	0.37	2	3.2
		23.1	196.7	19.8	0.31	3	3.7
5.4	5	14.4	67.2	10.8	0.37	3	4.1
		7.6	29.8	6.1	0.42	2	2.8
		9.6	31.2	8.3	0.29	3	3.9

dispersion model are also presented in Table 5.3. The curves corresponding to the different transfer function models are plotted in Figure 5.7 with the measured data. The peak of the pdf is generally underpredicted by all of the models, but the trend at the early and late times is fairly consistent with the measured data. The axial-dispersion and lognormal model give similar predictions to the data, except the lognormal model is slightly better in predicting the peak values of the data. The reactor in series has the worst fit to the measured data. Overall, the lognormal model has the best fit to the data and may therefore be appropriate for describing transport through heterogeneous, unsaturated fractures.

5.5.3. Analysis of Breakthrough Curves: Experiment 5.3

The BTC's from Experiment 5.3 were analyzed by formulating a model which accounted for solute transport when flow was intermittent. In this experiment, flow proceeded as a series of blobs which coalesced with a residual pool of water along the flow path (see Figure 5.4). Solute transport along an intermittent flow path is shown schematically in Figure 5.8 for a step-input concentration change. In this model, the blob of water that forms and disconnects is assumed to be at the inlet solute concentration. When the blob coalesces with the residual pool, the volume of water displaced from the pool must have the same volume as the incoming blob if the pool is at capillary-gravity equilibrium. Complete mixing of the solute in the blob and residual pool is assumed to occur, resulting in the following concentration of solute measured at the fracture outlet:

$$\frac{C_{out}}{C_o} = 0 \qquad n_b = 1$$

$$\left.\frac{C_{out}}{C_o}\right|_{n_b} = \frac{V_{blob}\left.\frac{C_{blob}}{C_o}\right|_{n_b-1} + (V_{res} - V_{blob})\left.\frac{C_{res}}{C_o}\right|_{n_b-1}}{V_{res}} \qquad n_b \geq 2 \qquad (5.15)$$

$$\left.\frac{C_{res}}{C_o}\right|_{n_b-1} = \left.\frac{C_{out}}{C_o}\right|_{n_b-1}$$

where n_b is the cumulative number of blobs that have formed and disconnected since the introduction of the tracer, V_{blob} is the volume of the blob saturated with solute, V_{res} is the volume of the residual pool of water, C_o is the solute concentration at the inlet, C_{out} is the concentration at the outlet, C_{blob} is the concentration of solute in the blob (assumed equal to C_o in this model), and C_{res} is the concentration of solute in the residual pool of water. Although Equation 5.15 is written in terms of the number of blobs, a certain time elapses between two successive blobs reaching the outlet. We assume that the time it takes for the disconnected blob of water to move through the fracture is minimal compared to the time it takes for the blob to form and disconnect. This assumption may no longer be appropriate in longer fractures. On relatively uniform and smooth surfaces, the blob velocity is a function of the receding and advancing contact angles and the length of the blob, as discussed in Chapter 4.

In Figure 5.9, the data from Experiment 5.3 are compared with predictions according to Equation 5.15. The volume of the blob, V_{blob}, used in Equation 5.15 was obtained by multiplying the flow rate (5 ml/hr) by the average time interval between two successive blobs reaching the outlet, which were 138 sec at 80° and 233 sec at 20°. The initial solute concentration in the residual pool is zero, while the normalized concentration in the incoming blob is assumed to be one. The aperture distribution of the fracture replica used in this experiment was not measured; therefore, the residual volume of water from this experiment could not be calculated from the images. V_{res} was changed until the best fit to the breakthrough curves in Figure 5.9 was obtained, resulting in a value of 0.6 ml at 80° and 0.7 ml at 20° for V_{res}. A smaller residual volume of water is expected at the higher angle since some of the water in the pool drains when the relative strength of gravity increases.

In calculating the predicted concentration, we assumed that only a single capillary pool was present along the flow path, which was consistent with observations of the liquid distribution from this experiment. The time lag before a concentration was measured in

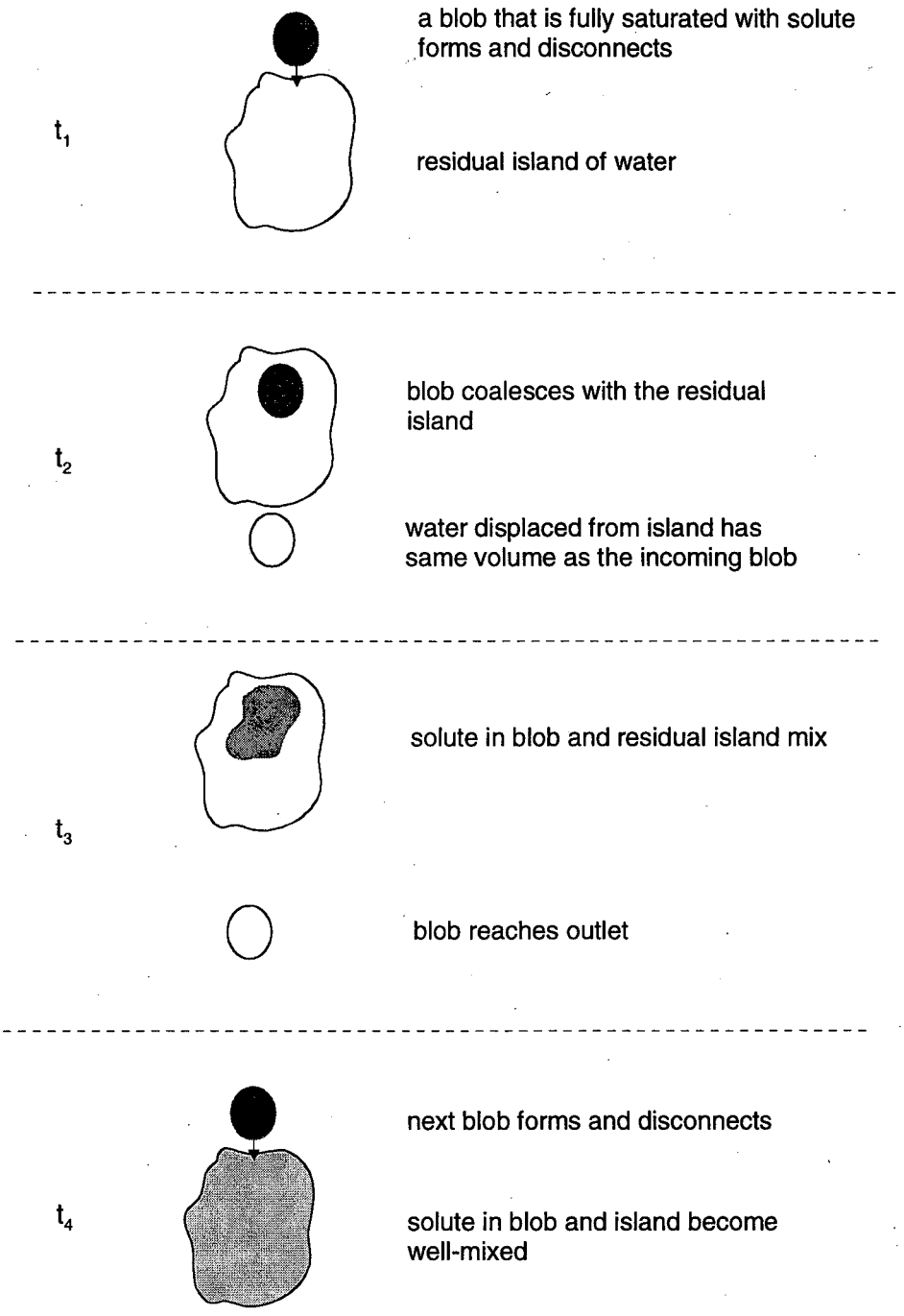

Figure 5.8. Schematic of solute transport and mixing when flow is intermittent during Experiment 5.3.

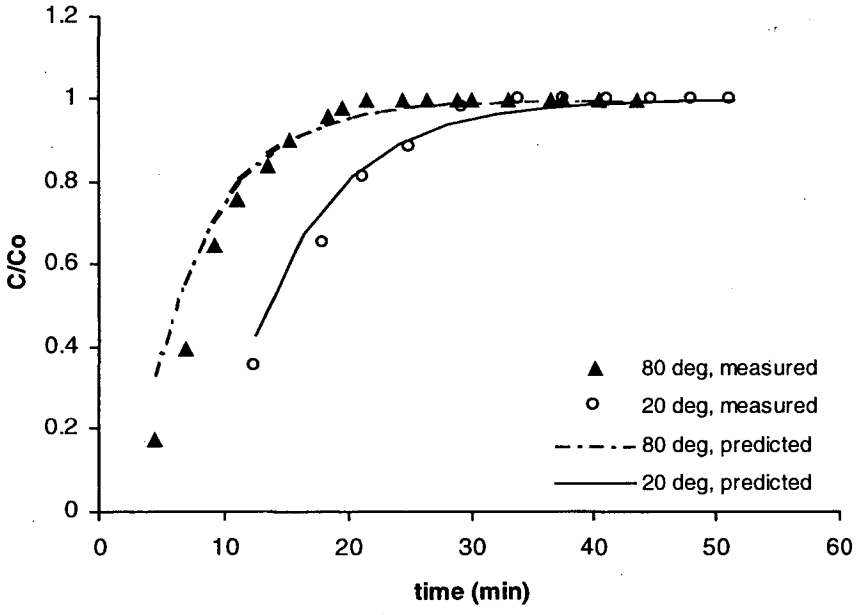

Figure 5.9. Measured data and predicted BTC for Experiment 5.3 using Equation 5.15.

Experiment 5.3 indicates that one blob reached the outlet without solute at 80°, while two blobs reached the outlet without solute at 20°. In order for these results to be consistent with the model presented in this section, the number of blobs that reach the outlet without solute should be equal to the number of capillary pools along the flow path. A single capillary pool model is still appropriate for the results at 20° since the initial blob may not have been equal to the inlet solute concentration as we assumed in the model. The tracer was probably introduced when the blob was already a considerable size, resulting in a very small concentration of solute in the first blob ($C_{blob}/C_o|_{n_i=0} << 1$). Therefore, when the next event occurred, the concentration of solute measured at the outlet was still negligible since the solute concentration in the residual pool was minimal.

5.6. Water Breakthrough Curves

The volume of effluent water collected over time after water was introduced into an initially dry fracture during Experiment 5.5 is presented in Figure 5.10a. Only one preferential flow channel formed in the fracture during this experiment. Water first arrived at the outlet at 15 minutes and the initial exit flow rate exceeded the influent rate as a blob passed through. After about 20 minutes of water introduction, the net outflow rate became nearly constant, although there continued to be pulsations in outflow which decreased over time to a nearly constant period of approximately 2 min. Flow to the fracture was stopped for 30 minutes and then reintroduced into the fracture to also measure the accumulation rate of effluent water when the fracture was initially wet. Water arrived at the outlet in only 3 minutes and the net outflow rate immediately became constant. The intermittent events are also periodic once the water reaches the outlet, as evidenced by the nearly uniform time intervals of no mass accumulation. If the influent water had been fully saturated with solute upon entering this fracture, the initial conditions and previous wetting history in the fracture would significantly impact solute travel times. A reduction in the time for flow paths to establish under initially wet conditions has also been observed in other laboratory experiments (*Nicholl et al.*, 1993) and field experiments (*R. Trautz*, personal communication).

The outflow rate was obtained by differentiating the cumulative effluent water curve (Figure 5.10a). A second order polynomial was fitted to the first 5 minutes of the effluent curve from the initially dry fracture and then differentiated to obtain the outflow rate. A linear regression was performed on the remaining portion of the effluent curve to obtain the steady-state outflow rate from the slope of the line, which corresponded to a rate of 3.6 ml/hr. Since the rate of water accumulation was immediately constant when the fracture was initially wet, a linear regression was only performed on these data, which also resulted in a steady-state outflow rate of 3.6 ml/hr. The steady-state outflow rate is lower than the input rate (4 ml/hr), which may have been partially due to imbibition into the rock matrix. This can be determined by calculating the theoretical imbibition rate into this Stripa granite. Assuming horizontal imbibition into the rock matrix, the distance to the imbibition front, x_f, can be estimated with the following equation derived by *Kao and Hunt* (1996):

$$x_f = B\frac{\sigma}{\mu}k^{1/4}t^{1/2} \tag{5.16}$$

where σ is the surface tension of water, μ is the viscosity of water, k is the permeability, and B is a geometric factor. Equation 5.16 can be differentiated to obtain the imbibition rate and multiplied by the surface area of the finger (SA) and porosity of the matrix to obtain the rate in terms of a volumetric flux, Q_i:

$$Q_i = \frac{nB\left(\frac{\sigma}{\mu}\right)^{1/2}k^{1/4}SA}{2t^{1/2}} \tag{5.17}$$

The surface tension and viscosity values used to calculate the imbibition rates are 72.75 mN/m and 1.002 x 10^{-3} kg/(m-s), respectively (CRC Handbook and Chemistry and Physics). The permeability and porosity of the Stripa granite are approximately 10^{-22} m^2 and 0.01, respectively (*P. Persoff*, personal communication) and a value of 0.5 for B is used (*Kao and Hunt*, 1996). The

measured surface area of the flow path is 23 cm^2 after a constant liquid distribution was attained. Using these values, the theoretical imbibition rates as a function of time are very small (less than 2×10^{-3} ml/hr after the first minute) and cannot account for the difference between the input rate and measured outflow rate (0.4 ml/hr). The discrepancy in the input and outflow rates must be primarily due to errors in measurement and calibration of the syringe pump. The measured steady-state outflow rate is assumed, therefore, to be approximately equal to the input rate.

The water breakthrough curves for Experiment 5.5 were calculated by normalizing the outflow rates by the input flow rate and are presented in Figure 5.10b. The shape of the water breakthrough curves for water entering an initially dry fracture is much different than the breakthrough curves obtained from numerical simulations, which increase almost immediately to the steady-state flow rate for a single preferential flow path in an unsaturated fracture (*Liou*, 1999). When water was introduced into the initially wet fracture, the steady-state flow rate was immediately attained when the water reached the outlet, resulting in a step-increase function for the water breakthrough curve that is similar to the results from numerical simulations.

The arrival of a high flow pulse in the water breakthrough curve from the initially dry fracture was due to accumulation of liquid in an advancing blob as it entered the dry fracture. The advancing blob contained more liquid than the fracture could retain, and once the finger reached the outlet, the excess water drained quickly to its steady-state liquid distribution, as shown in Figure 5.11. *Prazak et al.* (1992) also measured higher outflow rates during the initial breakthrough of the water from sand columns compared to the rates measured at later times.

5.7. Summary and Conclusions

Laboratory studies were conducted to examine the factors controlling solute transport in unsaturated fractures. Qualitative aspects of solute transport were identified in a miscible dye tracer experiment conducted in a transparent replica of a natural granite fracture. Faster flowing regions were present within the preferential flow channels. Capillary pools act as long term sources or sinks for the solute, while transport along rivulets occurs quickly. Additional experiments were conducted to measure the BTC's of a conservative chloride tracer introduced

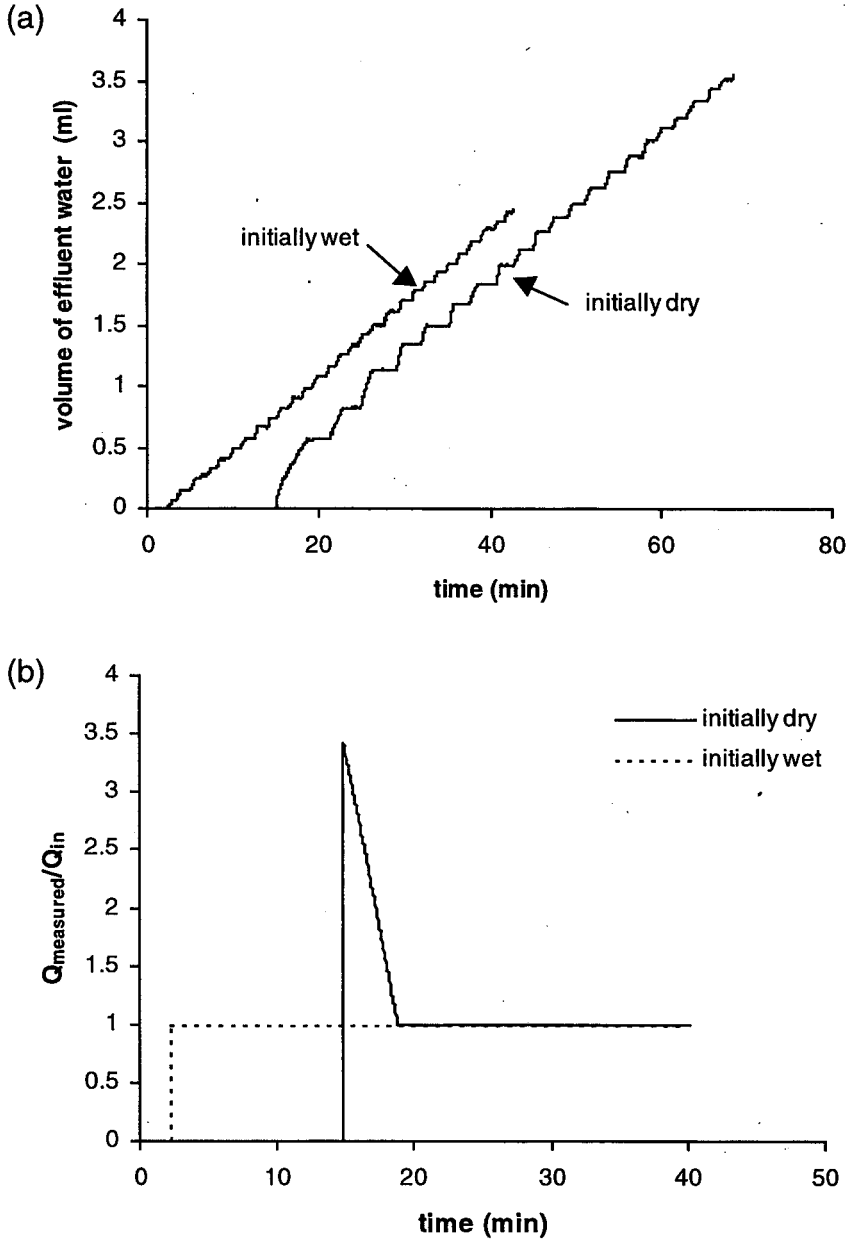

Figure 5.10. (a) Volume of effluent water collected over time and (b) the calculated water breakthrough curves for Experiment 5.5.

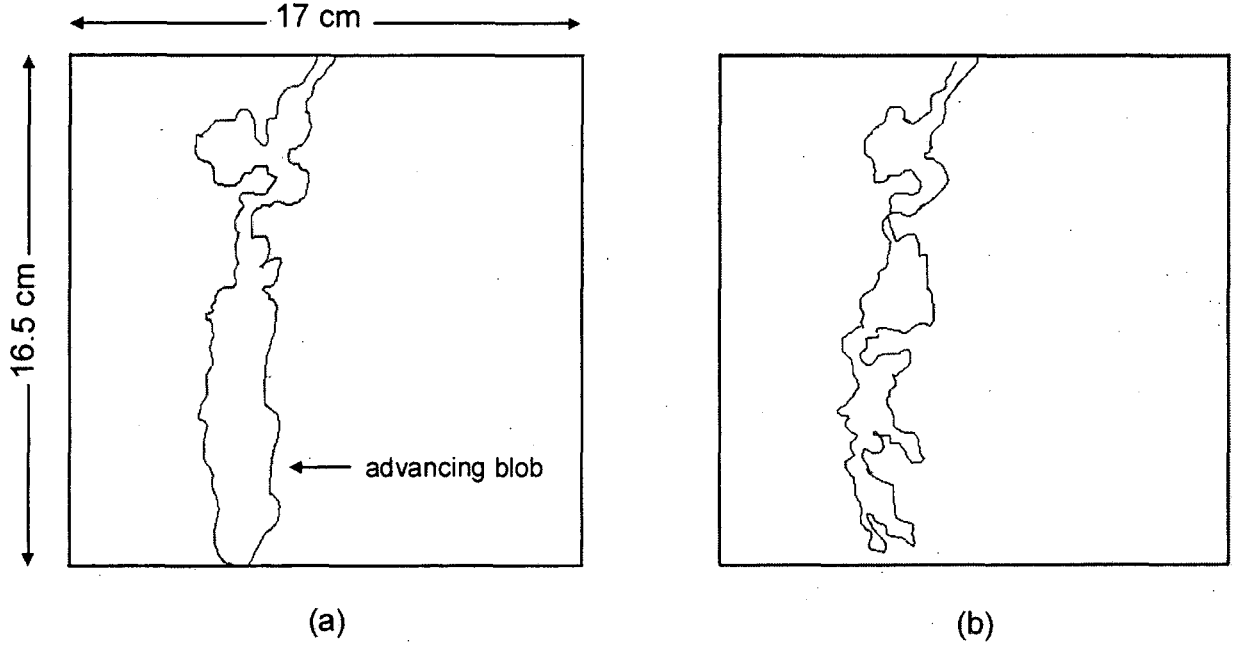

Figure 5.11. Liquid distribution (a) when the finger introduced into an initially dry fracture reaches the outlet and (b) after drainage to its steady-state configuration.

into an established preferential flow path in three different fractures. Intermittent flow had a significant affect on solute transport in these experiments. Two modes of intermittent flow occurred in two of the experiments, the pulsating blob mode and the rivulet snapping mode, affecting how the travel times of the solute changed with the relative strength of gravity. During the rivulet snapping mode, the average travel time of the solute actually increased as the relative strength of gravity increased. During the pulsating blob mode, the average travel times of the solute decreased with increasing strength of gravity as expected. In another experiment where flow changed from steady to intermittent as the angle of inclination increased, the average travel time increased when flow was intermittent compared to when flow was steady.

The breakthrough curves were analyzed with three transfer function models: the axial-dispersion, reactor in series, and the lognormal models. The lognormal transfer function fit the measured data the best, indicating that it may be applicable for modeling solute transport in unsaturated, heterogeneous fractures. A model was also formulated to describe transport when the pulsating blob mode occurred. The measured breakthrough was successfully fit to this model which assumed complete mixing of the blob containing solute with residual pools along the flow path.

Water was introduced into an initially dry and wet fracture and the subsequent outflow rates were measured over time to calculate the water breakthrough curves by normalizing the outflow rate by the applied flow rate. The initial conditions played an important role in the travel time distributions observed in the breakthrough curves. The flow channel reached the outlet five times faster when it was introduced into an initially wet fracture compared to one that was dry. In an initially dry fracture, the outflow rate was initially higher than the input rate due to the advancing finger accumulating more water than the fracture could retain, resulting in a breakthrough curve that actually decreased to a constant flow rate over time. In an initially wet fracture, however, the steady-state flow rate was immediately established when the water reached the outlet of the fracture, resulting in a step-function water breakthrough curve.

These laboratory experiments demonstrate that small-scale mechanisms can significantly impact transport in unsaturated fractures. Other factors affecting transport will inevitably occur at different scales. At larger scales, network of flow channels may join, divide, and enter into

perched water bodies. Improving conceptual models for flow and transport in unsaturated fractures requires an understanding of the processes occurring at many different scales.

6. Conclusions and Future Work

Flow visualization experiments conducted on a transparent epoxy replica of a natural granite fracture demonstrated that infiltrating water proceeds through unsaturated rock fractures along non-uniform, localized preferential flow paths. These flow paths consisted of broader, liquid-filled regions or capillary pools, connected by thin threads or rivulets of liquid. Even in the presence of constant flow and constant head boundary conditions, the flow often proceeded in an intermittent manner, where rivulets along the flow channel snapped, drained and reformed. The persistent occurrence of this behavior in our flow visualization experiments suggests that this is an important feature of unsaturated flow in fractures. The location and distribution of the preferential flow path was similar even when different liquids were used, but the wettability of the liquid had a significant effect on the rate at which the rivulets snapped and reformed. A strongly wetting liquid will spread on the fracture surface, removing liquid from the rivulets and increasing the rate at which they thin and subsequently snap.

Two modes of intermittent flow were observed. In one mode, the pulsating blob mode, the flow channel did not connect over the length of the fracture, and blobs of liquid disconnected from the flow channel when the gravitational force overcame the capillary force. In another mode of intermittent flow, the rivulet snapping mode, the flow channel remained completely connected over the length of the fracture for some time before rivulets along the flow channel suddenly snapped and reformed. This mode of intermittent flow occurred because the strong capillary force provided by the smaller apertures along the flow channels pulled the rivulet through at a faster rate than the supply of the liquid, thereby causing it to break. In order to characterize the rivulet snapping mode, the frequency of intermittent flow events were measured from several sets of experiments and related to the Bond and capillary numbers. The dimensionless frequency of events had a consistent trend as a function of the ratio of the capillary number to the Bond number squared.

Finger drainage, the dynamics of blob migration, and rivulet flow were also investigated in this study. Finger drainage, or the formation a rivulet upstream of an advancing blob, occurred over a range of wettabilities and certain scales of surface roughnesses. During blob migration,

contact angle hysteresis, which is defined as the difference in the receding and advancing contact angles, was an important factor controlling the rate at which the blobs move through the fracture. During rivulet flow, the rivulet width was affected by the wettability of the surface. For liquids that strongly wetted a surface, the width of the rivulet was less than predicted partially due to spreading of liquid adjacent to the rivulet. In sufficiently large apertures, the liquid in the rivulet did not completely span the aperture, forming two streamlets of liquid on either side of the fracture.

Solute transport in unsaturated fractures was quantified in laboratory experiments by measuring breakthrough curves of a conservative chloride tracer. The travel times of the solute were significantly affected by intermittent flow. Longer travel times were measured when flow was intermittent compared to flow that was steady. When the rivulet snapping mode occurred, the travel times actually increased with the relative strength of gravity, contrary to expectations. Some of the breakthrough curves were analyzed with three transfer function models and the lognormal transfer function fit the measured data the best, indicating that it may be applicable for modeling solute transport in unsaturated, heterogeneous fractures. A model was also formulated to describe transport when the pulsating blob mode of intermittent flow occurred and was successfully fit to the measured data. This model assumed complete mixing of the blob containing solute with residual pools of water along the flow channel.

Different boundary conditions, initial conditions, and aperture widths will give rise to a range of flow behavior in unsaturated fractures. Although a number of important mechanisms controlling flow and transport in unsaturated fractures have been characterized in this dissertation, future work should be conducted using different boundary conditions, such as episodic liquid application to the fracture, and using a larger range of aperture widths and flow rates so that other important processes controlling flow can be identified. Understanding the flow dynamics under different sets of conditions will provide a broader scope of potential flow and transport scenarios that may occur in nature. Further work should also be performed to study rock matrix-fracture interaction and the relative importance of flow through the matrix versus the fracture over longer time scales. Scale-up of flow is also an extremely important issue to address. As the scale increases, mechanisms other than those observed in laboratory-scale experiments

may control flow and transport, particularly when three-dimensional fracture networks are considered. One major challenge in scaling up flow is connecting pore-scale processes with mathematical models on the macroscale. Appropriate averaging must be performed in developing these large-scale models, using constitutive relations that incorporate important small-scale phenomena.

References

Abelin, H., L. Birgersson, J. Gidlund, L. Moreno, I. Neretnieks, H. Widen, and J. Agren, 3D migration experiment - report 3: Performed experiments, results and evaluation, *Stripa Project Technical Report 87-21*, Swedish Nuclear Fuel and Waste Management Company (SKB), Stockholm, Nov., 1987.

Adamson, A.W., *Physical Chemistry of Surfaces*, 4th edition, John Wiley & Sons, Inc., New York, 1990.

Adler, P.M. and H. Brenner, Multiphase flow in porous media, *Ann. Rev. Fluid Mech., 20*, 35-59, 1988.

Babel, M.S., R. Loof, and A. Das Gupta, Fingered preferential flow in unsaturated homogeneous coarse sands, *Hydrological Sciences Journal-Journal Des Sciences Hydrologiques, 40(1)*, 1-17, 1995.

Bear, J., *Dynamics of Fluids in Porous Media*, 764 pp., Elsevier, New York, 1972.

Benjamin, J.R. and C.A. Cornell, *Probability, Statistics, and Decision for Civil Engineers*, McGraw Hill Inc., New York, 684 pp., 1970.

Bikerman, J.J., Sliding of drops from surfaces of different roughnesses, *J. of Colloid Sci., 5*, 349-359, 1950.

Birkholzer, J. and C.-F. Tsang, Solute channeling in unsaturated heterogeneous porous media, *Water Resour. Res., 33(10)*, 2221-2238, 1997.

Bradford, S.A. and F. J. Leij, Wettability effects on scaling two- and three-fluid capillary pressure-saturation relations, *Env. Science and Technology, 29(6)*, 1446-1455, 1995.

Brooks, R.H. and A.T. Corey, Properties of porous media effecting fluid flow, *J. Irrig. Drainage Div. Am. Soc. Civ. Eng., 92*(IR2), 61-88, 1966.

Brown, S., A. Caprihan, and R. Hardy, Experimental observation of fluid flow channels in a single fracture, *J. of Geophy. Res., 103*, 5125-5132, 1998.

Chestnut, D.A., Characterizing the altered zone at Yucca Mountain: The beginning of a testing strategy, *Proceedings of the Third High-Level Radioactive Waste Management International Conference*, Las Vegas, NV., American Nuclear Society, La Grange Park, IL, Vol. 1, pp. 1026-1039, April 12-16.

Chuoke, R.L., P. Van Meurs, and C. Van der Poel, The instability of slow, immiscible, viscous liquid-liquid displacements in permeable media, *Petrol. Trans. AIME, 216*, 188-194, 1959.

Cook, N.G.W., Natural joints in rock - mechanical, hydraulic and seismic behaviour and properties under normal stress, *Int. J. of Rock Mechanics and Mining Sciences & Geomechanics Abstracts, 29(3),* 198-223, 1992.

Corey, A.T., The interrelationship between gas and oil relative permeabilities, *Prod. Mon., 19*, 38-41, 1954.

Crocker, M.E. and L.M. Marchin, Wettability and adsorption characteristics of crude-oil asphaltenes and polar fractions, *J. Petr. Technol., 40(4),* 470-474, 1988.

Dawson, H.E. and P.V. Roberts, Influence of viscous, gravitational, and capillary forces on DNAPL Saturation, *Ground Water, 35(2),* 261-269, 1997.

de Marsily, *Quantitative hydrology: Groundwater Hydrology for Engineers*, Academic Press, New York, 440 pp., 1986.

DiCarlo, D.A., T.W.J. Bauters, C.J.G. Darnault, T.S. Steenhuis, and J.-Y. Parlange, Lateral expansion of preferential flow paths in sands, *Water Resour. Res., 35(2),* 427-434, 1999

Dullien, F.A.L., *Porous Media: Fluid Transport and Pore Structure*, Academic Press, New York, 574 pp., 1992.

Ewing, R.P. and B. Berkowitz, A generalized growth model for simulating initial migration of dense non-aqueous phase fluids, *Water Resour. Res., 34(4),* 611-622, 1998.

Extrand, C.W. and Y. Kumagai, Liquid drops on an inclined plane: The relation between contact angles, drop shape, and retentive force, *J. of Colloid and Interface Science, 170*, 515-521, 1995.

Fabryka-Martin, J.T., A.V. Wolfsberg, A.V. Dixon, P.R. Dixon, S. Levy, J. Musgrave, H.J. Turin, Summary report of chlorine-36 studies: sampling, analysis and simulation of chlorine-36 in the Exploratory Studies Facility, Las Alamos National Laboratory Report LA-CST-TIP-96-002, Los Alamos National Laboratory, Los Alamos, NM, Auguest 1996.

Fourar M., S. Bories, R. Lenormand, and P. Persoff, Two-phase flow in smooth and rough fractures: Measurements and correlation by porous-medium and pipe flow models, *Water Resour. Res., 29(11),* 3699-3708, 1993.

Furmidge, Studies at phase interfaces 1. The sliding of liquid drops on solid surfaces and a theory for spray retention, *J. of Colloid Sci., 17*, 309-324, 1962.

Gauglitz., P.A., C.M. St. Laurent, and C.J. Radke, Experimental determination of gas-bubble breakup in a constricted cylindrical capillary, *Ind. Eng. Chem. Res., 27,* 1282-1291, 1988.

Geller, J.T., G. Su and K. Pruess, Preliminary studies of water seepage through rough-walled fractures, Lawrence Berkeley Laboratory Report LBL Report-38810, Berkeley, C, July, 1996.

Geller, J.T., G. Su, H-Y. Holman, M. Conrad, K. Pruess and J.C. Hunter-Cevera, Processes controlling the migration and biodegradation of non-aqueous phase liquids (NAPLs) within fractured rocks in the vadose zone. FY96 Annual Report, Lawrence Berkeley National Laboratory Report LBNL Report-39996, Berkeley, CA, February, 1997.

Geller, J.T., H.Y. Holman, G. Su, K. Pruess, and J.C. Hunter-Cevera, Flow dynamics and potential for biodegradation of organic contaminants in fractured rock vadose zone, *J. of Cont. Hydrology*, in press.

Geller, J.T., S. Borglin, B. Faybishenko, Experimental study and evaluation of dripping water in fracture models, abstract presented at the Chapman Conference on Fractal Scaling, Nonlinear Dynamics and Chaos in Hydrologic Systems.

Gentier, S., Morphologie et comportement hydromécanique d'une fracture naturelle dans un granite sous contrainte normale, PhD thesis, Univ. of d'Orléans, Orléans, France, 1986.

Glass, R.J., J.-Y. Parlange and T.S. Steenhuis, Wetting front instability, 1, Theoretical discussion and dimensional analysis, *Water Resour. Res., 27(6),* 1187-1194, 1989a.

Glass, R.J., J.Y. Parlange and T.S. Steenhuis, Wetting front instability, 2, Experimental determination of relationships between system parameters and two-dimensional unstable flow field behavior in initially dry porous media, *Water Resour. Res., 25(6),* 1195-1207, 1989b.

Glass, R.J., J.Y. Parlange and T.S. Steenhuis, Mechanism for finger persistence in homogeneous, unsaturated, porous media: Theory and verification, *Soil Science, 148(1),* 60-70, 1989c.

Glass, R.J., J.Y. Parlange and T.S. Steenhuis, Immiscible displacement in porous media: Stability analysis of three-dimensional, axisymmetric disturbances with

application to gravity-driven wetting front instability, *Water Resour. Res., 27(8),* 1947-1956, 1991.

Glass, R.J., Modeling gravity-driven fingering using modified percolation theory, *Proceeding of the Fourth Annual International Conference on High Level Radioactive Waste Management, Las Vegas, NV, April 26-30,* 2042-2052, 1993.

Glass, R.J., M.J. Nicholl, and V.C. Tidwell, Challenging models for flow in unsaturated, fractured rock, through exploration of small scale processes, *Geophysical Research Letters, 22(11),* 1457-1460, 1995.

Glass, R.J., and M.J. Nicholl, 1996, Physics of gravity fingering of immiscible fluids within porous media: An overview of current understanding and selected complicating factors, *Geoderma, 70,* 133-163, 1996.

Iwata, S., T. Tabuchi, and B.P. Warkentin, *Soil-water Interactions: Mechanisms and Applications,* Marcel Dekker, Inc., New York, 1995

Kneafsey, T. and K. Pruess, Laboratory experiments on heat-driven two-phase flows in natural and artificial rock fractures, *Water Resour. Res., 34(12),* 1998.

Kueper, B.H. and E.O. Frind, An Overview of Immiscible Fingering in Porous Media, *J. of Contaminant Hydrology, 2,* 95-110, 1988.

Jury, W.A., Simulation of solute transport using a transfer function model, *Water Resour. Res., 18(2),* 363-368, 1982.

Jury, W.A. and K. Roth, *Transfer Functions and Solute Movement Through Soil: Theory and Application,* 239 pp., Birkhäuser, Basel, Switzerland, 1990.

Keller, A.A., M.J. Blunt, and P.V. Roberts, Micromodel observation of the role of oil layers in three-phase flow, *Transport in Porous Media, 26(3),* 277-297, 1997.

Kung, K-J.S., Preferential flow in a sandy vadose zone: 1. Field observation, *Geoderma, 46,* 51-58, 1990.

Kung, K-J.S., Preferential flow in a sandy vadose zone: 2. Mechanisms and implications, *Geoderma, 46,* 59-71, 1990.

Laroussi, C. and L.W. DeBacker, Relations between geometrical properties of glass beads media and their main ψ θ hysteresis loops, *Soil Sci. Am. J., 43,* 646-650, 1979.

Lenormand, R., C. Zarcone and A. Sarr, Mechanisms of displacement of one fluid by another in a network of capillary ducts, *J. Fluid Mech., 135*, 337-353, 1983.

Levenspiel, O., Nonideal flow, *Chemical Reaction Engineering, 2nd Edition,* pp. 254-325, John Wiley and Sons, New York, 1972.

Liou, T.-S., Statistical analysis of liquid seepage in partially saturated, heterogeneous fracture systems, Ph.D. thesis, University of California, Berkeley, anticipated December 1999.

Liu, B., J. Fabryka-Martin, A. Wolfsberg, B. Robinson and P. Sharma, Significance in apparent discrepancies in water ages derived from atmospheric radionuclides at Yucca Mountain, Nevada, Los Alamos National Laboratory Report LA-UR-95-572, Los Alamos, NM, February 1995.

Long, J.C.S., O. Olsson, S. Martel and J. Black, Effects of excavation on water inflow to a drift, in *Proceedings of the Conference on Fractured and Jointed Rock Masses, Lake Taho, CA,* edited by L.R. Myer et al., pp. 543-549, A.A. Balkema, Brookfield, Vt., 1995.

Luxmoore, R.J., P.M. Jardine, G.V. Wilson, J.R. Jones, and L.W. Zelazny, Physical and chemical controls of preferred path flow through a forested hillslope, *Geoderma, 46*, 139-154.

Mannhardt, K. and H.A. Nasr-El-Din, A review of one-dimensional convection-dispersion models and their applications to miscible displacement in porous media, *In Situ, 18(3),* 277-345, 1994

McCoy, E.L., C.W. Boast, R.C. Stehouwer, and E.J. Kladivko, Macropore Hydraulics: Taking a Sledgehammer to Classical Theory, in *Soil Processes and Water Quality*, edited by R. Lal and B.A. Stewart, pp. 303-348, CRC Press, Inc., Boca Raton, Fl, 1994.

Moreno, L, B. Gylling, and I. Neretnieks, Solute transport in fractured media – The important mechanisms for performance assessment, *Journal of Contaminant Hydrology, 25(3-4)*, 283-298, 1997.

Morrow, N.R. and B. Songkran, Effects of viscous and buoyancy forces on nonwetting phase trapping in porous media, *Surface Phenomena in Enhanced Oil Recovery*, edited by D.O. Shah, Plenum Press, New York, 387-411, 1981.

Nativ, R., E. Adar, O.Dahan and M.Geyh, Water recharge and solute transport through the vadose zone of fractured chalk under desert conditions, *Water Resour. Res., 31(2),* 253-261, 1995.

Neretnieks, I., T. Eriksen, and P. Tahtinen, Tracer movement in a single fissure in granitic rock: Some experimental results and their interpretation, *Water Resour. Res., 18(4),* 849-825, 1982.

Neretnieks, I., Transport in fractured rocks, *Proceedings, Memoirs of the 17th International Congress of International Association of Hydrologists*, vol. XVII, pp. 301-318, International Association of Hydrologists, Tuscon, Ariz., 1985.

Nicholl, M.J., R.J. Glass, and H.A. Hguyem, Small-scale behavior of single gravity-driven fingers in an initially dry fracture, *Proceedings of the Fourth International High-Level Radioactive Waste Management Conference, Las Vegas, NV, April 26-30*, 2061-2070, 1993.

Nicholl, M.J. and R.J. Glass, Wetting phase permeability in a partially saturated horizontal fracture, *Proceedings of the Fifth International High-Level Radioactive Waste Management Conference, Las Vegas, NV, May 22-26*, 2007-2019, 1994.

Nicholl, M.J., R.J. Glass and S.W. Wheatcraft, Gravity-driven infiltration instability in initially dry nonhorizontal fractures, *Water Resour. Res., 30(9),* 2533-2546, 1994.

Nitao, J. and T. Buscheck, Infiltration of a liquid front in an unsaturated, fractured porous medium, *Water Resour. Res., 27(8),* 2099-2112, 1991.

Persoff, P., and K. Pruess, Flow visualization and relative permeability measurements in rough-walled fractures, *Proceedings of the Fourth International High-Level Radioactive Waste Management Conference, Las Vegas, NV, April 26-30*, 2033-2041, 1993.

Persoff, P. and K. Pruess, Two-phase flow visualization and relative permeability measurement in natural rough-walled rock fractures, *Water Resour. Res., 31(5),* 1175-1186, 1995.

Peters, R.R. and E.A. Klavetter, A continuum model for water movement in an unsaturated fractured rock mass, *Water Resour. Res., 24(3),* 416-430, 1988.

Philip, J.R., Stability analysis of infiltration, *Soil Sci. Soc. Am. Proc., 39*, 1042-1049, 1975.

Powers, S.E., W.H. Anckner, and T.F. Seacord, Wettability of NAPL-contaminated sands, *J. of Environmental Engineering, 122(10),* 889-896, 1996.

Prazák, J., M. Sír, F. Kubík, J. Tywoniak and C. Zarcone, Oscillation phenomena in gravity-driven drainage in coarse porous media, *Water Resourc. Res., 28(7),* 1849-1855, 1992.

Pruess, K., and Y. Tsang, On two-phase relative permeability and capillary pressure of rough-walled rock fractures, *Water Resourc. Res., 26(9),* 1915-1926, 1990.

Pruess, K., On water seepage and fast preferential flow in heterogeneous, unsaturated rock fractures, *J. of Contaminant Hydrology, 30,* 333-362, 1998.

Pruess, K., A mechnistic model for water seepage through thick unsaturated zones in fractured rocks of low matrix permeability, *Water Resour. Res., 35(4),* 1039-1051, 1999.

Pruess, K., B. Faybishenko, G.S. Bodvarsson, Alternative concepts and approaches for modeling flow and transport in thick unsaturated zones of fractured rocks, *J. of Cont. Hydrology, 38,* 281-322, 1999

Pyrak-Nolte, L.J. and N.G.W. Cook, Fluid percolation through single fractures, *Geophysical Res. Letters, 15(11),* 1247-1250, 1988.

Raats, P.A.C., Unstable wetting fronts in uniform and nonuniform soils, *Soil Sci. Soc. Am. Proc., 37,* 681-685, 1973.

Rietsma, S. and B.H. Kueper, Laboratory measurement of capillary pressure-saturation relationships in a rock fracture, *Water Resour. Res., 30(4),* 865-878, 1994.

Richards, L.A., Capillary conduction of liquids through porous medium, *Physics, 1,* 318-333, 1931.

Scanlon, B.R., Moisture and solute flux along preferred pathways characterized by fissured sediments in desert soils, *J. of Cont. Hydrology, 10,* 19-46, 1992.

Schwille, F., Spreading as a Fluid Phase in a Fractured Medium, *Dense Chlorinated Solvents in Porous and Fractured Media,* translated by J.F. Pankow, pp.61-72, Lewis Publishers, Chelsea, MI, 1988.

Scheidegger, A.E., *The Physics of Flow Through Porous Media,* 3rd ed., University of Toronto Press, Toronto, Ont., 1974.

Schulkes, R.M.S.M., The evolution and bifurcation of a pendant drop, *J. Fluid Mech., 278,* 83-100, 1994.

Selker, J., Fingered flow in two dimensions, 2, Predicting finger moisture profile, *Water Resourc. Res., 28(9),* 2523-2528, 1992.

Selker, J.S. and M.H. Schroth, Evaluation of hydrodynamic scaling in porous media using finger dimensions, *Water Resour. Res., 34(8),* 1935-1940, 1998.

Shi, X.D., M.P. Brenner, and S.R. Nagel, A cascade of structure in a drop falling from a faucet, *Science, 265,* 219-222, 1994.

Su, G.W., J.T. Geller, K. Pruess, and F. Wen, Experimental studies of water seepage and intermittent flow in unsaturated, rough-walled fractures, *Water Resourc. Res., 35(4),* 1999.

Thunvik, R. and C. Braester, Gas migration in discrete fracture networks, *Water Resourc. Res., 26(10),* 2425-2434, 1990.

Tidwell, V.C., R.J. Glass, and W. Peplinski, Laboratory investigation of matrix imbibition from a flowing fracture, *Geophysical Res. Letters, 22(11),* 1405-1408, 1995.

Tokunaga, T. and J. Wan, Water film flow along fracture surfaces of porous rock, *Water Resour. Res., 33(6),* 1287-1295, 1997.

Tsang, Y.W. and Tsang, C.F., Channel model of flow through fractured media, *Water Resour. Res., 23(3),* 467-479, 1987.

van Genuchten, M.T., A closed form equation for predicting the hydraulic conductivity of unsaturated soils, *Soil Sci. Am. J., 44,* 892-898, 1980.

Vernard, J.K. and R.L. Street, *Elementary fluid mechanics, Sixth edition,* John Wiley & Sons, New York, 689 pp., 1982.

Wang, J.S.Y, and T.N. Narasimhan, Hydrologic mechanisms governing fluid flow in a partially saturated, fractured, porous medium, *Water Resour. Res.,* 21(12), 1861-1874, 1985.

Wang, J.S.Y, N.G.W. Cook, H.A. Wollenberg, C.L. Carnahan, I. Javandel, and C.F. Tsang, Geohydrologic data and models of Rainer Mesa and their implications to Yucca Mountain, *Proceedings, Fourth Annual International High Level Radioactive Waste ManagementConference, Las Vegas, NV,* vol. 1, pp. 675-681, American Nuclear Society, La Grange Part, IL, April 1993.

Wang, Z., J. Feyen, and C.J. Ritsema, Susceptibility and predictability of conditions for preferential flow, *Water Resour. Res., 34(9),* 2169-2182, 1998.

Wang, Z., J. Feyen, and D.E. Elrick, Prediction of fingering in porous media, *Water Resour. Res., 34(9),* 2183-2190, 1998.

White, I., P.M. Colombera, and J.R. Philip, Experimental studies of wetting front instability induced by gradual change of pressure gradient and by heterogeneous porous media, *Soil Sci. Soc. Am. J., 41,* 483-489, 1977.

Wildenschild, D., K.H. Jensen, K. Villholth, and T.H. Illangasekare, A laboratory analysis of the effect of macropores on solute transport, *Ground Water, 32(3),* 381-389, 1994.

Wildenschild, D. and K.H. Jensen. Laboratory investigations of effective flow behavior in unsaturated heterogeneous sand, *Water Resour. Res.,35(1),* 17-27, 1999.

Witherspoon, P.A., J.S.Y. Wang, K. Iwai, and J.E. Gale, Validity of cubic law for fluid flow in a deformable rock fracture, *Water Resour. Res., 16(6),* 1016-1024, 1980.

Zhou, D. and F.M. Orr, Jr., The effects of gravity and viscous forces on residual nonwetting-phase saturation, *In Situ, 19(3),* 249-273, 1995.

ERNEST ORLANDO LAWRENCE BERKELEY NATIONAL LABORATORY
ONE CYCLOTRON ROAD | BERKELEY, CALIFORNIA 94720

Prepared for the U.S. Department of Energy under Contract No. DE-AC03-76SF00098